UNIVERSITÀ
DEGLI STUDI
DI PADOVA

Sede Amministrativa: Università degli Studi di Padova
Dipartimento di Scienze Chimiche

SCUOLA DI DOTTORATO IN: SCIENZA ED INGEGNERIA DEI MATERIALI
CICLO: XXVI

Electrochemical Approaches for the Synthesis and Characterization of Innovative Electrode Materials

Direttore della Scuola: Ch.mo Prof. Gaetano Granozzi
Supervisore: Ch.mo Prof. Armando Gennaro

Dottorando: Lorenzo Perini

RINGRAZIAMENTI

Desidero ricordare tutti coloro che mi hanno aiutato nella stesura di questa tesi di dottorato con suggerimenti, critiche ed osservazioni: a loro va la mia gratitudine.

Desidero ringraziare anzitutto il mio supervisore, *Prof. Armando Gennaro,* per avermi dato la possibilità di svolgere questo progetto nel suo gruppo di ricerca; per la guida sapiente, e per la grande disponibilità dimostratami in questi anni passati sotto la sua supervisione.

Desidero ringraziare il *Dr. Christian Durante,* che con i suoi consigli e suggerimenti ha dato un contributo importante in tutti i risultati da me ottenuti. Ringrazio anche il *Dr. Abdirisak Ahmed Isse* per aver speso il proprio tempo a leggere e discutere con me le bozze del lavoro.

Un sentito ringraziamento va al *Prof. Gaetano Granozzi,* e a tutto il gruppo di scienza delle superfici con il quale ho avuto modo di collaborare. In particolare vorrei ricordare il *Dr. Marco Favaro*, amico e collega, con cui ho condiviso innumerevoli e proficue discussioni intervallate da altrettante pause caffè.

Particularly, I want to extend a special thank to *Dr. Oliver Schneider*, who hosted me for four months as a visiting researcher at the Technical University of Munich; to *Dr. Celine Rüdiger*, who, despite the busy schedule in her work, she always found time to listen to me, advise me, ease my work project and provide me with valuable lessons for my future career.

Un ringraziamento particolare va anche al *Dr. Marco Fantin*, che oltre a un collega è presto diventato un amico, e a tutti i laureandi del laboratorio che hanno contribuito a creare un'atmosfera ricca di momenti sereni e piacevoli e a cui auguro di realizzare tutti i propri progetti.

Vorrei infine ringraziare le persone a me più care: i miei genitori che con il loro incrollabile sostegno morale ed economico mi hanno permesso di raggiungere questo traguardo; i miei amici per essere stati costantemente presenti e preziosa fonte ove ricaricare le forze;

ed infine *Mariachiara*, a cui questo lavoro è dedicato.

CONTENTS

Riassunto **1**

Abstract **5**

Chapter 1. Fuel Cells **9**

1.1 History 9
1.2 Electrode mechanism 11
1.3 Classification 14
1.4 Electrocatalysts 20

Bibliography

Chapter 2. Carbon-Halogen Bond Cleavage **25**

2.1 Overview 25
2.2 Homogeneous electrocatalysis 27
2.3 Role of DET mechanism 30

Bibliography

Chapter 3. Techniques and Instruments **43**

3.1 Linear Sweep and Cyclic Voltammetry 43
3.2 Rotating Disk Electrode 46
3.3 Electrochemical Impedance Spectroscopy 49
3.4 X-ray Photoemission Spectroscopy 51
3.5 Scanning Tunneling Microscopy 53
3.6 Transmission and Scanning Electron Microscopy 55
3.7 Brunauer-Emmett-Teller Theory 58

Bibliography

Chapter 4. HOPG – Highly Oriented Pyrolitic Graphite **61**

4.1 Carbon based electrodes 61
4.2 Chemical and Electrochemical properties of HOPG 62
4.3 Doping of HOPG by ion implantation 64
4.4 Electrochemical characterization 70
4.5 Deposition of Palladium NPs 77
4.6 Activity toward Oxygen Reduction Reaction 82

Bibliography

Chapter 5. GC – Glassy Carbon **91**

5.1 Chemical and Electrochemical properties 91
5.2 Characterization of pristine GC 92
5.3 Deposition of Palladium NPs on GC 95
5.4 Ion implantation and Electrochemical doping 97
5.4.1 Doping by N_2 and Ar ion implantation 97
5.4.2 Doping by carbamate electrolysis 100
5.5 Deposition of Palladium NPs on doped GC 102
5.6 Electrocatalytic activity 109
5.6.1 Activity of N-GC obtained by ion implantation 109
5.6.2 Activity of N-GC obtained by carbamate electrolysis 111

Bibliography

Chapter 6. MC – Mesoporous Carbon **117**

6.1 Synthesis of MC 118
6.2 Synthesis of N-MC 122
6.3 Physical characterizations 125
6.4 Deposition of metal NPs 131
6.5 Activity toward Oxygen Reduction Reaction 135

Bibliography

Chapter 7. Conclusions **141**

Publications and Conferences **I**

ABBREVIATIONS

AA	Active area
AFC	Alkaline fuel cell
Ar-HOPG	Ar sputtered HOPG
BE	Binding energy
BET	Brunauer, Emmett, Teller
BDD	Boron doped diamond
BDE	Bond dissociation energy
BnCl	Benzyl chloride
CA	Cronoamperometry
CB	Carbon black
CPE	Constant phase element
CV	Cyclic voltammetry
DET	Dissociative electron transfer
DMF	Dimethylformamide
DOS	Density of state
EIS	Electrochemical impedance spectroscopy
ET	Electron transfer
FBDD	Fluorinated boron doped diamond
FC	Fuel cell
FWHM	Full width at half maximum
GC	Glassy carbon
GDL	Gas diffusion layer
HOPG	Highly oriented pyrolitic graphite
HOR	Hydrogen oxidation reaction
LM	Light microscopy
LSV	Linear sweep voltammetry
MEA	Membrane electrode assembly
MC	Mesoporous carbon
MCFC	Molten carbonate fuel cell
MeCN	Acetonitrile
MS	Mesoporous silica
N-GC	Nitrogen doped glassy carbon
N-HOPG	Nitrogen doped HOPG
N-MC	Nitrogen doped mesoporous carbon
PAFC	Phosphoric acid fuel cell
PBS	Phosphate buffered solution
PEM	Proton exchange membrane

PZC	Potential of zero charge
NPs	Nanoparticles
ORR	Oxygen reduction reaction
RDE	Rotating disk electrode
RMS	Root mean square
RX	Organic halide
SCE	Saturated calomel electrode
SCCM	Standard cubic centimeter for minute
SCSE	Small cluster size effect
SEM	Scanning electron microscopy
SOFC	Solid oxide fuel cell
SOS	Spin orbit splitting
STM	Scanning tunnelling microscopy
TEM	Transmission electron microscopy
UHV	Ultra high vacuum
XPS	X-ray photoemission spectroscopy

RIASSUNTO

La sintesi di catalizzatori nanostrutturati è una via imprescindibile per affrontare le sfide energetiche moderne, che vanno dal migliorare l'efficienza delle celle a combustibile alla degradazione di agenti inquinanti [1]. A questo proposito, l'elettrocatalisi è un campo di particolare interesse e uno dei più promettenti grazie all'abilità dei metodi elettrochimici di studiare meccanismi di reazione e trasferimenti elettronici a livello molecolare alla superficie elettrodica. I notevoli progressi nella sintesi di nonostrutture hanno messo in luce nuove tipologie di catalizzatori nanomolecolari e nuove proprietà catalitiche [2]. Spesso, i catalizzatori nanostrutturati sono supportati su elettrodi dove l'effetto catalitico si manifesta come minore sovratensione richiesta e si parla quindi di elettrocatalisi.

Lo sviluppo e l'uso di nuovi materiali elettrodici e di elettrodi modificati nel campo *dell'elettrochimica applicata*, dell'*energetica* e dell'*elettrosintesi organica* è oggi un importante via per ottenere catalizzatori con struttura e morfologia controllata e reazioni selettive. Il controllo su una varietà di fenomeni fisici e chimici che vanno dalla catalisi al trasferimento elettronico è spesso ottenuto attraverso l'ampio uso di superfici modificate. Una superficie elettrodica può essere modificata principalmente attraverso: (i) l'alterazione della sua struttura o (ii) la variazione della sua composizione chimica (o entrambe) [3].

L'avvento della tecnologia nel campo delle celle a combustibile ha creato il bisogno di generare nuovi catalizzatori per sostituire il platino costoso e raro il quale contribuisce per più del 55% del costo complessivo della cella stessa. Ridurre il caricamento di Pt (in modo particolare al catodo) senza compromettere le prestazioni delle Fuel Cells (FCs) è una strategia necessaria per la loro commercializzazione. Inoltre, la progettazione di nuovi catalizzatori richiede non solo di ridurre il contenuto di metallo nobile ma anche di aumentarne l'attività catalitica e la durabilità.

Nelle FCs, la reazione di riduzione dell'ossigeno (ORR) è la reazione che decorre al catodo. È stato osservato che questa reazione, in una tipica PEM fuel cell, è caratterizzata da una lenta cinetica con una sovratensione di ca. 300 mV usando l'attuale stato dell'arte sui catalizzatori di platino rispetto alla reazione di ossidazione d'idrogeno

dell'anodo [4]. Idealmente, il potenziale standard di cella, E^{0}_{cell}, è 1.23 V con energia libera di Gibbs minore di zero, il che implica una reazione spontanea che può essere utilizzata per produrre energia elettrica. In pratica però, il potenziale di cella è minore di 1.23 V a causa della sovratensione di cella principalmente causata al catodo in quanto una notevole quantità di energia è necessaria per rompere il doppio legame ossigeno-ossigeno durante il processo. Ad esempio, materiali carboniosi dopati azoto e i loro compositi possiedono grandi potenzialità per applicazioni come catalizzatori in fuel cells e in particolare per la riduzione di ossigeno al catodo, poiché il meccanismo di reazione di catalizzatori dopati azoto per ORR sembra evolvere con adsorbimento di ossigeno [5] su atomi di carbonio parzialmente polarizzati adiacenti ai droganti azoto, diversamente dal meccanismo dei catalizzatori metallici (es. Pt, Pd) dove l'orbitale σ dell'ossigeno forma un legame con l'orbitale d_z^2 parzialmente occupato del metallo stesso.

Invece, nel campo dell'elettrocatalisi organica, un argomento di grande interesse è lo studio del comportamento di elettrodi catalitici nella riduzione di alogenuri organici [6]. Infatti, la scelta del materiale elettrodico è spesso cruciale per il successo della reazione elettrochimica allo scopo di ottenere reazioni selettive. Per nostra esperienza, materiali elettrodici come Ag, Cu o Pd hanno un enorme effetto catalitico sulla riduzione elettrochimica di alogenuri organici in solventi organici comuni come MeCN, DMF, etc. [7]. Questo permette non solo di ridurre i substrati a potenziali più positivi ma può anche modificare i meccanismi di reazione e la selettività [8]. È quindi di grande interesse trovare nuovi materiali catalitici per creare condizioni più favorevoli per i processi elettrochimici. Pertanto, è di primaria importanza caratterizzare i parametri che influenzano la reattività e la selettività di una superficie catalitica, al fine di utilizzare tali conoscenze per la progettazione sistematica di catalizzatori migliori.

I parametri che possono influenzare le proprietà elettrocatalitiche delle nanoparticelle [9,10] sono: (i) dimensione, (ii) dispersione, (iii) densità di atomi superficiali non coordinati, (iv) influenza del materiale di supporto. Per valutare questi parametri sistemi modello che non presentino difetti chimici e morfologici (HOPG) e nanostrutture depositate su di essi sotto forma di monolayer devono essere studiate.

Generalmente, gli elettrodi modificati sono costituiti da un supporto inerte, come la grafite (HOPG), il glassy carbon (GC) o il carbonio mesoporoso (MC) dove le

nanonparticelle metalliche sono depositate sulla superficie. Questi materiali sono molto interessanti poiché tutti i supporti a base di carbonio possiedono una notevole stabilità chimica, larga finestra di potenziale e bassa corrente di fondo.

Questo progetto di tesi ha come scopo quello di preparare e caratterizzare differenti materiali carboniosi, prima e dopo la modificazione con etero atomi (in particolare Azoto), con lo scopo di studiare le loro proprietà catalitiche verso la reazione di riduzione dell'ossigeno e la riduzione di alogenuri organici. Dopo di che, depositeremo nanoparticelle metalliche preparate per evaporazione in ultra-alto-vuoto (UHV), e per riduzione chimica ed elettrochimica, per confrontare i risultati dai tre metodi di deposizione e ottenere migliori indicazioni circa la possibilità di sviluppare un elettrocatalizzatore reale nelle differenti tematiche viste precedentemente.

La prima parte sarà rivolta a ricercare le migliori condizioni sperimentali per ottenere nuovi materiali elettrodici mediante tecniche in ultra-alto-vuoto per ottenere N-HOPG e N-GC o attraverso la sintesi chimica per ottenere N-MC. Dopo la valutazione delle proprietà chimiche e morfologiche, nella seconda parte saranno investigate le reazioni di riduzione dell'ossigeno e di riduzione degli alogenuri organici le quali possono dipendere dal solvente, pH, elettrolita di supporto, potenziale di lavoro e meccanismo di trasferimento elettronico.

La caratterizzazione chimica e fisica sarà condotta usando Cyclic Voltammetry (CV), Rotating Disk Electrode (RDE), X-ray Photoelectron Spectroscopy (XPS), Transmission and Scanning Electron Microscopy (TEM, SEM) and Brunauer-Emmett-Teller theory (BET).

Bibliografia

[1] Jacobson, M.Z.; Colella, W.G.; Golden D.M. *Science* **2005**, *308*, 1901.

[2] Steele, B.C.H.; Heinzel, A. *Nature* **2001**, *414*, 331.

[3] Bell, A.T. *Science* **2003**, *299*, 1688.

[4] Poizot, P.; Simonet, J. *Electrochim. Acta* **2010**, *56*, 15.

[5] Maldonado, S.; Stevenson, K.J. *J. Phys. Chem*. B **2010**, *109*, 4707.

[6] Isse, A.A.; Sandonà, G.; Durante, C.; Gennaro, A. *Electrochim. Acta* **2009**, *54*, 3235.

[7] Isse, A.A.; Gennaro, A. *Collect. Czech. Chem. Comm.* **2003**, *68*, 1379.

[8] Isse, A.A.; Gottardello, S.; Durante, C.; Gennaro, A. *Phys. Chem. Chem. Phys.* **2008**, *10*, 2409.

[9] Kitchin, J.R.; Nørskov, J.K.; Barteau, M.A.; Chen, J.G. *Phys. Rev. Lett.* **2004**, *93*, 156801.

[10] Wolfschmidt, H.; Weingarth, D.; Stimming, U. *Chem. Phys. Chem.* **2010**, *11*, 1533.

ABSTRACT

The synthesis of nanoscale catalysts is a cornerstone technology to meet the current energy challenges, spanning in a wide range of applications from fuel cell efficiency to pollutant degradation [1]. On this regard, electrocatalysis is a field of particular interest and one of the most promising, owing to the ability of electrochemical methods to study the reaction mechanisms and electron transfer (ET) dynamics at a molecular level, at the electrode surface. With the rapid advances in nanostructure synthesis, new nanoscale catalysts and novel catalytic properties continue to emerge [2]. Often, nanoscale catalysts are used on electrodes, where the electrode modifies the kinetics of the process reducing the overpotential, hence performing electrocatalysis.

The development and use of new electrodic materials and modified electrodes in the field of *applied electrochemistry*, *energy* and *organic electrosynthesis* is today an important way to obtain catalysts with controlled structure and morphology, and reactions with high selectivity. Control over a variety of physical and chemical phenomena ranging from catalysis to electron transfer is often achieved through the extensive use of modified surfaces. There are basically two possibilities for the modification of an electrode surface, (i) to alter its structure or (ii) to modifiy its composition (or both) [3].

The emergence of fuel cell technology has created a new tool for the generation of new catalysts to replace the expensive and rare platinum, which contributes to over 55% of the total costs. Reducing the Pt loading (particularly in the cathode catalyst layer) without compromising the fuel cell performance is an effective strategy to meet the cost requirements for its commercialization. In addition, the design of novel electrocatalysts requires not only reducing the amount of Pt used, but also enhancing catalytic activity and durability.

In fuel cells (FCs), the oxygen reduction reaction (ORR) is the reaction occurring at the cathode. ORR in a typical PEM fuel cell is a slow reaction; using the state-of art platinum catalysts the overpotential of ORR is found to be 300 mV higher than that of the oxidation reaction at the anode [4]. Ideally, the standard cell potential, $E^{\mathbf{0}}_{\text{cell}}$, is 1.23 V with a negative Gibbs free energy, implying a spontaneous reaction that

can be utilised as an electrical energy generator. Practically, however, the cell potential is less than 1.23 V due to an overpotential in the cell, primarily related to the oxygen reduction reaction at the cathode, which is kinetically sluggish because a large amount of energy is needed to break the strong oxygen-oxygen double bond during the process. For example, Nitrogen-doped carbon and its composites possess a great potential for fuel cell catalyst applications, especially at the oxygen reduction reaction. The ORR mechanisms of nitrogen-doped carbon catalysts seem to involve adsorption of oxygen [5] at the partially polarised carbon atoms adjacent to the nitrogen dopants, in contrast to the mechanism at metal catalysts (i.e. Pt, Pd), which utilise d-bands to form bonds with oxygen.

Indeed, in the field of organic electrocatalysis, a topic of great interest is the behaviour of catalytic electrode materials for the reduction of organic halides [6]. In fact, the choice of electrode materials is often crucial for the success of electrochemical reactions in order to achieve selective reactions. In our own experience, some electrode materials such as Ag, Cu or Pd in organic solvents (MeCN, DMF, etc.) showed extraordinary catalytic properties for the electroreduction of organic halides [7]. This allows not only the reduction of the substrates at more positive potentials, but also makes possible modification of the reaction mechanism and selectivity [8]. It is thus of great interest to find new catalytic materials to create more favourable conditions for electrochemical processes. Therefore, it is of primary importance to characterize decisive parameters influencing the reactivity and the selectivity of a catalytic surface, in order to use this knowledge for the systematic design of better catalysts.

The parameters influencing the electrocatalytic properties of nanoparticles [9,10] can be: (i) particle size, (ii) particle dispersion, (iii) density of low-coordinated surface atoms and (iv) effect of the substrate material. In order to evaluate these parameters, model surfaces without chemical and morphological defects (HOPG) and monolayer nanostructures deposited on them must be investigated.

Usually, the modified electrodes are built from an inert support, such as graphite (HOPG), glassy carbon (GC) or mesoporous carbon (MC), on which metal nanoparticles are deposited. These supports are very interesting because, like all carbon-based supports, they have chemical stability, wide potential window and low background current.

This PhD thesis project intends to prepare and characterize different carbon materials, before and after doping with heteroatoms (particularly Nitrogen), with aim of investigating their catalytic properties in the ORR and in the reduction of organic halides. After that, we will try to deposit metal nanoparticles prepared by evaporation in ultra-high-vacuum (UHV), or by electrochemical and chemical means, to compare the results achieved using the three deposition methods and gain a better indication about the possibility to device a real electro-catalyst in the different fields described above.

The first task includes the research for the best experimental conditions to obtain the new electrode materials. To this end, UHV conditions will be investigated to synthetize N-HOPG and N-GC, whereas chemical synthesis followed by annealing will be used to prepare N-MC. After evaluation of the chemical and morphological properties of the materials, the second goal is to investigate their catalytic properties toward the electrochemical reduction reactions of oxygen and organic halides, reactions that can be influenced by solvent, pH, supporting electrolyte, working potential and electron transfer mechanism.

The physical and chemical characterizations will be carried out using Cyclic Voltammetry (CV), Rotating Disk Electrode (RDE), X-ray Photoelectron Spectroscopy (XPS), Transmission and Scanning Electron Microscopy (TEM, SEM) and Brunauer-Emmett-Teller theory (BET).

Bibliography

[1] Jacobson, M.Z.; Colella, W.G.; Golden D.M. *Science* **2005**, *308*, 1901.

[2] Steele, B.C.H.; Heinzel, A. *Nature* **2001**, *414*, 331.

[3] Bell, A.T. *Science* **2003**, *299*, 1688.

[4] Poizot, P.; Simonet, J. *Electrochim. Acta* **2010**, *56*, 15.

[5] Maldonado, S.; Stevenson, K.J. *J. Phys. Chem*. B **2010**, *109*, 4707.

[6] Isse, A.A.; Sandonà, G.; Durante, C.; Gennaro, A. *Electrochim. Acta* **2009**, *54*, 3235.

[7] Isse, A.A.; Gennaro, A. *Collect. Czech. Chem. Comm.* **2003**, *68*, 1379.

[8] Isse, A.A.; Gottardello, S.; Durante, C.; Gennaro, A. *Phys. Chem. Chem. Phys.* **2008**, *10*, 2409.

[9] Kitchin, J.R.; Nørskov, J.K.; Barteau, M.A.; Chen, J.G. *Phys. Rev. Lett.* **2004**, *93*, 156801.

[10] Wolfschmidt, H.; Weingarth, D.; Stimming, U. *Chem. Phys. Chem.* **2010**, *11*, 1533.

FUEL CELLS

1.1 History

A Fuel Cell (FC) is an electrochemical cell that can continuously convert the chemical energy evolving from a fuel into electricity through a chemical reaction with oxygen or another oxidizing agent [1]. Hydrogen is the most common fuel, but also hydrocarbons, such as natural gas and alcohols like methanol, are sometimes used. FCs are different from batteries in requiring a constant source of fuel and oxygen to run, but they can produce electricity continuously for as long as these elements are supplied.

The principle of the FC was discovered by the German scientist Christian Friedrich Schönbein in 1838 and published in one of the scientific magazines of that time. Based on this work, the first FC operational validity was proved by Sir William Robert Grove in the February 1839 edition of the *Philosophical Magazine and Journal of Science,* and later sketched, in 1842, in the same journal. In 1939, the British engineer Francis Thomas Bacon successfully developed a stationary alkaline fuel cell. Later in 1959, Bacon and his colleagues demonstrated a practical five-kilowatt unit capable of powering a welding machine. In 1955, W. Thomas Grubb, a chemist working for the General Electric Company (GE), further modified the original fuel cell design using a sulphonated polystyrene ion-exchange membrane as the electrolyte.

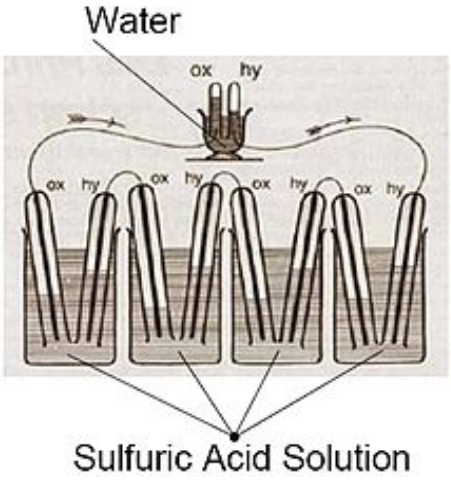

Fig. 1.1 - William Grove's FC (1839).

Three years later, another GE chemist, Leonard Niedrach, devised a way of depositing platinum onto the membrane, which served as a catalyst for the hydrogen oxidation and oxygen reduction reactions necessary for its function. This became known as the "Grubb-Niedrach fuel cell" that was used during Project Gemini, the first

commercial use of a fuel cell. In 1991, the first hydrogen fuel cell automobile was developed by Roger Billings. UTC Power (United Technologies Company) was the first company to manufacture and commercialize a large, stationary fuel cell system as a co-generation power plant in hospitals, universities and large office buildings. UTC Power continues to be the sole supplier of fuel cells to NASA for use in space vehicles, having supplied fuel cells for the Apollo missions and the Space Shuttle program.

During the last decade, FCs have received enormous attention from research institutions and companies as a novel electrical energy production systems. In the near future, they foresee applications in automotive propulsion, distributed power generation, and in low power portable devices (as battery replacements).

The reasons for the late evolution of FCs can be attributed mainly to economic factors, lack of suitable innovative materials, and certain inadequacies in the operation of electrochemical devices. At the beginning of the 20th century, with an increase in the use of electricity, the conversion of chemical energy into electrical energy became more and more important even though primary energy sources were still abundant, unrestricted, and inexpensive at that time.

The development of FCs in the last few years is due to the environmental consequences of the daily use of fossil fuel for the production of electricity and propulsion of vehicles [2]. There are several ways in which harmful emissions in the atmosphere by human activities can be controlled and our dependence on fossil fuels reduced without diminishing the standard of living. The combustion of fossil fuels releases harmful emissions into the air, which are related with global warming and influence the health of people, especially in urban areas. At the same time, fear is often expressed that the rapid consumption and the resulting disappearance of fossil fuels will eventually stop the future progress of technology at a time when the increasing world population needs far more food, better use of resources, improved industrial products and extended means of transport and communication.

FC systems are important components of a rapidly emerging “Energy Technology”, which has many industrial supporters as well as an established competitive technology to match in costs and performances. The chances to become an essential part of the environmentally-benign energy supply technology of the next century are good, particularly for the dispersed and local fuel cell power plants which

can produce electricity and heat. The operation life, the efficiency and costs of FC systems will be the key for the next study and development.

1.2 Electrode mechanism

An electrochemical cell consists of two electrodes (an anode and a cathode) and has the overall reaction described below.

$$Ox_1 + Red_2 \longrightarrow Red_1 + Ox_2 \qquad [1.1]$$

The voltage of the cell, ΔE, is represented by the difference between the potentials of the two half-cells, whereby the equilibrium potential of each half-cell reaction is given by the Nernst Equation (Eq. 1.2), in which n is the number of electrons involved and F is the Faraday constant.

$$E = E^{\theta} + \frac{RT}{nF} ln \frac{a_{ox}}{a_{red}} \qquad [1.2]$$

Fuel cells are Galvanic cells, in which the free energy of a chemical reaction is converted into electrical energy (via an electrical current). The Gibbs free energy change of a chemical reaction is linearly related to the cell voltage (Eq. 1.3).

$$\Delta G = -nF\Delta E \qquad [1.3]$$

The anodic reaction in a fuel cell is either the direct oxidation of hydrogen or the oxidation of methanol. An indirect oxidation, via a reforming step, can also occur. The cathodic reaction is usually the reduction of oxygen and in most cases the oxygen source is air. This reaction has been investigated in numerous studies but the complete mechanism of oxygen reduction is still not thoroughly understood [2]. Two different possible mechanisms are given below.

In acid electrolytes:

Cathode: $O_2 + 4\ H^+ + 4\ e^- \longrightarrow 2\ H_2O$ $\quad E^0 = 1.229$ V

Anode: $H_2 \longrightarrow 2\ H^+ + 2e^-$ $\quad E^0 = 0.000$ V

Total: $2\ H_2 + O_2 \longrightarrow 2\ H_2O$ $\quad \Delta E^0 = 1.229$ V

In alkaline electrolytes:

Cathode: $O_2 + 2\ H_2O + 4\ e^- \longrightarrow 4\ OH^-$ $\quad E^0 = 0.401$ V

Anode: $H_2 + 2\ OH^- \longrightarrow 2\ H_2O + 2e^-$ $\quad E^0 = -0.828$ V

Total: $2\ H_2 + O_2 \longrightarrow 2\ H_2O$ $\quad \Delta E^0 = 1.229$ V

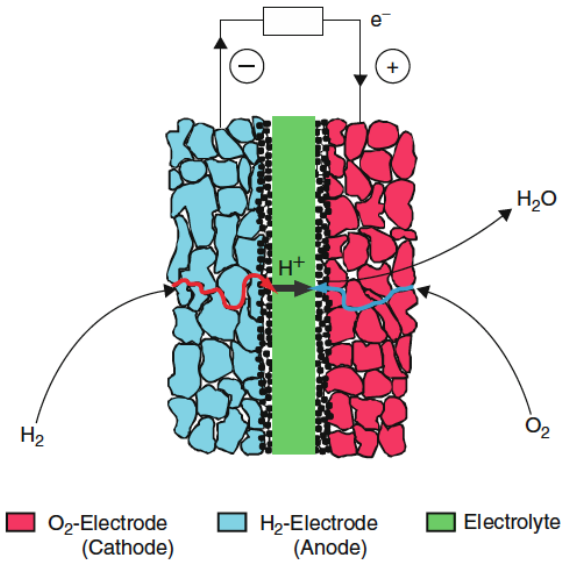

Fig. 1.2 - Simplified fuel cell scheme with an acidic aqueous electrolyte.

An oxygen reduction reaction (ORR) is a multi-electron reaction that includes several elementary reactions. Yeager proposed two mechanisms for ORR in acidic

media [3]:

1) a "direct" four-electron mechanism where O_2 is directly reduced to water, without generation of hydrogen peroxide (H_2O_2): $O_2 + 4H^+ + 4e^- \rightarrow 2H_2O$ and
2) a "series" mechanism in which O_2 is firstly reduced to H_2O_2: $O_2 + 2H^+ + 2e^- \rightarrow H_2O_2$, followed by a further reduction of H_2O_2 to H_2O: $H_2O_2 + 2H^+ + 2e^- \rightarrow H_2O$.

Adzic et al., on the other hand, proposed a parallel pathway in which the direct and series mechanisms occur simultaneously, with the direct pathway (1) as the dominant one [4]. For transition metal catalysts, two-electron reduction was reported for less active metals such as Au and Hg. The most active of these catalysts are Pt and Pt-based alloys; in the mechanism of action of these very active catalysts a four-electron reduction is generally observed. However, the detailed mechanism and reduction pathways are not completely clear and much debate on the subject is still going on. Even for the first electron transfer step, different views exist [5–7]. Examples of plausible first steps include the following: (1) the breakage of the O–O bond upon oxygen adsorption on two Pt sites (S) in a bridge configuration, $O_2 + 2S \rightarrow O^* + O^*$; (2) formation of the superoxide anion, $O_2 + 2S + e^- \rightarrow O_2^-$; and (3) simultaneous electron and proton transfer, $O_2 + 2S + (H^+ + e^-) \rightarrow OOH$. O_2 reduction pathways are affected to a great extent by the O_2 adsorption modes on catalyst surfaces. There are three adsorption models for molecular oxygen adsorption, shown in Fig. 1.3:

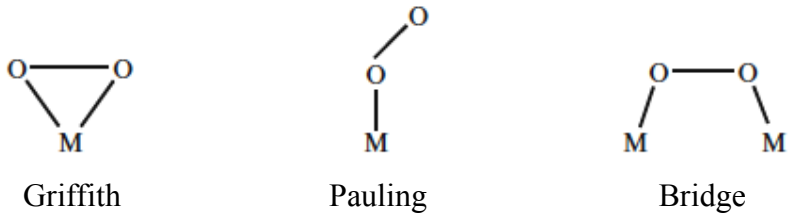

Fig. 1.3 - Models of O_2 adsorption on electrode surfaces.

1. In Griffith model, O_2 interacts with a single substrate atom [8] forming a bond between its σ-orbitals and the empty d_z^2 orbitals of the metal surface atom and by forming a σ-backbond from the partially filled d_{xy} or d_{yz} metal orbitals to the antibonding π* orbitals of O_2.

2. Pauling model involves the end-on adsorption through a single σ-type bond, in which the σ-orbital of O_2 donates electrons to the d_z^2 orbital on the metal.
3. The bridge model, with an O_2 molecule bonding with two metal sites, was firstly proposed by Yeager [9], principally for the reaction on platinum group metals.

In brief, the direct four-electron pathway is preferable because it does not involve the formation of peroxide species in solution and the charge efficiency of the reaction is greater. However, this mechanism consists in a number of steps in which molecular oxygen dissociates at the surface and combines with hydrogen ions. Therefore, the adsorption of an oxygen species on the surface of the metal particles is essential for the electron transfer.

1.3 Classification

There are many types of fuel cells, but they all consist of an anode (negative side), a cathode (positive side) and an electrolyte that allows ions to move between the two sides of the fuel cell. Electrons are drawn from the anode to the cathode through an external circuit, producing current electricity (Fig. 1.2). On the contrary, a fuel and an oxidant are stored outside the cell providing the chemical energy, and as long as the cell is supplied with them, electrical power can be *directly* obtained (Fig. 1.4 [1]).

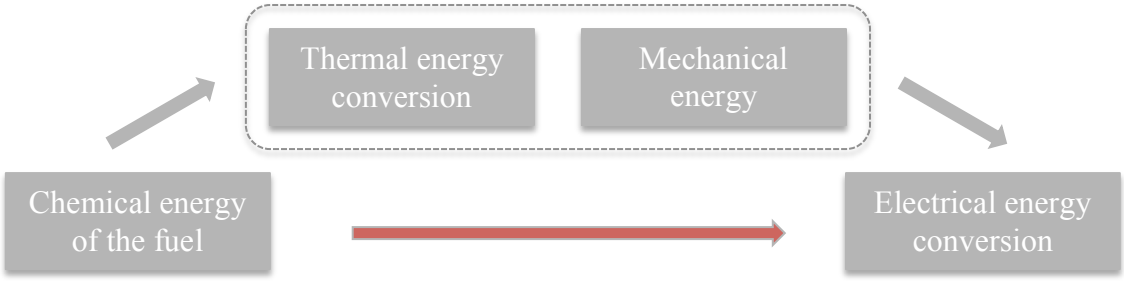

Fig. 1.4 - Direct energy conversion (FCs) in comparison to Conventional Indirect Technology.

There are several types of FCs and many classifications exist in the literature [10]. FC systems can be classified according to different parameters; one of them, for example, could be the working temperature (high, medium and low temperature) or the operational pressure (high, medium and low pressure). Another one might be the type of fuel that the fuel cell uses: whether gas, liquid or solid. For practical reasons, FC systems are simply classified by the type of electrolyte used and the names and abbreviations reported in Table 1.1 are now frequently used.

FC Type	Operating Temp. (°C)	System Size	Electrical Efficiency	Applications	Key Advantages
PEMFC	50-100°C	<1KW-100KW	30-60%	Backup power Portable power Transportation Special vehicles	Low temperature, quick startup
AFC	90-100°C	10-100KW	60%	Military Space	Fast cathode reaction, low cost components
PAFC	150-200°C	400KW	>40%	Distributed generation	Tolerance to hydrogen impurities
MCFC	600-700°C	300KW-3MW	45-47%	Electric utility	High efficiency, fuel flexibility
SOFC	700-1000°C	1KW-2KW	35-43%	Electric utility Distributed generation	High efficiency, use of solid electrolyte

Table 1.1 - Fuel Cells classification.

Individual fuel cells produce relatively small electrical potentials, about 0.7 V, so cells are "stacked", or placed in series, to increase the voltage to meet application's requirements. The energy efficiency of a fuel cell is generally between 40 to 60%, but can be increased up to 85% if waste heat is captured for use.

- **PEMFC**

A single PEMFC is made of three components: a membrane-electrode assembly (MEA), two bipolar plates and two seals (Fig. 1.5). The MEA consists of a membrane, two dispersed catalyst layers and two gas diffusion layers (GDL). The membrane separates the reduction and oxidation half-reactions, allowing protons to pass through to complete the overall reaction; GDLs improve the efficiency of the cell, allowing direct and uniform access of the fuel on both half-catalyst layers (Fig. 1.2).

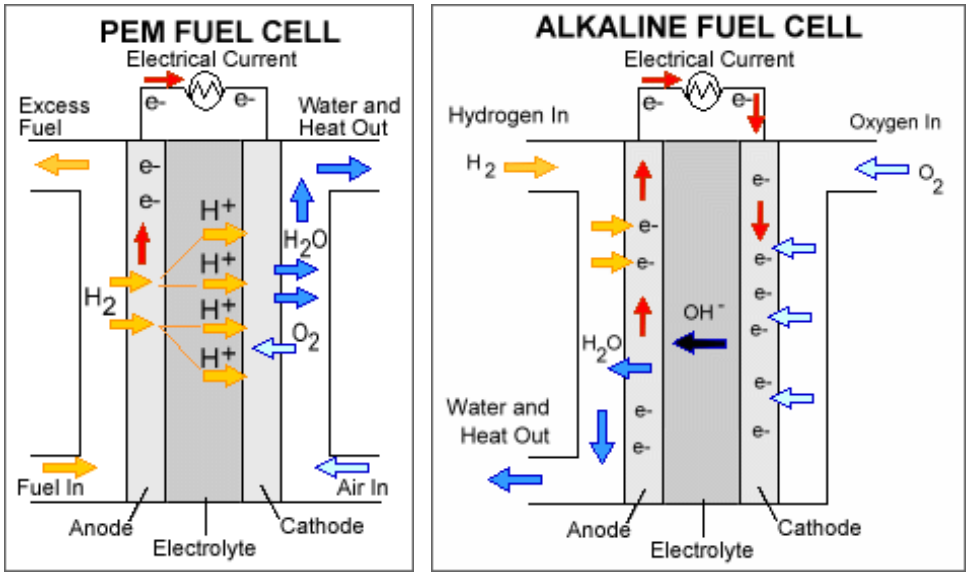

Fig. 1.5 - Scheme of a proton exchange membrane fuel cell and an alkaline fuel cell.

Application of PEMFC as a primary power source in electric vehicles has received a lot of attention in the past decade due to several technical advantages.
The advantages of PEMFC are:

- there is no free corrosive liquid in the cell,
- therefore, corrosion problems are minimal,
- the cell is simple to fabricate,
- they are able to withstand large pressure differentials,
- they have demonstrated long life.

There are also some disadvantages:

- the Nafion electrolyte is expensive and the cell costs are high,
- water management in the membrane is critical for efficient operation,
- CO tolerance is poor because of catalyst poisoning.

PEMFCs use a polymer membrane as electrolyte, which is an electronic insulator but an excellent conductor of hydrogen ions. The most commonly used membrane is Nafion®, which presents a fluorocarbon polymer backbone to which sulfonic acid groups are attached (Fig. 1.6) [11]. The acid molecules are fixed to the polymer and cannot be leached out, but the protons on these acid groups are free to migrate through the electrolyte.

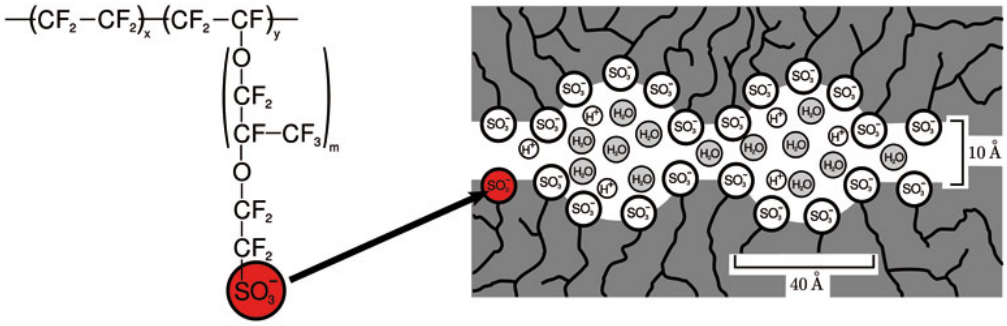

Fig. 1.6 - Chemical structure and water-filled channels of Nafion®.

This polymer is used in the form of very thin membrane, typically 50-180 μm thick, and can be handled easily and safely.

One critical issue of PEMFCs is that water is produced in the membrane, so the FC must work at temperatures below 100 °C, despite the fact that the catalyst has its highest activity at temperatures higher than 100 °C. Another important issue is the low tolerance of the cell to carbon monoxide (CO). In particular, when hydrogen is formed by methane or methanol steam reforming process, an amount of CO of 1% is produced, causing a drop of the cell performance. Current oxidation technologies can reduce CO levels down to <10 ppm, even though this is difficult to maintain under actual operating conditions.

- **AFC**

The AFC is one of the most developed FCs since the mid-1960s in the Apollo mission. As PEMFC, it uses hydrogen and oxygen to produce water, heat and electricity with the highest efficiency of 60%. The two electrodes are separated by a porous matrix saturated with an aqueous alkaline solution, such as potassium hydroxide (Fig. 1.5). Aqueous alkaline solutions do not tollerate carbon dioxide (CO_2) so the fuel cell can be "poisoned" through the conversion of KOH to potassium carbonate (K_2CO_3). Because of this, alkaline fuel cells typically operate with pure oxygen, or at least purified air, and incorporate a 'scrubber' moiety into the design to clean out as much of the CO_2 as possible, increasing cell costs.

- **PAFC**

Phosphoric acid fuel cells use liquid phosphoric acid as an electrolyte (Fig. 1.7). A Teflon-bonded silicon carbide matrix contains the phosphoric acid and a porous carbon electrode contains a platinum catalyst. Other inorganic acids such as $HClO_4$, H_2SO_4, HF and HCl were evaluated in laboratory scale for use in FCs. In comparison to H_3PO_4, these acids have lower thermochemical stability and higher vapour pressure, and therefore are not acceptable replacements for H_3PO_4 at high temperatures (~200°C).

The PAFC is considered as a "first generation" of modern fuel cells. It is one of the most mature cell types and the first to be used commercially. This type of fuel cell is typically used for stationary power generation and its efficiecy is around 35-42%. As PEMFCs, PAFCs require an expensive platinum catalyst, which raises the overall cost of the fuel cell.

- **MCFC**

MCFCs are high-temperature fuel cells that use an electrolyte composed of a molten carbonate salt mixture suspended in a porous, chemically inert lithium aluminium oxide ($LiAlO_2$) ceramic matrix (Fig 1.7). Because they operate at extremely high temperatures (650°C and above), non-precious metals can be used as catalysts at

the anode and cathode to reduce costs. Molten carbonate fuel cells can reach efficiencies approaching 65%, considerably higher than the 35–42% efficiency of phosphoric acid fuel cells. Molten carbonate fuel cells are not sensitive to carbon monoxide or carbon dioxide "poisoning", so they can even use carbon monoxide as a fuel, rendering them more attractive for fuelling with gases derived from coal. The primary disadvantage of current MCFC technology is durability. The high temperatures at which these cells operate and the corrosive electrolyte used accelerate component breakdown and corrosion, decreasing cell life.

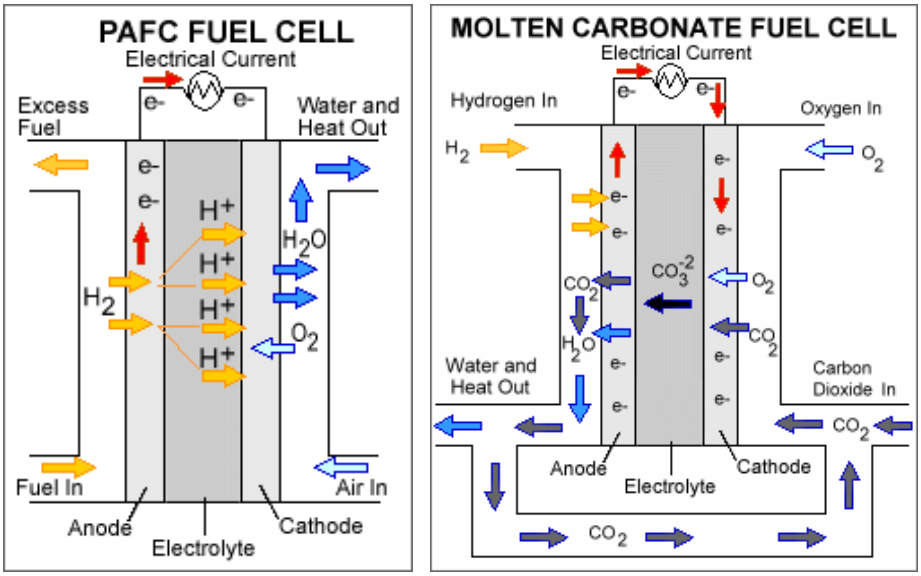

Fig. 1.7 - Scheme of a phosphoric acid fuel cell and molten carbonate fuel cell.

- **SOFC**

Solid oxide fuel cells (SOFCs) use a hard, non-porous ceramic compound as the electrolyte (Fig 1.8). Solid oxide fuel cells operate at very high temperatures (around 1000 °C), so they make expensive catalyst unnecessary, thereby reducing cost. It also allows SOFCs to reform fuels internally, which enables the use of a variety of fuels and reduces the cost associated with adding a reformer to the system. In addition, they are

not affected by poisoning by carbon monoxide (CO), which can even be used as a fuel. This property allows SOFCs to use gases made from coal.

High-temperature operation has disadvantages. It results in a slow start-up and requires significant thermal shielding to retain heat and protect personnel, which may be acceptable for utility applications but not for transportation and small portable applications. The high operating temperatures also place stringent durability requirements on materials.

Scientists are currently developing new low-cost materials with high durability at these operating temperatures, and exploring the potential for developing lower-temperature SOFCs operating at or below 800 °C, that have fewer durability problems and lower cost.

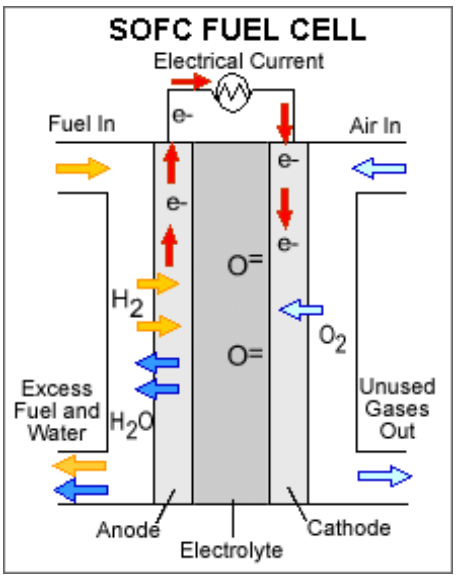

Fig. 1.8 - Scheme of a solid oxide fuel cell.

1.4 Electrocatalysts

Our interest is mainly focused on low temperature FCs, where molecular hydrogen is oxidized to form protons and electrons at the anode, while oxygen is reduced at the cathode leading to the formation of water. Both these reactions require

electrocatalysts to reduce the overpotential and to increase reaction rates. In the state of the art, Pt-based materials are used as the electrocatalyst for both reactions; however, the high cost and limited resources of this precious metal are withholding the commercialization of fuel cells.

The electrcatalytic activity of Pd, which was chosen as a target metal in this thesis work, is the second highest among pure metals for ORR, second only to Pt. This, combined with the fact that the cost of Pd is much lower than that of Pt, makes it an attractive alternative to Pt catalysts (Fig 1.9) [12].

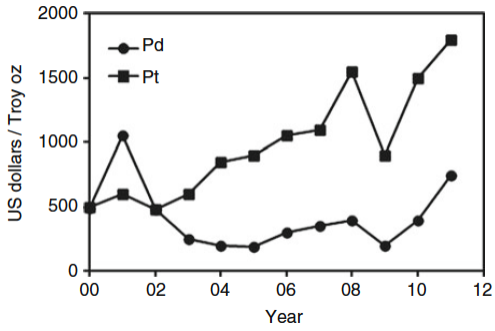

Fig. 1.9 - Comparison of the cost of Pd and Pt per troy ounce in the period of 2000-2011.

It is well known that the electrocatalytic activity of bulk, polycrystalline Pd for ORR is at least five times lower than that of Pt, which prevents Pd from being used directly in fuel cells, even though it is less expensive.

In the recent past years, great efforts have been dedicated to improve the activity of Pd by surface modification of the catalyst support and by alloying it with non-precious metals. Now the challenges include the design of inexpensive, stable, durable and robust catalysts for the electrochemical reaction at the cathode, which needs to be addressed, via:

1. Improvement of current platinum-based catalysts for the oxygen reduction reaction (ORR) and the hydrogen oxidation reaction (HOR) or substitution by platinum-group metal (PGM) free catalysts, in order to meet the platinum cost and design constraints for commercial applications [13].
2. Development of more durable ORR and HOR catalysts, resilient to the voltage-cycles occurring during the transient operation of fuel cell vehicles [14,15].

3. Replacement of the currently used high-surface area carbon supports (e.g., Ketjen blacks) with more corrosion-resistant materials (e.g., fully graphitized carbon supports or noncarbon-based supports) to minimize the damage caused by local hydrogen starvation [16,17] and during fuel cell start/stop processes [18,19].
4. Design of HOR catalysts that have no activity for the ORR [20] and their integration into anode electrodes, which is an alternative approach to mitigating degradation caused by start/stop.
5. Optimization of electrode performances with new electrode materials (catalysts, catalyst supports, and ionomers [14]), particularly for high-current density operation with low platinum loadings.
6. Design of high-performing gas-diffusion media (DM) and microporous layer (MPL) coatings, that are resistant to contaminations [21] and aging caused by fuel cell system transients (i.e., extensive voltage-cycling, start/stop [22]).
7. Development of ab-initio catalyst models, particularly for the ORR catalysis [23] and in situ diagnostic methods in order to provide effective methods (i.e. doping) required for the screening and implementation of improved electrode materials designs.

Bibliography

[1] Kordesch, K.; Simader, G. *Fuel Cells and Their Applications VCH* **1996**.

[2] Carette, L.; Friedrich, K.A.; Stimming, U. *ChemPhysChem* **2000**, *1*, 162.

[3] Yeager, E. *Electrochim. Acta* **1984**, *29*, 1527.

[4] Adzic, R.R.; Wang, J.X. *J. Phys. Chem. B* **1998**, *102*, 8988.

[5] Damjanovic, A.; Brusic, V. *Electrochim. Acta* **1967**, *12*, 615.

[6] Yeager, E.; Razaq, M.; Gervasio, D.; Razaq, A.; Tryk, D. *J. Electrochem. Soc.* **1992**, *92*, 440.

[7] Shao, M.H.; Liu, P.; Adzic, R.R.; *J. Am. Chem. Soc.* **2006**, *128*, 7408.

[8] Griffith, J.S.; *Proc. R. Soc. Lond. A* **1956**, *235*, 23.

[9] Yeager, E.; *J. Electrochem. Soc.* **1981**, *128*, 160C.

[10] Steele, B.C.H.; Heinzel, A. *Nature* **2001**, *414*, 331.

[11] Gottesfeld, S.; Zawodzinski, T. *Adv. Electrochem. Sci. Eng.* **1997**, *5*, 195.

[12] Shao, M. Electrocatalysis in Fuel Cell, Springer **2013**.

[13] Adzic, R.R.; Zhang, J.; Sasaki, K.; Vukmirovic, M.B.; Shao, M.; Wang, J.X.; Nilekar A.U.; Mavrikakis, M.; Valerio, J.A. *Uribe F.* **2007**, *46*, 249.

[14] Gasteiger. H.A.; Kocha, S.S.; Sompalli, B.; Wagner, F.T. *Appl. Catal. B: Environ.* **2005**, *56*, 9.

[15] Lefevre, M.; Proietti, E.; Jaouen, F,; Dodelet, J.P. *Science* **2009**, *324*, 71.

[16] Shao, M.H.; Liu, P.; Adzic, R.R.; *J. Am. Chem. Soc.* **2006**, *128*, 7408.

[17] Tarasevich, M.R.; Sadkowski, A.; Yeager, E. *Plenum* **1983**, *7*, 301.

[18] Zhang, J.; Vukmirovic, M.B.; Xu, Y.; Mavrikakis, M.; Adzic, R.R. *Angew. Chem. Int. Ed.* **2005**, *44*, 2132.

[19] Xu, Y.; Greeley, J.; Mavrikakis, M. *J. Am. Chem. Soc.* **2005**, *127*, 12823.

[20] Stamenkovic, V.R.; Fowler, B.; Mun, B.S.; Wang, G.; Ross, P.N.; Lucas, C.A.; Markovic, N.M. *Science* **2007**, *315*, 493.

[21] Markovic, N.M.; Adzic, R.R.; Cahan, B.D.; Yeager, E.B. *J. Electroanal. Chem.* **1994**, *377*, 249.

[22] Kondo, S.; Nakamura, M.; Maki, N.; Hoshi, N. *J. Phys. Chem. C* **2009**, *113*, 12625.

[23] Shao, M.H.; Huang, T.; Liu, P.; Zhang, J.; Sasaki, K.; Vukmirovic, M.B.; Adzic, R.R.; *Langmuir* **2006**, *22*, 10409.

CARBON-HALOGEN BOND CLEAVAGE

2.1 Overview

The electrochemical activation of carbon–halogen bonds is a widely explored field in organic electrochemistry. The great interest for this process is due to the important roles it plays in synthetic and environmental applications, especially the abatement of volatile polychlorinated organic compounds.

Electron transfer to an organic halide, RX, by reaction with a homogeneous electron donor as well as by electrochemical or other means, results in the rupture of the carbon-halogen σ bond to give a free radical and a halide ion. The process is known as dissociative electron transfer (DET) and can occur by two alternative mechanisms. Electron transfer (ET) and bond breaking can occur either by a stepwise mechanism (Eqs. 2.1-2.2), with the intermediate formation of a radical anion $RX^{\bullet -}$ or in a concerted way in which ET and bond fragmentation occur in a single step (Eq. 2.3).

$$RX + e^- \rightleftharpoons RX^{\bullet -} \quad [2.1]$$

$$RX^{\bullet -} \longrightarrow R^{\bullet} + X^- \quad [2.2]$$

$$RX + e^- \longrightarrow R^{\bullet} + X^- \quad [2.3]$$

$$R^{\bullet} + e^- \rightleftharpoons R^- \quad [2.4]$$

Depending on the value of the applied potential with respect to the reduction potential of $R^{\bullet}$, the latter may undergo typical radical reactions or be reduced to a carbanion R^- (Eq. 2.4). In some cases, it is thus possible to trigger either radical or ionic chemistry, by appropriately choosing the applied potential [1] In the case of stepwise mechanism, two energy barriers must be taken into account: the first one is related to the ET (Eq. 2.1) whereas the second is due to the carbon-halogen fragmentation (Eq. 2.2), i.e. the intramolecular electron transfer from the orbital initially accommodating the incoming electron (generally a π* orbital) to the C-X σ* orbital (see Fig. 2.1). A

voltammetric investigation on an extended series of aryl halides, affording a regular, well-defined sequence of increasingly more stable radical anion intermediates, has shown [2] that a kinetic parameter κ, defined as:

$$\kappa = -1.15\ (RT/F)\ /\ (\mathrm{d}E\mathrm{p}/\mathrm{dlog}v) \qquad [2.5]$$

or

$$\kappa = 1.857\ RT\ /\ [F(E_{p/2} - E_p)] \qquad [2.6]$$

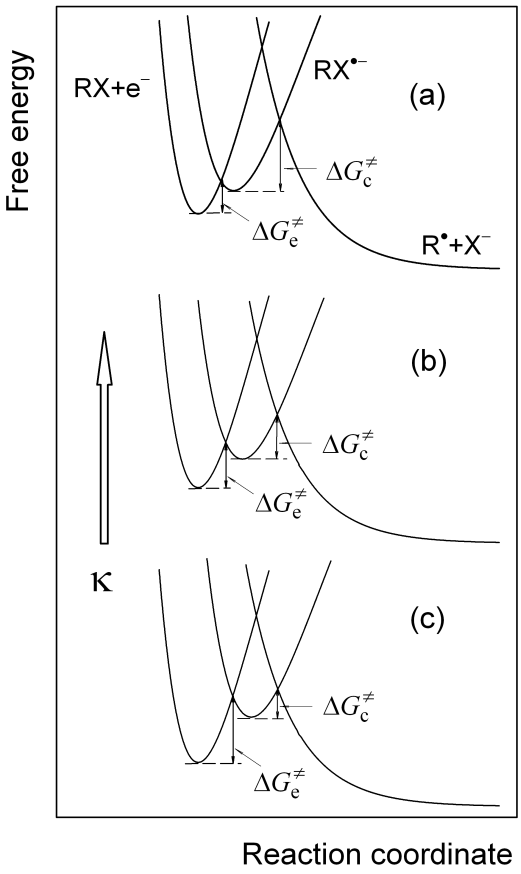

Fig. 2.1 - Potential energy diagrams for a dissociative electron transfer to R-X under Kinetic control of (a) the bond cleavage reaction, (b) both bond cleavage and electron transfer reactions and (c) electron transfer. The subscripts e and c stand for the electron transfer and bond rupture reactions, respectively.

is an efficient indicator of the relative kinetic influence of the above two barriers. In particular, the relative importance of the energy barrier associated with the ET with respect to the energy barrier of bond rupture regularly decreases with increasing κ. When $\kappa = 1$ the dissociative electron transfer process in kinetically controlled by the bond rupture (Eq. 2.2), the ET step (Eq. 2.1) being relatively fast. Conversely, when $\kappa < 0.5$ the ET step becomes the rate-determining step and κ coincides with the electron transfer coefficient, α.

The electrochemical reduction of organic halides is an important topic, not only for the stimulating and interesting mechanistic aspects, but also for the development of very useful electrosyntheses. In this connection, however, two major drawbacks must be considered. The first is the highly negative reduction potential required for the reduction of organic halides, which is an unfavourable aspect, both for the energetic cost and for the greater probability of concomitant undesired reduction processes. As is well known, the reduction potential becomes more negative in the series RI, RBr, RCl. The second problem is the possibility of parasitic reactions, in particular nucleophilic substitution, which lower selectivity and yields of the desired products. Furthermore, parasitic reactions are more important for the more easily reducible iodides, whereas chlorides are more resistant, but also more difficult to be reduced. For these reasons, much attention has been devoted to develop possible electrocatalytic processes and electrode materials for the activation of carbon-halogen bonds.

2.2 Heterogeneous electrocatalysis

In the last decade, investigations on the electrocatalytic cleavage of carbon-halogen bonds have usually dealt with electrocatalytic effects in terms of differences between reduction peak potentials obtained in the same conditions on the electrode surface tested as catalytic and on a suitable electrode, acting as an inert (or non-catalytic) electron source ensuring outer-sphere ET. The catalytic effect is therefore defined as:

$$\textit{Catalytic effect} = \Delta E_p = E_{p,\,\text{catalytic}} - E_{p,\,\text{non-catalytic}} \qquad [2.7]$$

Glassy carbon (GC), boron-doped diamond (BDD) and fluorinated boron-doped diamond (FBDD) have been tested as reference non-catalytic electrodes [3]. The reduction potential sequence of different model organic halides on the three carbon-based electrodes is GC > BDD > FBDD, actually a sequence of decreasing Lewis acidity of the reacting surfaces, considering that the GC surface is partially functionalized with hydroxyl and carboxyl groups [4], while BDD is predominantly hydrogen-terminated [5] and FBDD features a consistent number of fluoride atoms on its surface, resulting in an even more hydrophobic character [6], which however could exert a repulsive effect on the approaching halide leaving group of the reacting molecule. Accordingly, BDD would appear the most appropriate inert reference among the three surfaces tested. However, it is expensive and difficultly available, particularly in an electrode setup suitable for working in nonaqueous solvents; moreover, fundamental studies on the electrochemical reduction of organic halides in non-catalytic conditions have mostly been carried out on the more popular GC electrode; thus, the latter has been commonly adopted as the reference for evaluating electrocatalytic effects for RX reduction

Care should however be exercised in the choice of GC electrodes when accurate analysis of DET dynamics is desired, since their electrochemical performance may be strongly influenced by their surface microstructure [7,8]. Additionally, edge-plane sites and defects are prone to oxidation and therefore several oxygen-containing functional groups, mainly carbonyl, hydroxyl and carboxyl moieties, are present on the electrode surface. This significantly affects the reduction peak potential of RX, an increase of the oxygen-to-carbon ratio apparently causing a positive shift of E_p [9]. Besides the surface morphology and composition, the catalytic effect of GC depends also on DET mechanism, regularly increasing with increasing importance of the initial electron transfer step in the overall kinetics of the process [9]. The highest observed peak potential difference between differently activated GC surfaces is of the order of 0.1 V, found for some alkyl halides undergoing a concerted DET [9].

The use of electrocatalytic electrode surfaces is a convenient approach to the electrochemical activation of carbon–halogen bonds in mild conditions. All metals

having specific halide affinity could potentially possess electrocatalytic activity for C-X bond cleavage; comparative investigations [3,10-14] encompassing a wide range of metals also in terms of electrocatalytic scale [3] or volcano plot [10], are available in the literature. The earliest studies on the electrocatalytic reduction of organic halides were rather unintentional, mostly aimed at polarographic characterisation of the compounds. These studies used the non-innocent mercury electrode and actually halide adsorption phenomena and intermediate formation of organomercurials were found to play an important role in the process [15]. Also the first approach to silver in the '70s was fortuitous, consisting in clinical observation of the anomalously high response of an oxygen Clark-type sensor in the presence of anaesthetic halothane [16], an observation slowly exploited and rationalized in the following two decades [17,18].

More recently, synthetic [19-26] and, above all, environmental issues [14,27-34] have prompted remarkable acceleration, rationalization and refinement in this research field. In particular, Hg was put aside because of its environmental concerns and operating problems and investigations were concentrated on a series of solid electrodes that are significantly more catalytic than Hg, in particular Ag, which was found to possess a very high, reproducible catalytic activity for a very wide range of organic halides [12,35,36] including mono- and polyhaloalkanes [33,34,37,38] as well as aryl [2,36,39] benzyl [1,40] and heteroaryl [36] halides. Silver nanoparticles [41,42] and alloys [29] have also been considered. Pd, both as such and as palladiated surfaces of different non-metals and metals, like glassy carbon, Ag, Cu, Ni, Pt and Au [43-48], and Cu [13,32-34,49,50] have also been found to possess good electrocatalytic properties for the reduction of many classes of organic halides. Au is also sometimes considered. It is important to stress however that although the affinity of this metal for halide ions is intrinsically higher than that of Ag [51,52], its catalytic activity for C-X cleavage is practically hampered by the huge negative charge density of the metal at the operating potentials (as a consequence of its more positive pzc) [53].

The electrocatalytic properties of silver have already been exploited in several electrochemical processes, such as electrosynthesis of fine chemicals and pharmaceutical products [22,24-26,54], treatment of environmentally relevant organic halide pollutants, [27-34] and monitoring of some organic halides [17,18,55].

2.3 Role of DET mechanism

The electrocatalytic activity of silver towards the reduction of organic halides is strongly affected by the DET mechanism [2,36,39]. In the case of concerted DET, which is usually followed by aliphatic and benzyl halides, remarkable electrocatalysis is always displayed, independently of the nature of the halogen atom. It can be assumed [39] that an activated complex characterised by strong interactions between reacting C-X bond and the electrode surface is formed; as a result, the intrinsic activation energy barrier ($\Delta G_0^{\neq} = (\lambda_0 + BDE)/4$, with BDE = bond dissociation energy and λ_0 = solvent reorganisation energy) is significantly lowered. This decrease of $\Delta G^{\neq}$ results in a decrease of the required overpotential for the process, and hence in a positive shift of E_p with respect to the value observed on a non-catalytic electrode such as GC.

The extent of catalysis in concerted DETs is also strongly affected by possible specific adsorption of the electrogenerated halide ion and/or the starting organic halide [40], if the reduction potential at Ag is not so negative that electrostatic repulsions prevent adsorption of X^-. This specific adsorption effect decreases in the sequence $I^- > Br^- > Cl^-$.

Adsorption processes also result in alterations, sometimes conspicuous, of the reduction peak morphology with respect to the canonical diffusive feature. The case of benzyl halides $PhCH_2X$ provides a good example of the implications of reactant and product specific adsorption as a function of the reduction potential (Figure 2.2). In the chloride case, the reduction potential is far beyond the negative threshold for Cl^- adsorption; consistently, the molecule exhibits on Ag a single diffusive two-electron reduction peak (indicating that the radical undergoes easy reduction to anion at the same potential at which it is formed), albeit at a considerably less negative potential than at GC. A closer examination reveals that some slow adsorption of the reactant $PhCH_2X$ molecule does take place, although so weak that dissolved and adsorbed reactant molecules are reduced virtually at the same potential [40].

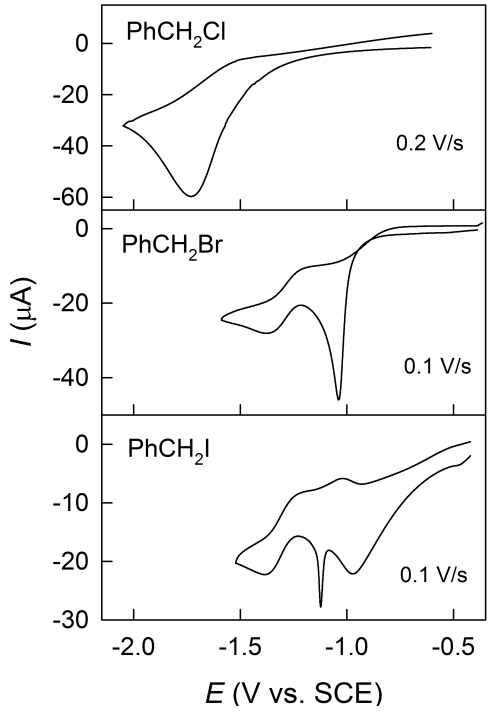

Fig. 2.2 - CV patterns for the reduction of benzyl halides on Ag in MeCN (from ref. [40])

In the case of $PhCH_2Br$, the DET process takes place within the potential range for specific Br^- adsorption. At slow scan rates, the molecules exhibits two irreversible reduction peaks attributed to the reduction of $PhCH_2Br$ (first peak) and $PhCH_2^{\bullet}$. The sharpness of the first peak indicates specific adsorption of one or both the reaction products. This peak gradually splits into two separate peaks as the scan rate is increased. Addition of Br^- in the reaction medium also brings about the same peak splitting even at low scan rates. These observations have been rationalized by considering the rate and degree of adsorption of Br^- during the voltammetric scan [40]. In the iodide case, the DET takes place well before the threshold potential for iodide anion adsorption and the adsorption of the $PhCH_2I$ reactant molecule at the Ag surface is so strong that reduction of adsorbed $PhCH_2I$ is observed as a sharp post peak at a potential about 150 mV more negative with respect to the diffusive one. (Figure 2.2) Combination of all the above effects results in a scale of catalytic effects (anodic shift of E_p: 0.45, 0.72 and 0.48 V for X = Cl, Br and I, respectively) which is at variance with the familiar silver/halide ion

interaction sequence in solution, i.e. $I^- > Br^- > Cl^-$. It is also worthwhile noticing that in both cases in which significant halide anion adsorption can take place, i.e. Br and I, a neat separation is observed between the potentials of first and second electron uptake; this allows to trigger selectively either radical or carbanion chemistry, as confirmed by preparative experiments [1].

The stepwise DET mechanism typically applies to aryl halides as a consequence of their ability to stabilize the incoming negative charge in a low-lying π* orbital delocalized on the aromatic system, so that the ensuing radical anion energy curve intersects those of the reagent and product. This charge delocalization implies a much lower polarization degree and a higher BDE of the carbon-halogen bond to be cleaved with respect to concerted DET cases. Aromatic bromides show catalytic effects on Ag possibly arising from interactions between the electrode and various species, mainly $ArBr^{\bullet -}$ and Br^-, involved in the DET. These catalytic effects have recently been shown [2] to be regularly linked to the degree of negative charge localization on the halogen atom in $ArBr^{\bullet -}$, suggesting that charge localization promotes specific interaction of the intermediate with the silver surface. Thus, for example, in the limiting case represented by 4-nitro-halobenzene, where the ET is circumscribed to the nitro group and therefore the negative charge in the radical anion is localized far away from the C-X bond, no electrocatalysis is displayed by Ag, independently of the type of the halogen atom [36]. Total absence of catalytic effects was also observed in the reduction of all aryl chlorides, at least in aprotic organic solvents [36,39]. This can be justified in terms of both the high value of the C-Cl BDE in aryl chlorides (396 kJ mol^{-1} for chlorobenzene) [56] and the negligible polarization of the C-Cl bond in the aryl radical anion intermediate $ArX^{\bullet -}$ [57]. Therefore, with organic chlorides in aprotic solvents, electrocatalysis appears to be clearly discriminated by the DET mechanism, being remarkable in all concerted DET cases and absent when the DET process follows a stepwise [36].

As compared to aryl chlorides, aryl bromides have lower BDEs and give rise to radical anions with higher C-X bond polarization [57]. Accordingly, when dealing with a bromide leaving group, significant electrocatalytic effects of Ag are observed, regardless of the mechanism of DET.

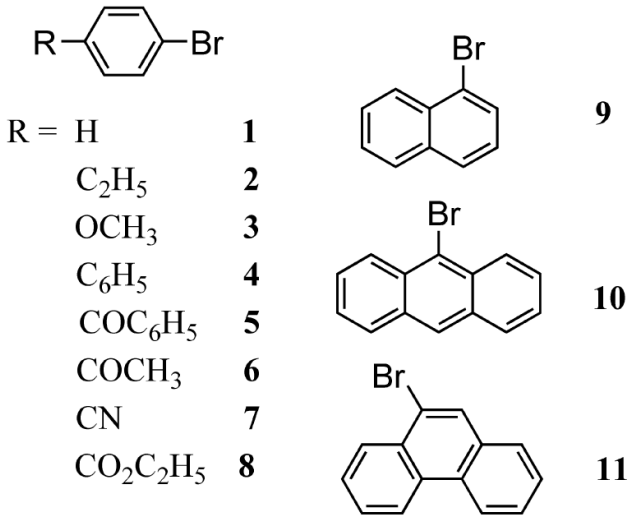

Chart 2.1

Such effects strongly depend on the molecular structure and a rationalization has been recently presented [2] by considering a wide series of aryl bromides (Chart 2.1) with different substituents appropriately selected so as to modulate the kinetics of decomposition of the intermediate radical anion $ArBr^{\bullet -}$, from the limiting case of a process controlled by the first heterogeneous ET, as in the case of bromobenzene, to the other extreme, in which the process is controlled by the intramolecular ET, i.e. the dehalogenation reaction, as in the case of bromoanthracene. These different kinetic regimes can be well described by a kinetic parameter κ. As shown in Figure 2.3a a plot of κ as a function of E_p is a straight line for both Ag and GC electrodes; κ increases as the peak potential becomes more positive, indicating that increasing the electron-withdrawing ability of the substituent or the number of fused aromatic rings stabilizes $ArBr^{\bullet -}$ and consequently shifts the kinetic regime of the DET process towards kinetic control by the bond rupture reaction. The two plots have quite different slopes, suggesting that also the electrocatalytic effect of Ag, $\Delta E_p = E_p^{Ag} - E_p^{GC}$, is significantly affected by molecular structure; in fact, ΔE_p is well correlated to κ, decreasing as the kinetic parameter increases (Fig. 2.3b).

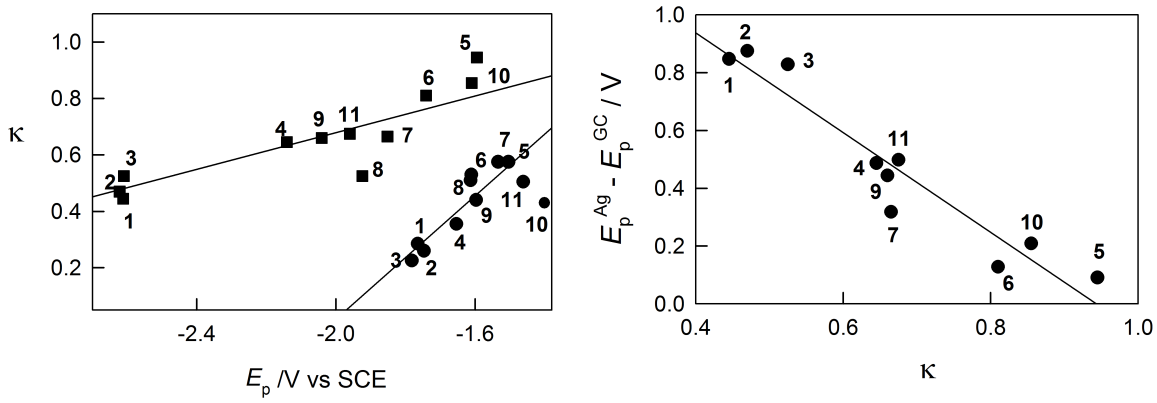

Fig. 2.3 - Correlation between the kinetic parameter κ and (a) the reduction peak potentials on GC (squares) and Ag (circles), (b) the catalytic effects of Ag, for the series of aryl bromides in Chart 2.1 (from ref. [2]).

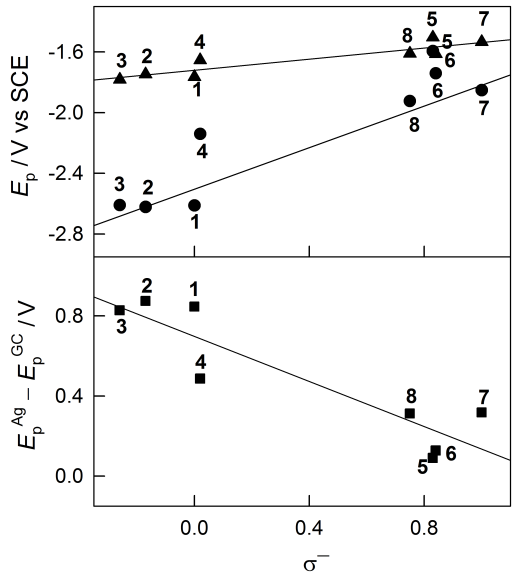

Fig. 2.4 - Reduction peak potentials measured on GC (circles) and Ag (triangles), and catalytic effects of Ag (squares) plotted vs σ^-, for the aryl bromides in Chart 2.1 (from ref. [2]).

The correlation between inductive effects in the aryl bromide molecular structure and Ag electrocatalytic effects is evidenced in the plots of E_p values at both GC and Ag electrodes vs Hammett substituent constants reported in Figure 2.4. As can be seen both electrodes show the same trend, i.e. E_p becomes more positive upon increasing the electron-withdrawing power of the substituent. For both electrodes, the dependence of E_p on σ^- can be fit to a linear equation of the classical form. It is worth

noting that reduction of the aromatic bromides at GC is ca. 4 times more sensitive to the substituents with respect to Ag, since at the catalytic Ag electrode, the molecular structure has a quite limited effect on E_p. It appears that the presence of the catalytic surface shifts, at least partially, the site of the negative charge in $ArBr^{\bullet -}$. Probably now the charge is mainly located at the bromine atom so that the electron-withdrawing power of the substituent becomes less important.

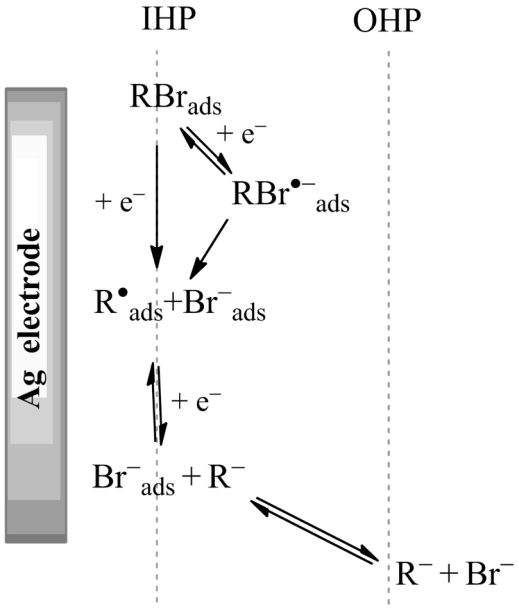

Scheme 2.1

Consistently with such observations a reduction mechanism has been proposed in which, as illustrated in Scheme 2.1, all reactions occur on the electrode surface. As a consequence, the potential energy profiles of reagents, intermediates and products at the catalytic surface are lowered with respect to the non-catalytic electrode (Fig. 2.5). This is mainly due to adsorption, especially in the case of $ArBr^{\bullet -}$ and the reduction products $Ar^{\bullet}$ and Br^-, which strongly interact with the Ag surface, whereas for the starting reagents ($ArBr + e^-$), their potential energy profile is lowered mainly because now the process occurs at less negative potentials. The combination of the decrease of the Gibbs free energy of the reaction and the enhancement of the cleavage rate of the radical anion

results in a positive shift of E_p at the catalytic electrode with respect to the non-catalytic electrode.

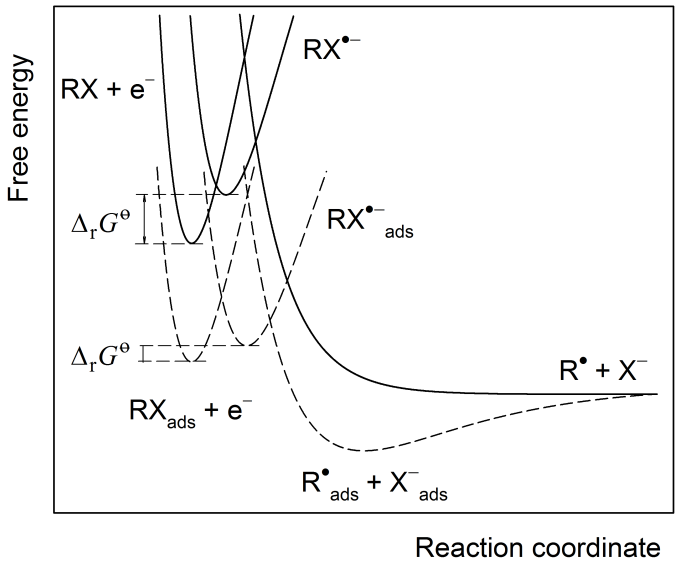

Fig. 2.5 - Potential energy profiles of reagents, intermediates and products for aryl bromide reduction at the non-catalytic (full lines) and catalytic surfaces (dotted lines).

In some cases there is a change of mechanism from stepwise to concerted on passing from the non-catalytic electrode to the catalytic one (Fig. 2.6). As before, the potential energy profiles of the reagents, intermediates and products of the catalytic process are lowered by surface interactions and by the increase of the reduction potential at the catalytic electrode. It is worth noting that the change of dissociative ET mechanism from stepwise at GC to concerted at Ag causes a drastic change of both the standard free energy, $\Delta_r G^\ominus$, and the activation free energy, $\Delta G^{\neq}$, of the ET.

It is well recognized that $E^\ominus_{stepwise}$ is considerably more negative than $E^\ominus_{concerted}$, even without taking into account adsorption phenomena, which would shift the latter to more positive potentials because of the preferential adsorption of the products with respect to the reagents. On the other hand, since the concerted DET involves rupture of a chemical bond, its activation free energy is often greater than that of the stepwise process. Catalysis arises from a combination of these kinetic and thermodynamic effects, both related to the ET to ArBr. The process at Ag has a remarkable

thermodynamic advantage over ET at a non-catalytic electrode, but loses something from the kinetic standpoint. The overall result, however, favours the catalytic surface with a net positive shift of the reduction potential.

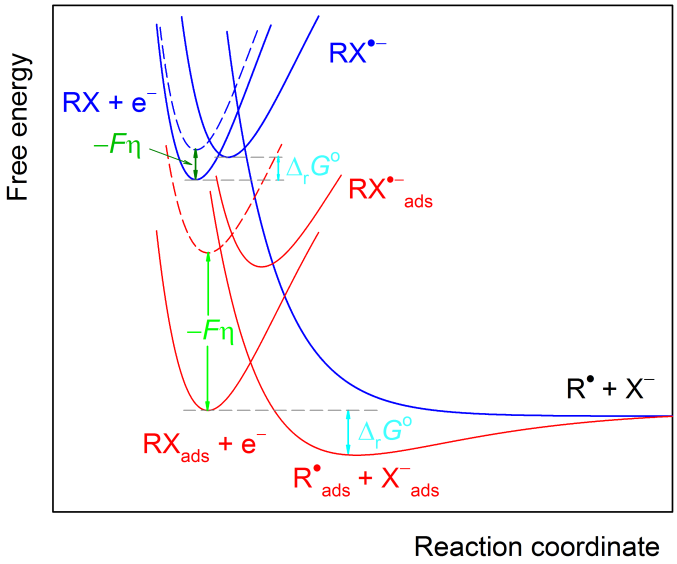

Fig. 2.6 - Potential energy profiles of reagents, intermediates and products for aryl bromide reduction at the non-catalytic (blue lines) and catalytic surface (red lines), in the case of DET mechanism change from stepwise to concerted.

More recently, several research groups tested the electrocatalytic activity of Ag nanoparticles [13,41]. These Ag nanoclusters show comparable activity to that of the bulk metal for a wide range of compounds. Ag/GC electrodes of suitable active surface can be employed in macroscale electrolyses for important catalytic electrosyntheses. For example, electrocatalytic reduction of benzyl chloride gives satisfactory yields of toluene or phenylacetic acid, the latter being the main product obtained in electrocaboxylation conditions, i.e., in CO_2-saturated CH_3CN. It is important to note that the performance of the Ag-modified GC electrode described here is comparable to that of bulk silver, but the catalyst metal load is very different, only a few micrograms of Ag per cm^2 being present in the former. This is a very important economic aspect, which should be taken into consideration in large-scale electrosynthesis processes.

In the same perspective, the electrocatalytic properties of Pd nanoparticles (Pd

NPs), synthesised by electrochemical reduction of an aqueous Pd salt, towards activation of carbon-halogen bonds have been extensively studied. A large number of substrates, including alkyl iodides [43,58] and bromides [45], aryl halides [59], benzyl bromides [46], allyl bromides [60], propargyl bromides [61] and vinyl bromides [62] have been investigated on smooth palladium electrodes, palladiated surfaces (such as Cu, Ni, Au, Pt, GC) and, above all, palladized silver.

However, although much attention is currently put on the discovery of new catalytic materials, little is known about the mesoscopic properties of the modified electrode surface and how its structure and stoichiometry can influence the electrochemical behaviour.

In this thesis work, the electrochemical reactivity of BnCl, which so far is considered as a benchmark process for electrocatalytic evaluation, will be studied on GC electrodes modified with metal nanoparticles. Particular attention will be focused on how electrocatalysis is affected by surface morphology and doping of the carbon support.

Bibliography

[1] Isse, A.A.; De Giusti, A.; Gennaro, A. *Tetrahedron Lett.* **2006**, *47*, 7735.

[2] Isse, A.A.; Mussini, P.R.; Gennaro, A. *J. Phys. Chem. C* **2009***, 113*, 14983.

[3] Bellomunno, C.; Bonanomi, D.; Falciola, L.; Longhi, M.; Mussini, P.R.; Doubova, L.M.; Di Silvestro, G. *Electrochim. Acta* **2005,** *50*, 2331.

[4] Dekanski, A.; Stevanović, J.; Stevanović, R.; Nicolić, B.Ž.; Jovanović, V.M. *Carbon* **2001***,* 39, 1195.

[5] Xu, J.; Granger, M.C.; Chen, Q.; Strojek, J.W.; Lister, T.E.; Swain, G.M. *Anal. Chem.* **1997**, *69*, 591A.

[6] Siné, G.; Ouattara, L.; Panizza, M.; Comninellis, C. *Electrochem. Solid State Lett.* **2003**, 6, D9.

[7] McCreery, R.L. *Chem. Rev* **2008**, *108*, 2646.

[8] Banks, C.E.; Davies, T.J.; Wildgoose, G.G.; Compton, R.G. *Chem. Commun.* **2005**, 829.

[9] Gennaro, A.; Isse, A.A.; Bianchi, C. L.; Mussini, P.R.; Rossi, M. *Electrochem. Commun.* **2009**, *11*, 1932.

[10] Langmaier, J.; Samec, Z. *J. Electroanal. Chem.* **1996**, *402*, 107.

[11] Sonoyama, N.; Hara, K.; Sakata, T. *Chem. Lett.* **1997**, *26*, 131.

[12] Rondinini, S.; Mussini, P. R.; Muttini, P.; Sello, G. *Electrochim. Acta* **2001**, 46, 3245.

[13] Isse, A.A.; Gottardello, S.; Durante, C.; Gennaro, A. *Phys. Chem. Chem. Phys.* **2008**, *10*, 2409.

[14] Schizodimou, A.; Kyriacou, G.; Lambrou, C. *J. Electroanal. Chem.* **1999**, *471*, 26.

[15] Peters, D. G. in *Organic Electrochemistry*, Lund, H.; Hammerich, O.; eds., Marcel Dekker, New York, 4th edn., **2001**, p. 341, and references therein cited.

[16] Dent, J. G.; Netter, K J. *Brit. J. Anaesth.* **1976**, *48*, 195.

[17] Albery, W.J.; Hahn, C E.; Brooks, W. N. *Brit. J. Anaesth.* **1981**, *53*, 447.

[18] Mount, A. R.; Appleton, M.S.; Albery, W. J.; Clark, D.; Hahn, C.E.W. *J. Electroanal. Chem.* **1992**, *334*, 155.

[19] Benedetto, M.; Miglierini, G.; Mussini, P.R.; Pelizzoni, F.; Rondinini, S.; Sello, G. *Carbohydr. Lett.* **1995**, *1*, 321.

[20] Rondinini, S.; Mussini, P.R.; Cantù, G.; Sello, G. *Phys. Chem. Chem. Phys.* **1999**, *1*, 2989.

[21] Rondinini, S.; Mussini, P.R.; Sello, G.; Vismara, E. *J. Electrochem. Soc.* **1998**, *145*, 1108.

[22] Gennaro, A.; Sánchez-Sánchez, C.M.; Isse, A.A.; Montiel, V. *Electrochem. Commun.*

2004, *6*, 627.

[23] Germini, M.; Guglieri, S.; Santarsiero, R.; Vismara, E. *Tetrahedron: Asymmetry* **2005**, *16*, 243.

[24] Isse, A.A.; Ferlin, M.G.; Gennaro, A. *J. Electroanal. Chem.* **2005**, *581*, 38.

[25] Scialdone, O.; Galia, A.; Filardo, G.; Isse, A.A.; Gennaro, A. *Electrochim. Acta* **2008**, *54*, 634.

[26] Scialdone, O.; Galia, A.; Errante, G.; Isse, A.A.; Gennaro, A. *Electrochim. Acta* **2008**, *53*, 2514.

[27] Rondinini, S.; Mussini, P.R.; Specchia, M.; Vertova, A. *J. Electrochem. Soc.* **2001**, *148*, D102.

[28] Georgolios, N.; Kyriacou, G.; Ritzoulis, G. *J. Appl. Electrochem.* **2001**, *31*: 207.

[29] Rondinini, S.; Vertova, A. *Electrochim. Acta* **2004**, *49*, 4035.

[30] Xu, Y.; Zhu, Y.; Zhao, F.; Ma, C. *Appl. Catal. A* **2007**, *324*, 83.

[31] Durante, C.; Isse, A.A.; Sandonà, G.; Gennaro, A. *Appl. Catal. B: Environ.* **2009**, *88*, 479.

[32] Huang, B.; Isse, A.A.; Durante, C.; Wei, C.; Gennaro, A. *Electrochim. Acta* **2012**, *70*, 50.

[33] Isse, A.A.; Huang, B.; Durante, C.; Gennaro, A. *Appl. Catal. B: Environ* **2012**, 126, 347.

[34] Durante, C.; Huang, B.; Isse, A.A.; Gennaro, A. *Appl. Catal. B: Environ.* **2012**, 126, 355.

[35] Rondinini, S.B.; Mussini, P.R.; Crippa, F.; Sello, G. *Electrochem. Commun* **2000**, *2*, 491.

[36] Isse, A.A.; Berzi, G.; Falciola, L.; Rossi, M.; Mussini, P.R.; Gennaro, A. *J. Appl. Electrochem.* **2009**, *39*, 2217.

[37] Isse, A.A.; Sandonà, G.; Durante, C.; Gennaro, A. *Electrochim. Acta* **2009**, *54*, 3235.

[38] Scialdone, O.; Guarisco, C.; Galia, A.; Herbois, R. *Electroanal. Chem.* **2010**, *641*, 14.

[39] Isse, A.A.; Falciola, L.; Mussini, P.R.; Gennaro, A. *Chem. Commun.* **2006**, 344.

[40] Isse, A.A.; De Giusti, A.; Gennaro, A.; Falciola, L.;. Mussini, P.R. *Electrochim. Acta* **2006**, *51*, 4956.

[41] Isse, A.A.; Gottardello, S.; Maccato, C.; Gennaro, A. *Electrochem. Commun.* **2006**, *8*, 1707.

[42] Rondinini, S.; Aricci, G.; Krpetic, Z.; Locatelli, C.; Minguzzi, A.; Porta, F.; Vertova, A. Fuel Cells **2009**, *9*, 253.

[43] Simonet, J. Electrochem. Commun. **2007**, *9*, 1840.

[44] Simonet, J.; Poizot, P.; Laffont, L. J. Electroanal. Chem. **2006**, *591*, 19.

[45] Jouikov, V.; Poizot, P.; Simonet, J. J. Electrochem. Soc. **2009**, *156*, E171.

[46] Jouikov, V.; Simonet, J. Electrochem. Commun. **2010**, *12*, 331.

[47] Simonet, J., Electrochem. Commun. **2010**, *12*, 520.

[48] Poizot, P.; Simonet, J. Electrochim. Acta **2010**, 56, 15.

[49] Fedurco, M.; Sartoretti, J.; Augustynski, J. Langmuir, **2001**, 17, 2380.

[50] Simonet, J. Electrochem. Commun. **2008**, 10, 647.

[51] Ignaczak, A.; Gomes, J.A.N.F. *J. Electroanal. Chem.* **1997**, 420, 71.

[52] Koper, M.T.M.; van Santen, R.A. *Surf. Sci.* **1999**, 422, 118.

[53] Fedurco, M.; Sartoretti, C. J.; Augustynski, J. *Langmuir* **2001**, *17*, 2380.

[54] Isse, A.A.; Gennaro, A. *Chem. Commun.* **2002**, 2798.

[55] Moorcroft, M.J.; Prado, C.; Compton, R.G.; McPeak, H.B.; Hahn, C.E.W. *J. Electroanal. Chem.* **2002**, *528*, 12.

[56] Lias, S.G.; Bartmess, J.E.; Liebman, J.F.; Holmes, J.L.; Levin, R.D.; Mallard, W.G. **1988**, *17*, Supplement 1.

[57] Enemærke, R.J.; Christensen, T.B.; Jensen, H.; Daasbjerg, K.J. *Chem. Soc., Perkin Trans.* **2001**, *2*, 1620.

[58] Simonet, J. *Electrochem. Commun.* **2005**, *7*, 74.

[59] Jouikov, V.; Simonet, J. *Electrochem. Commun.* **2010**, *12*, 781.

[60] Simonet, J.; *Electrochem. Commun.* **2011**, *13*, 1417.

[61] Jouikov, V.; Simonet, J. *Electrochem. Commun.* **2012**, *15*, 93.

[62] Poizot, P.; Simonet, J. *Electrochem. Commun.* **2012***, 23*, 137.

TECHNIQUES and INSTRUMENTS

3.1 Linear Sweep and Cyclic Voltammetry

Linear sweep voltammetry belongs to the potential sweep methods, in which the current is recorded while the electrode potential is changed linearly with time between two values. The initial potential, E_1, is usually the one where there is no electrochemical activity and the final potential, E_2, is the one where the reaction is under mass transport controlled. In linear sweep voltammetry, the scan stops at E_2, whereas in cyclic voltammetry, the sweep direction is reversed when the potential reaches E_2 and the potential is swept back to E_1, usually with the same scan rate. This constitutes a single cyclic voltammogram (Fig. 3.1) [1]. Choosing the waveform parameters is the most important step when preparing the experiment. The starting and reversal potentials determine the driving force for electron transfer and the oxidation state of the species involved. Appropriate choice of the potentials will thus determine whether a species is formed or consumed, and whether the reaction is under kinetic or mass transport control. In fact, in Chapter 6 a linear sweep method will be used for the characterization of Mesoporous Carbon electrodes towards ORR activity, because the oxygen peak is located at a very positive potential (around 0.5-0.6 V) and is therefore hidden by the peak of metal oxide stripping. It is necessary to use linear sweep voltammetry in order to avoid the corresponding oxide formation peak during the reverse scan of CV.

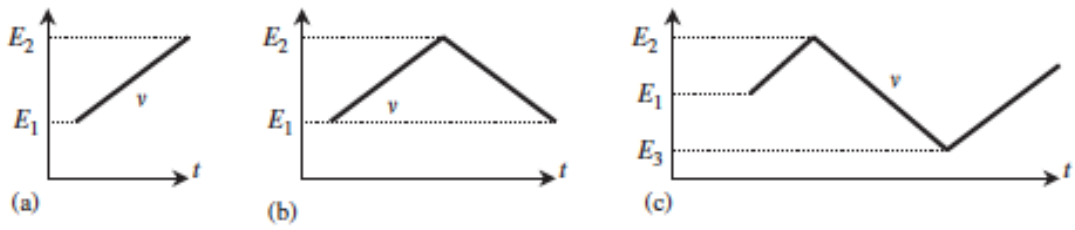

Fig. 3.1 - Waveforms used in linear sweep (a) and cyclic voltammetry (b and c). E_1, E_2 and E_3 are the starting and reversal potentials while v is the scan rate.

The potential scan rate is a very important experimental parameter as it sets the timescale of the experiment. In fact, in the case of coupled homogeneous reactions, the value of v will determine whether intermediates are formed or consumed and to what extent. Typically v values in the range from a 10 mV sec^{-1} to 10 V sec^{-1} are used, although if necessary higher sweep rates can be used.

A typical cyclic voltammogram for a diffusion-controlled electron transfer reaction on an inert planar electrode is shown in Figure 3.2. Its shape derives from the evolution of the concentration profiles resulting from the potential sweep and planar diffusion. Changing the electrode potential produces new surface concentrations for O and R and induces their diffusion between the bulk solution and the electrode [1,2].

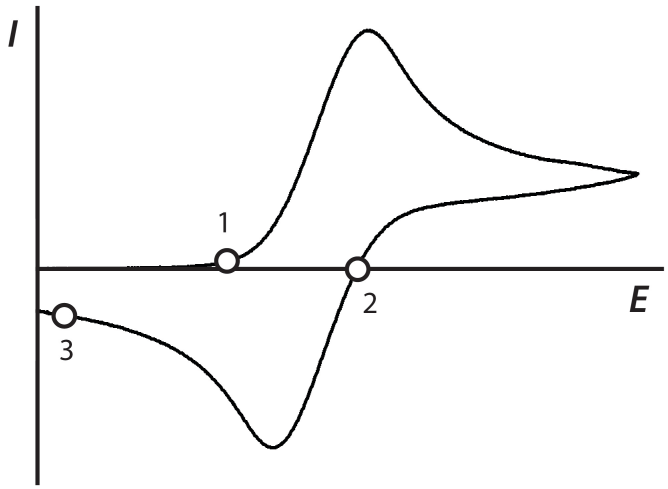

Fig. 3.2 – A Cyclic voltammogram of a reversible redox reaction.

Between points 1–2, species O is consumed at the electrode and an overall reduction current is observed, whereas in the potential zone between points 2–3, O is regenerated by oxidation of R and an overall oxidation current is observed.

The key features of the cyclic voltammogram are the peak height and the peak-peak separation. The peak current is given by Randles-Sevčik equation, which shows that the peak current is proportional to the square root of the sweep rate (Eq. 3.1).

$$i_p = 0.4463nFAC_O^* \left(\frac{nF}{RT}\right)^{1/2} D_O^{1/2} v^{1/2} \qquad [3.1]$$

where n is the number of electron exchanged, F is the Faraday constant, R (8.314 J/mol K) is the universal gas constant, T (K) is the absolute temperature, A (cm^2) is the electrode surface area, v (V/s) is the potential scan rate, D_O (cm^2/s) is the diffusion coefficient and C_0^* (mol/cm^3) is the bulk concentration of the redox specie. The diagnostic criteria for cyclic voltammetry of a reversible electron transfer are:

$$i_p \propto v^{1/2}$$

$$\left|\frac{i_{pa}}{i_{pc}}\right| = 1$$

$$E_p \text{ is indipendent of } v$$

$$\Delta E_p = E_{pa} - E_{pc} = \left|E_p - E_{p/2}\right| = \frac{57}{n} \text{mV } at \text{ } 298 \text{ } K$$

The shape of the voltammogram changes significantly when the rate of mass transport overcomes the rate of electron transfer. When the mass transfer coefficient is comparable to the rate constant for electron transfer, the voltammogram is almost identical to the diffusion-controlled one (Figure 3.2). However, when the mass transfer coefficient is increased, i.e. at large values of v, the voltammogram becomes drawn out. The peaks broaden and the peak separation increases because a bigger overpotential is needed to reach the same rate of electron transfer. As the rate of mass transport increases, the reverse peak becomes less and less pronounced. In the limit of a very slow rate of electron transfer, i.e. irreversible electron transfer, the reverse peak disappears. The diagnostic criteria for irreversible systems are:

$$i_p \propto v^{1/2}$$

No reverse peak

E_p shifts to higher overpotentials as v increases

$$\left|E_p - E_{p/2}\right| = \frac{48}{\alpha n} mV \text{ } at \text{ } 298 \text{ } K$$

3.2 Rotating Disk Electrode

The rotating disc electrode (RDE) is the classical hydrodynamic electroanalytical technique used to limit the diffusion layer thickness.

Compared to transient methods such as stationary electrode voltammetry, hydrodynamic methods have several advantages including (1) rapid establishment of a high rate of steady-state mass transport and (2) easily and reproducibly controlled convection over a wide range of mass transfer coefficients. There are also drawbacks: (1) in many instances, the construction of electrodes and cells is not easy and (2) the theoretical treatment requires the determination of the solution flow velocity profiles (as functions of rotation rate, viscosities and densities) as well as solution of the electrochemical problem; very few cases yield exact solutions. The RDE consists of a disk (e.g. of metal, glassy carbon or graphite) set into an insulating (PTFE, PEEK) surround. The electrode is rotated about its vertical axis (Figure 3.3) [1], typically between 400 and 10,000 rpm. The theory for the hydrodynamics at the RDE [2] assumes that the electrode is uniformly accessible and affords a precise and reproducible control of the convection and diffusion of reactant to the electrode. Hence, RDE can be used to study the kinetics of interfacial processes. Considering the concentration profile shown in Fig. 3.3, the limiting current is defined by the Levich equation:

$$i_l = 0.620nFACD^{2/3}v^{-1/6}\omega^{1/2} = BC\omega^{1/2} \qquad [3.2]$$

Where B is known as the Levich costant, v is the kinematic viscosity and ω (rad/s) is the angular velocity of the electrode.

The limiting current is achieved by recording a linear sweep voltammogram at a low scan rate (1–10 mV s^{-1}) from an initial potential where no reaction occurs to a final potential in the region where the process becomes under diffusion control. The classical RDE experiment consists in recording a series of linear sweep voltammograms at a low scan rate for a range of ω values.

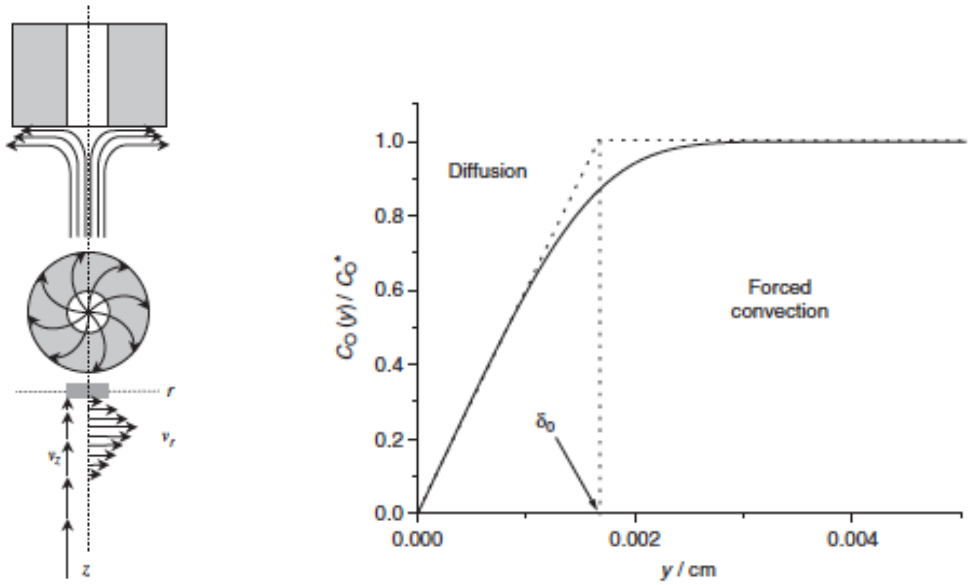

Fig. 3.3 - (a) Streamlines for flow and vector representation of fluid velocities near a rotating disk electrode, (b) steady-state concentration profile at the RDE.

The Levich equation predicts that a plot of the limiting current vs. the square root of ω should be a straight line passing through the origin with a slope determined by the number of electrons, the geometric area of the electrode, the diffusion coefficient, the bulk concentration of O and the kinematic viscosity of the solution, v. When the redox process is reversible, the shape of the wave does not depend on ω. Hence, at any potential, the current should, like the limiting current, be proportional to $\omega^{1/2}$. If the shape of the curve depends on ω, then the redox process is kinetically limited by the electron transfer. In this case, one can measure the current at a series of fixed potentials along the voltammogram and for each potential plot the inverse of the current vs. $\omega^{1/2}$. This is known as a Koutecký–Levich plot and follows the Koutecký–Levich equation:

$$\frac{1}{i} = \frac{1}{i_k} + \frac{1}{i_d} = \frac{1}{i_k} + \frac{1}{BC\omega^{1/2}} \qquad [3.3]$$

where i_k is the kinetically controlled current that would be obtained for $\omega^{-1/2} = 0$, i.e. for an infinite rotation speed where the mass transfer would be so efficient that the surface concentration of C_o would be equal to C_o^*.

The result of the linearization is known as the diffusion limited current and is denoted as i_d. However, when we want to do some qualitative comparison, for example in ORR activity, it is more appropriate to use the normalized current, which can be calculated if the active surface area of the electrode is known.

In our case, where metal NPs are deposited on a carbon electrode, it is possible to calculate the active surface area from:

$$AA_{H-UPD}(cm^2) = \frac{Q_{H-UPD}(C)}{210\ (\mu C/cm^2)} \times 10^6 \qquad [3.4]$$

$$AA_{CO}(cm^2) = \frac{Q_{CO}(C)}{420\ (\mu C/cm^2)} \times 10^6 \qquad [3.5]$$

$$AA_{Cu-UPD}(cm^2) = \frac{Q_{Cu-UPD}(C)}{420\ (\mu C/cm^2)} \times 10^6 \qquad [3.6]$$

In this work, and in particular in Chapter 6 - Mesoporous Carbon, the first two methods (Eqs. 3.4, 3.5) were used to calculate the active surface area. Once i_k is measured, it is possible to calculate the *specific activity* (Eq. 3.7) and *mass activity* (Eq. 3.8) of the catalyst.

$$Specific\ activity = \frac{i_k(A)}{AA\ (cm^2)} \qquad [3.7]$$

$$Mass\ activity = \left[\frac{i_k(A)}{w_{Met}(g)}\right] \qquad [3.8]$$

3.3 Electrochemical Impedance Spectroscopy

Impedance spectroscopy is an extremely powerful method for the investigation of electrical properties of materials and processes at the electrode-solution interface. When the impedance spectroscopy is applied to electrochemical systems we call it electrochemical impedance spectroscopy (EIS). The use of EIS is based on the idea that the electrochemical systems are comparable to electrical circuits where the physical and chemical phenomena, which constitute an electrochemical process, are associated with the circuit elements that interact with the passage of current. Some of the most important phenomena are: (1) the charge-transfer resistance; (2) the diffusion at the electrode of the redox species; (3) the interfacial capacitance; (4) the ET overpotential; (5) adsorption and desorption processes.

Each of these stages may be modelled as an element or combination of elements of an electrical circuit. The problem is to distinguish each contribution within the global response and assign it to the right stage. This technique is used in the study of batteries, fuel cells, semiconductors, ceramic materials, biosensors, corrosion processes etc.

Ohm's law defines resistance as the ratio between the voltage and the current, and its use is limited to resistors.

$$R = V/I \qquad [3.9]$$

However, electrochemical systems have a much more complex behaviour than a simple resistor; so from this point of view, an impedance is better suited than a resistor to describe an electrochemical system.

$$Z(\omega) = Z_{re} + jZ_{im} \qquad [3.10]$$

where $j = (-1)^{1/2}$.

A graphical representation of the impedance of an electrochemical system takes the form of a Nyquist or Bode plot (Fig. 3.4) [3]. In the Nyquist plot (Fig. 3.4a), the experimental data points measured at different frequencies are put in a graph by plotting

the imaginary part against the real one corresponding to the frequency, ω_i. Bode plots express the impedance as a function of frequency and can be of two types: one describes the dependence of the impedance module of the frequency (Fig. 3.4b), and the other expresses the dependency of the phase on frequency (Fig. 3.4c).

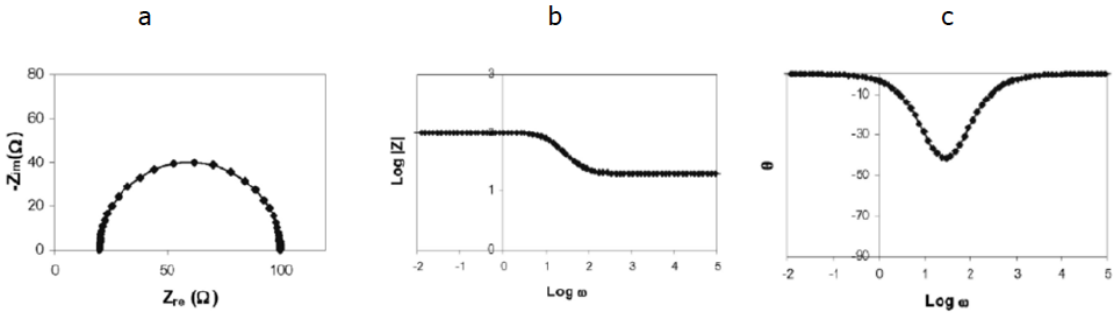

Fig. 3.4 - (a) Nyquist Plot, (b) Bode plot for the module of frequency |Z|, (c) Bode plot for the phase of frequency θ.

EIS data are obtained by fitting Nyquist or Bode diagrams to equivalent circuit models. An equivalent circuit model is a combination of resistances, capacitances and inductances that mimic the same response of electrochemical systems, in which each element represents a physicochemical process that contributes to the impedance of the electrochemical cell. In reality, some phenomena such as the diffusion cannot be modelled by simple circuit elements; in these cases, the appropriate electrochemical elements are introduced as a constant phase element (CPE) or the diffusion element of Warburg.

The equivalent circuit used in chapter 4 to extract EIS parameters from HOPG substrates consists in a serial resistance, R_S, which accounts for the solution Ohmic drop, connected to a loop with the charge transfer resistance (R_{ct}) and a constant phase element, which accounts for non-ideal diffusion phenomena, in parallel with a capacitor representing the capacitive contribution of the double-layer (C_{dl}) [4].

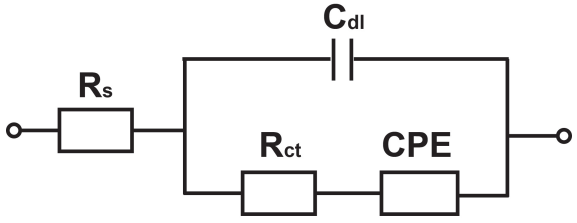

Fig. 3.5 - EIS equivalent circuit.

3.4 X-Ray Photoelectron Spectroscopy

X-ray photoelectron spectroscopy is a powerful surface technique to measure the binding energy (E_B) of electrons in matter. This technique is based on the *photoelectric effect* explained by Einstein in 1905 [5] and was developed during the 60's of the last century by K. Siegbahn and his research group. Figure 3.6 shows a schematic representation of the XPS experimental setup usually adopted in surface science studies.

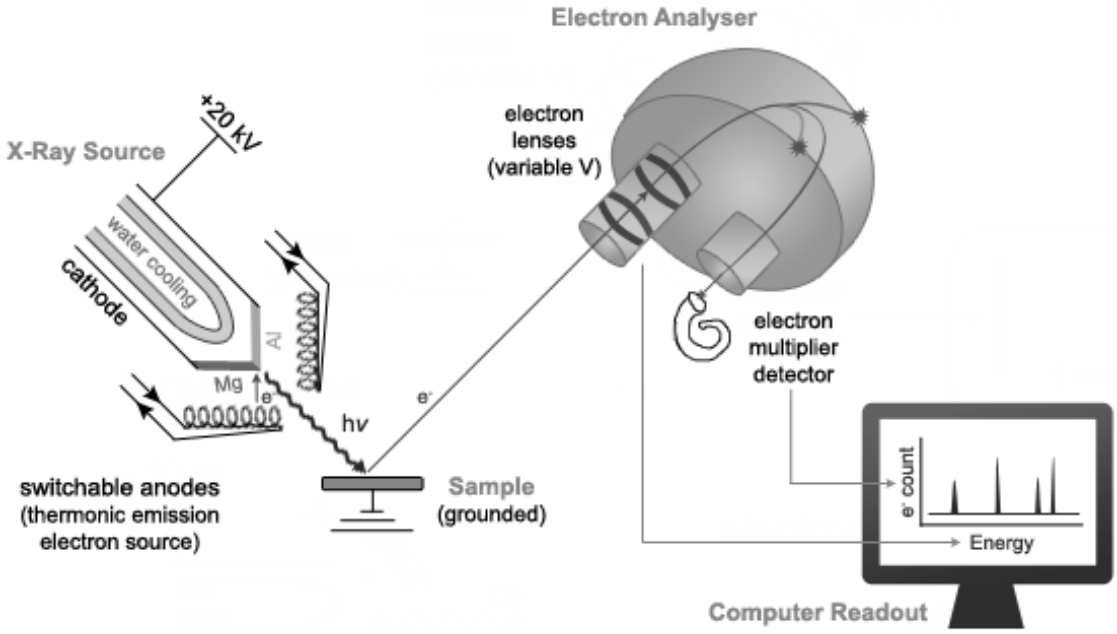

Fig. 3.6 - Schematic representation of XPS setup.

When X-rays irradiate a sample, the photon energy is used partially to ionize the atom and accelerate the photoelectrons that are emitted from the sample. Since *energy is conserved*, the kinetic energy (E_K) of the photoelectrons is related with the E_B and to the X-rays energy ($h\nu$) by the formula:

$$E_K = h\nu - E_B \qquad [3.11]$$

The electronic hole that remains in the atomic level that has been ionized by the interaction with the X-ray photon is refilled with a second electron of higher energy. The energy relaxations take place through two different processes, the *X-ray fluorescence*, and the *Auger emission*, which are competitive processes; the first has a higher cross section than the second for "heavy" elements (Z > 35), while the second is more favoured for "light" elements (Z < 35). Therefore, if $h\nu$ and E_B are known, it is possible to predict E_K of the emitted photoelectron. When a photoelectron is emitted, it may have basically two fates: it may be emitted without energy loss, giving an elastic peak in the spectrum, or it may undergo an inelastic diffusion losing some of its energy and contributing to the spectrum base line. The analyzer can discriminate between the different photoelectron energies, giving a spectrum of *intensity* (counts per second) versus E_B.

The XPS technique allows to identify and quantify the chemical elements present in the sample; the atomic concentration of the identified element i is [6]:

$$C_i^{\%} = \frac{A_i}{S_i} \cdot \frac{1}{\sum_{j=1}^{n} \frac{A_j}{S_j}} \cdot 100 \qquad [3.12]$$

where A_i is the area below the element peak (which has been previously subjected to the subtraction of the inelastic background due to Bremsstrahlung effect), whereas S_i is the sensibility factor, which is given by [7]:

$$S_i = K \frac{d\sigma_k}{d\Omega} \Lambda_e \qquad [3.13]$$

in which K is an instrumental factor usually taken as kinetic energy-independent.

3.5 Scanning Tunnelling Microscopy

A scanning tunnelling microscope (STM) is an instrument for imaging surfaces at the atomic level, developed in 1981 by Gerd Binnig and Heinrich Rohrer (at IBM Zürich). The instrument has two main important features [8]:

1. It is a local probe because of the particular geometry of the probing metal electrode, which is an extremely (atomically) sharp tip;
2. It is a proximal probe because of the close proximity of the probe tip and the sample surface, required for obtaining high spatial resolution.

The principle of STM is based on the strong distance dependence of the quantum mechanical tunnelling effect (Fig.3.7). First, a voltage bias is applied and a thin metal tip is brought in close proximity of the sample surface. At a distance of only a few angstroms, the overlap between tip and sample electron wave functions is large enough for a tunnelling current I_t to occur. The tunnelling current is given by:

$$I_t \sim e^{-2Kd} \qquad [3.14]$$

where d denotes the tip-sample distance and K is a constant depending on the height of the potential barrier.

At close range, fine control of the tip in all three dimensions is usually piezoelectric, maintaining tip-sample separation typically in the range of 4-7 Å, which is the equilibrium position between attractive and repulsive interactions. In this situation, the voltage bias will cause electrons to tunnel between the tip and sample, creating a current that can be measured.

Once tunnelling is established, the tip's bias and position with respect to the sample can be varied (with the details of this variation depending on the experiment) and data are obtained from the resulting changes in current.

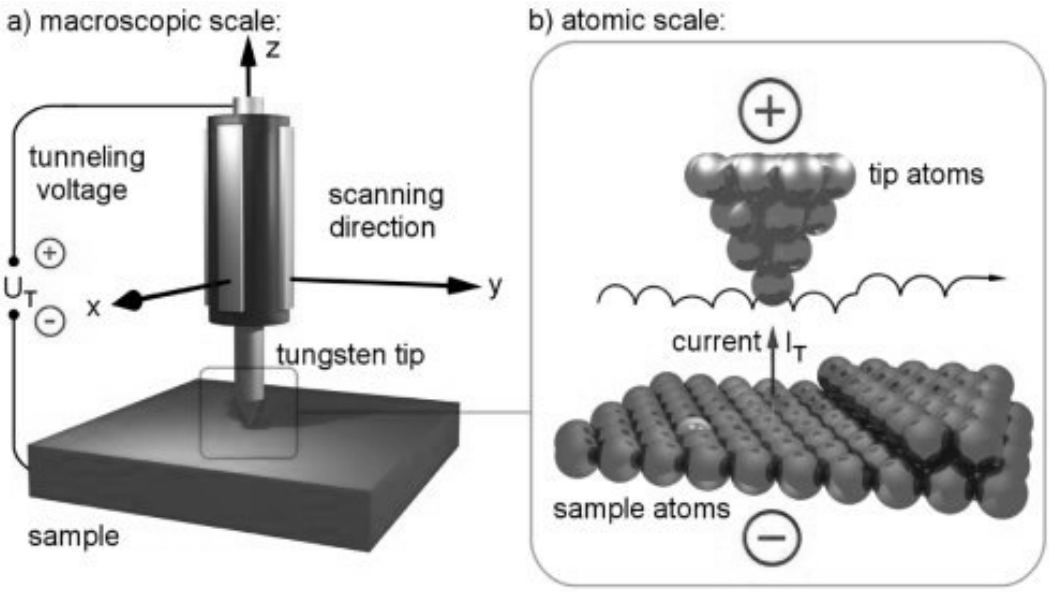

Fig. 3.7 - Principle of scanning tunnelling microscopy.

This ability to perform local experiments, together with the ability to characterize non-periodic surface structures can be regarded as the main advantages of STM compared with other surface analysis techniques [8].

3.6 Transmission and Scanning Electron Microscopy

Transmission electron microscopy (TEM) was invented and developed by Max Knoll and Ernst Ruska in 1931, whereas scanning electron microscopy (SEM) was developed about a decade later in 1942, owing to the complexity of the machine's scanning process.

There is a variety of similarities between SEM [9] TEM [10]. Both are electron microscopes that give the possibility to examine with a high magnification and resolution the morphology and the compositions of a sample. They both use electrons (specifically, electron beams) to acquire images, but while in SEM the beams scan the surface of the sample, in TEM they are transmitted through the sample and this allows to look beyond the surface. In fact, the method used in SEM is based on scattered electrons (classified as backscattered or secondary electrons) while TEM is based on transmitted electrons.

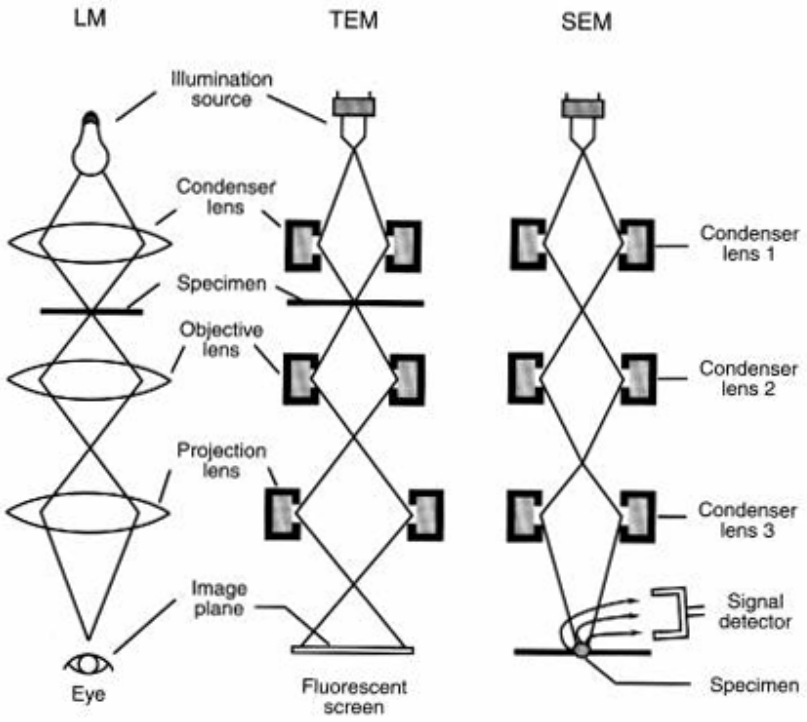

Fig. 3.8 - Comparison between schematic representation of the SEM, TEM and LM setup.

SEM and TEM have also some significant differences. In SEM, electrons are scattered as a consequence of interactions between the primary electron beam and the surface and this produces an image of the sample, which is collected by the microscope which also counts the scattered electrons. In TEM, electrons are directly pointed toward the sample and since the organization of the instrument is similar to that of the light microscope (LM), the electrons that pass through the sample create illuminated regions in the image (see Figure 3.8).

While in the SEM the scattered electrons from the samples (Fig. 3.9) are captured by the detector, in TEM the image is magnified and focused onto an imaging device, such as a fluorescent screen, on a layer of photographic film, or is detected by a sensor such as a CCD camera.

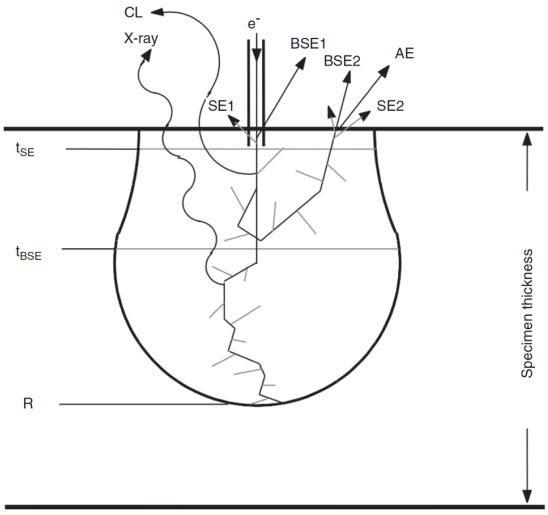

Fig. 3.9 - Illustration of several signals generated by the electron beam-specimen interaction in the scanning electron microscope and the regions known as the interaction volume (from 100nm to 1μm) from which the signals can be detected.

Even the focus of analysis is different. SEM focuses on the sample's surface and its composition and shows the sample bit by bit, providing a three-dimensional image. On the other hand, TEM seeks to see what is inside or beyond the surface and therefore shows the sample as a whole delivering a two-dimensional picture. In terms of magnification and resolution, TEM has an advantage compared to SEM. TEM has up to a 50 million magnification level, whereas SEM offers a maximum magnification level of only 2 millions. Moreover, the resolution of TEM is 0.5 angstroms, whereas SEM has a resolution of 0.4 nanometers; however, SEM images have a better depth of field compared to TEM produced images.

In Figure 3.10, is reported a comparison between a SEM and TEM images of a Mesoporous Carbon (MC) sample obtained from our synthesis.

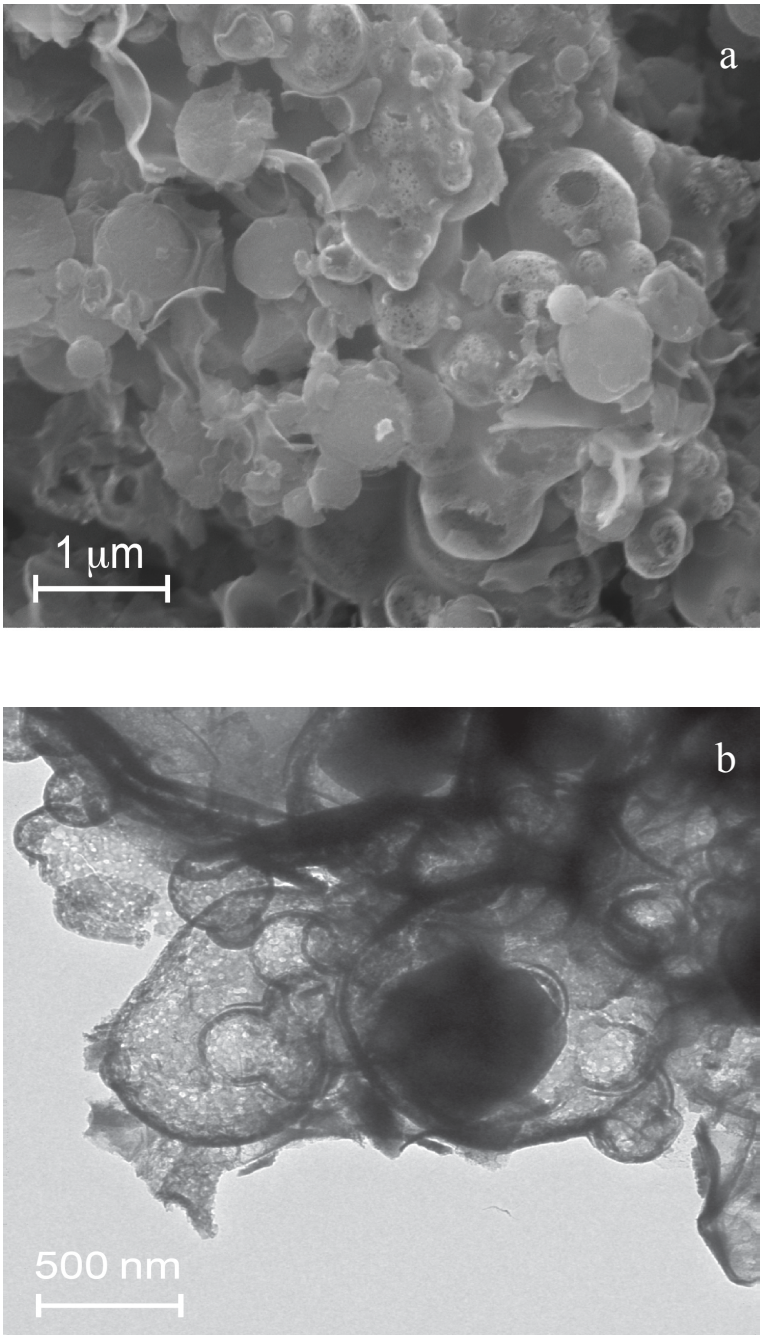

Fig. 3.10 - Comparison between (a) SEM and (b) TEM images of MC.

3.7 Brunauer-Emmett-Teller Theory

Stephen Brunauer, Paul Emmett and Edward Teller developed the BET theory in 1938 [11-15]. The first letter of each author's surname was taken to name this theory, which is an extension of the Langmuir theory, developed by Irving Langmuir in 1916.

The Langmuir theory is based on the following assumptions:

- All surface sites have the same adsorption energy for the adsorbate, which is usually argon, krypton or nitrogen gas. A surface site is defined as the area on the sample where one molecule can adsorb onto.
- Adsorption of the solvent at one site occurs independently of adsorption at neighboring sites.
- Activity of adsorbate is directly proportional to its concentration.
- Adsorbates form a monolayer.
- Each active site can be occupied only by one particle.

The BET theory extends the Langmuir theory to multilayer adsorption with three additional assumptions:

- Gas molecules will physically adsorb on a solid in multilayers.
- The different adsorption layers do not interact.
- The theory can be applied to each layer.

Adsorption is defined as the adhesion of atoms or molecules of gas to a surface. The amount of gas adsorbed depends on the exposed surface area but also on the temperature, gas pressure and strength of the interaction between the gas and the solid. In BET surface area analysis, nitrogen is usually used because of its availability in high purity and its strong interaction with most solids. Because the interaction between gaseous and solid phases is usually weak, the surface is cooled using liquid N_2 to obtain detectable amounts of adsorption. Known amounts of nitrogen gas are then released stepwise into the sample cell. Relative pressures less than 1 atm are achieved by creating conditions of partial vacuum. After the saturation pressure, no more adsorption occurs, regardless of any further increase in pressure. Highly precise and accurate

pressure transducers monitor the pressure changes due to the adsorption process. After the adsorption layers are formed, the sample is removed from the nitrogen atmosphere and heated to cause the adsorbed nitrogen to be released from the material and quantified. The data collected is displayed in the form of a BET isotherm, which plots the amount of gas adsorbed as a function of the relative pressure.

Five types of adsorption isotherms (denoted I-V) are possible, but our interest is mainly focused on type IV isotherm (Chapter 6 – Mesoporous Carbon), which is characterized by the formation of a monolayer, followed by the formation of multilayers in mesoporous materials that have pore diameters between 2-50 nm. (See Fig. 3.11)

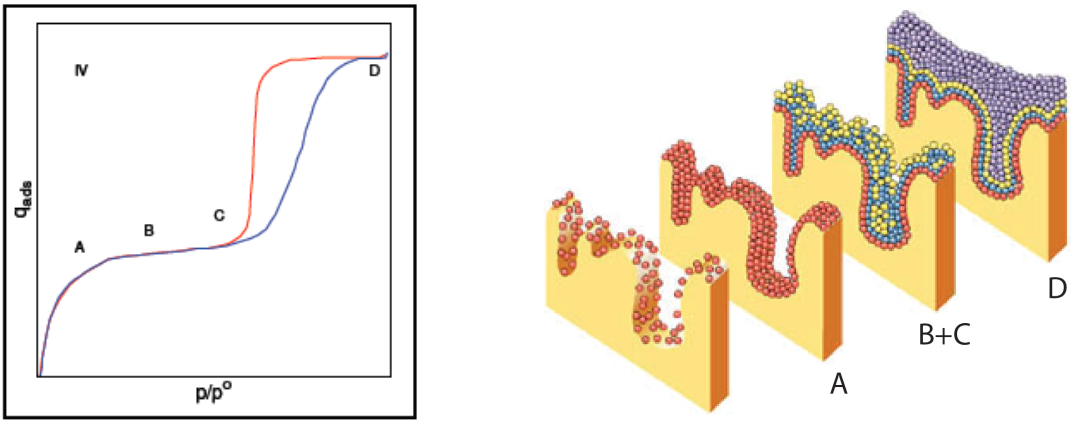

Fig. 3.11 - (a) Isotherm type IV, (b) model of monolayer and multilayer adsorption.

The BET equation (Eq. 3.15) uses information from the isotherm to determine the surface area of the sample:

$$S = \frac{X_m N_a A_m}{M_v} \qquad [3.15]$$

where X_m is monolayer capacity, which is the volume of gas adsorbed at standard temperature and pressure (STP), N_a is Avogadro's number, A_m is the cross-sectional area of the adsorbate and equals 0.162 nm^2 for an absorbed nitrogen molecule, and M_v is the molar volume of the gas (22414 mL at STP).

Bibliography

[1] Zoski, C.G. *Handbook of Electrochemistry*, Elsevier **2007**.

[2] Bard, A.J.; Faulkner, L.R. *Electrochemical Methods*, 2nd ed., John Wiley & Sons **2001**.

[3] Gennaro, A. *Electrochemistry of Materials,* lecture notes.

[4] Favaro, M.; Perini, L.; Agnoli, S.; Durante, C.; Granozzi, G.; Gennaro, A. *Electrochim Acta* **2013**, *88*, 477.

[5] Einstein, A. *Annalen der Physik* **1905**, *17*, 132.

[6] Rizzi, G.A. *X-ray Photoelectron Spectroscopy*, lecture notes.

[7] Fadley, C.S. *Electron Spectroscopy,* Pergamon Press **1978**.

[8] Güntherodt, H. J.; Wiesendanger, R. *Scanning Tunnelling Microscopy I,* Springer **1992**.

[9] Zhou, W.; Wang, Z.L. *Scanning Microscopy for Nanotecnology*, Springer **2006**.

[10] Williams, D.B.; Barry Carter, C. *The Transmission Electron Microscopy*, Springer **1996**.

[11] Sing, K. S. *Langmuir* **1987**, *3*, 2.

[12] Brunauer-Emmett-Teller (BET) Surface Area Analysis and Barrett-Joyner-Halenda (BJH) *Pore Size and Volume Analysis, Testing and Analysis Techniques*. CERAM.

[13] Brunauer, S.; Deming, L.S.; Deming, W.E.; Teller, E. *J. Am. Chem. Soc.* **1940**, *62*, 1723.

[14] Brunauer, S.; Emmett, P.H.; Teller, E. *J. Am. Chem. Soc.* **1938**, *60*, 309.

[15] Bae, Y.S.; Yazaydin, O.; Snurr, R.Q. *Langmuir* **2010**, *26*, 5475.

HIGHLY ORIENTED PYROLITIC GRAPHITE

4.1 Carbon based electrodes

Carbon (from: *carbo* "coal") is a chemical element with the symbol **C** and atomic number 6. As a member of group 14 of the periodic table, it is non-metallic and tetravalent - making four electrons available to form covalent chemical bonds.

The well-known allotropes of carbon include graphite, diamond and fullerenes, each of which can exist in a variety of materials with different electrochemical properties. The most common of these materials are based on the graphite structure where the carbon atoms are sp^2 hybridized with an intraplanar C-C bond length of 1.42 Å.

The often-cited advantages of carbon-based electrodes include low cost, wide potential window, relatively inert electrochemistry, predisposition to be chemically modified, and electrocatalytic activity for a variety of redox reactions [1].

As a catalyst support, carbon supported platinum is commonly used as anode and cathode electrocatalysts in low-temperature fuel cells, fuelled with hydrogen or low molecular weight alcohols, and in metal-air batteries [2,3]. In the last period, the chemical doping of sp^2-carbon materials with nitrogen has gained a lot of attention, since excellent stability and high performances over time of the NPs/support assembly have been obtained [4-6]. Even more interestingly, it has been suggested that a properly doped support can become itself catalytically active [7].

The most ordered three dimensional graphite materials are relatively uncommon and comprise highly oriented pyrolytic graphite (HOPG) and natural crystalline graphite. HOPG is made by high-temperature decomposition of gaseous hydrocarbons, often acetylene, followed by hot pressing at high pressure and temperature. The dimensions of the crystallites often characterize graphite materials, L_a for the in-plane crystallite size and L_c for the inter-planar space perpendicular to the graphene planes (Fig. 4.1).

In this chapter, we will see the physical and electrochemical properties of HOPG, pristine and doped, before and after deposition of palladium NPs, which is a model system to understand the catalytic activity and ORR mechanism in the field described above. We have chosen to use Pd, instead of Pt, because it has very similar properties (same group of the periodic table, same *fcc* crystal structure, similar atomic size), but is much cheaper than Pt and could therefore be a good substitute for Pt as a catalyst in fuel cells.

L_a: in-plane microcrystalline size,
L_c: inter-planar microcrystalline size

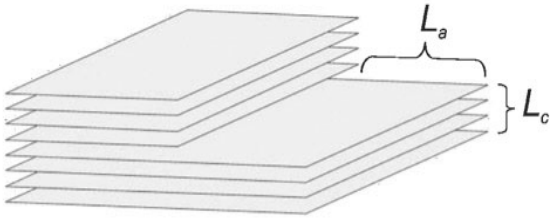

Fig. 4.1 - Structure model of HOPG.

4.2 Chemical and Electrochemical properties of HOPG

Highly Oriented Pyrolytic Graphite (HOPG) is the most suitable sp^2-carbon model substrate and is of particular interest because the electro-chemical behaviour of carbon nanotubes or graphene is commonly interpreted with reference to the graphite surface [8,9].

Actually, rigorous studies of model electrodes, in terms of surface characterization and electrochemical behaviour, for the rationalization of the effects deriving from the doping of the supports is still missing. Therefore, the outcomes of adopting HOPG as benchmark electrodes can be capitalized to implement efficient real electrodes based on the most innovative carbon based materials to be properly tested under working conditions. Recent studies have demonstrated the presence of distinct chemical defects [10,11] in N-doped HOPG (hereafter N-HOPG) obtained by N^+ and N_2^+ implantation [12,13]. Thence, the use of HOPG allows investigation of the role played by the chemical defects for promoting catalytic activity. This can be achieved by comparing HOPG with doped HOPG, keeping unchanged all the other factors (such as active surface area, conductivity and porosity of the support) that are involved in

determining the overall catalytic activity. However, many chemical aspects are still obscure and a systematic identification of all the functional groups that can be introduced into carbon-based materials has not been yet undertaken. In this study, we have used HOPG as a model system for mimicking sp^2-hybridized carbon-based supports and ion implantation as a doping technique. We choose this route because, being a kinetic driven technique, it allows obtaining a rich gamut of N-based defects. In order to disentangle the effects connected to the presence of new functional groups from those deriving from the morphological defects introduced by ion implantation, we studied also Ar^+ implanted HOPG samples (hereafter Ar-HOPG) and used them as an internal reference to gauge the results.

Another advantage of using HOPG is related to the impressive literature that deals with the electrochemical behaviour of pure and modified HOPG electrodes [1], allowing a sound comparison with the new electrode supports. Actually, the electrochemical properties of HOPG surfaces are under a renewed focus, in part driven by the on-going interest on the reactivity of carbon nanotubes and graphene. An aspect of particular interest refers to the different activity of edge planes and basal planes with respect to the heterogeneous electron transfer (ET) from/to HOPG. ET is reported to take place on the edges of graphite sheets, while ET from the basal planes of HOPG is very close to zero [14,15]. In particular, the edge planes are associated to the presence of chemical and morphological defects. Therefore, the electrochemical analysis allows disentanglement of effects coming from surface chemistry from those related to pure structural defects. In virtue of the high susceptibility of HOPG to ET processes, we have investigated several different electrochemical probes, namely $Ru(NH_3)_6^{3+}$, $Fe(CN)_6^{4-}$ and O_2. The $Ru(NH_3)_6^{3+}$ cation has been employed since its ET kinetics is not affected by neither chemical nor morphological defects [1]. The second redox probe considered is $Fe(CN)_6^{4-}$, which is reported to be sensitive to the state of the carbon surface [1] and, in particular, the sensitivity of its ET rate constant (k^0) on defects is unusually high. Thence, it is commonly used to validate HOPG surfaces [16]. It is well-documented that the reduction of O_2 at pristine HOPG has a slow kinetics [17], and that the main reduction pathway involves a two-electron process leading to the formation of hydrogen peroxide [18]. This is why HOPG is often adopted as a support for investigating the mediation effect of functional groups, such as quinones, which generally promote the

ET to O_2 by increasing the reduction rate [19]. Therefore, since O_2 reduction kinetics is affected by the surface chemistry and because there are many expectations concerning the use of doped carbon materials as cathode supports in fuel cells and batteries or in O_2 or H_2O_2 sensors, ORR has been investigated. After that, undoped and doped HOPG, with palladium nanoparticles (NPs) deposited, were also studied, because a strong NP/support interaction is beneficial to improve both the activity and durability of the electrocatalyst [4,5].

4.3 Doping of HOPG by ion implantation

Clean HOPG samples (MikroMash, ZYB grade) were prepared by peeling the surface with a scotch tape, and then by annealing in Ultra High Vacuum (UHV) at 800 °C. The UHV preparation chamber (base pressure < 5×10^{-9} mbar) was equipped with a double anode X-ray source (Omicron), a hemispherical electron analyzer (VG Scienta) and an ion gun (Thermo VG Scientific). The N- and Ar-HOPG samples were prepared by using the ion beam produced by the ion gun under the same conditions: 2.2×10^{-6} mbar background of N_2 or Ar, a beam energy of 500 eV and exposure time of 10 min, with an incidence angle of the ion beam equal to 45° with respect to the sample surface (the ion current measured during this treatment was 2.0 μA and the total dose of implanted atoms was around 3.8×10^{16} ion cm^{-2}). The nitrogen/argon dose was evaluated to be between 6.5 at% and 10 at%. All the XPS measurements were performed at room temperature (r.t.), using non-monochromatized Mg-Kα radiation ($h\nu$ = 1253.6 eV) and pass energy of 50 eV and 20 eV for the survey and high-resolution spectra, respectively. The calibration of the Binding Energy (BE) scale was carried out using Au 4f as reference. The XPS peaks were deconvoluted into individual components (after Shirley background removal) using symmetrical Voigt functions and nonlinear least squares routines for the χ^2 minimization. Thermal annealing cycles were performed with electron-beam heating; the temperature was measured by a K-type thermocouple. Scanning tunneling microscopy (STM) data were acquired in situ, in the RHK SPM1000 STM system connected to the preparation chamber and operating in

UHV conditions (base pressure about 5×10^{-11} mbar). The STM images were obtained in constant current mode at r.t., with tip-to-sample positive bias of 0.4 V and tunneling current close to 0.4 nA. The STM tips were prepared by chemical etching of a Pt/Ir 80:20 wire in a saturated $CaCl_2$ solution [20]. The analysis and the post-processing of the STM images were carried out employing the WSxM 4.0 software [21]. Monte Carlo simulations were carried out by using the SRIM-011 (Stopping and Range of Ion in Matter) package [22].

Table 4.1 - Projected range and FWHM (ΔR_p) of the ion distributions in implanted HOPG calculated with the SRIM-011 package assuming the Kinchin-Pease modeling [19] of the ion-target atoms interaction.

	R_p [Å]	ΔR_p [Å]
Ar^+	13.08	9.42
N_2^+	17.19	15.46
N^+	20.04	19.22

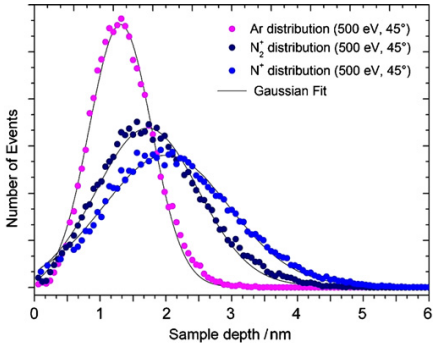

Fig. 4.2 - Ion distributions in implanted HOPG calculated with the SRIM-011 package [17] assuming the Kinchin–Pease modeling [19] of the ion–target atoms interaction (the simulation has been performed with a beam constituted by 10^6 ions).

Under the experimental conditions described above, the nitrogen plasma contains both N^+ and N_2^+ ionic species. Fig. 4.2 reports the N^+, N_2^+ and Ar^+ ion distributions in the HOPG target, while the parameters that characterize them (i.e. the projected range, R_p, and the Full Width at Half Maximum, FWHM, of the distribution, ΔR_p) are reported in Table 4.1.

The ion implantation process can be interpreted by assuming the so-called three steps model [21].

1. The interaction of the ion beam with the first layer of the target does not change significantly the energy of the ion beam itself if the energy (e.g. 500 eV in our experiments) is much higher than the displacement energy $\Delta E_{Frenkel}$ necessary to

produce a Frenkel couple ($\Delta E_{Frenkel}$ = 47.3 eV for graphite [25]). Then, the energy loss of the ions due to the interaction with the first layers of the target is negligible. As a direct consequence of the high kinetic energy, an amorphous region (localized within the first few layers of the target) is expected, and actually observed by STM (see Fig. 4.2), in agreement with previous literature data [26].

2. During ion penetration and propagation into the target, thermal spikes can occur along the ion trajectories due to the energy exchanged between ions and target. The consequent high-energy collision cascades can be at the origin of non-equilibrium or non-thermodynamic defects (due to the high local temperature generated in these thermal spikes, the reactions taking place within this scenario, are obviously under kinetic control).

3. Finally, for spatial regions close to the R_p, the ions are considered in thermal equilibrium with the target and the chemical reactions are under thermodynamic control. In this way, equilibrium or thermodynamic defects are generally localized close to the R_p.

If we examine the STM data reported in Fig. 4.3 for both the N-and Ar-HOPG samples, we clearly observe amorphization of the surface after the interaction with the ion beam without significant differences in morphology between the two samples. Moreover, it is possible to notice that, as a consequence of thermal treatment at 500 °C, a slight smoothing of the surface roughness takes place as confirmed by the decrease of Root Mean Square roughness (RMS) observed on thermally annealed, modified HOPG surfaces (see values reported in Table 4.2, where the error that affects these roughness RMS values is about 5% of the values themselves.).

Table 4.2 - Roughness RMS values for N- and Ar-HOPG samples obtained by the STM measurements reported in Figure 4.2 before and after a thermal annealing at 500 °C.

	RMS values (nm)	
	r.t.	annealed at 500 °C
Ar-HOPG	0.38 ± 0.02	0.34 ± 0.02
N-HOPG	0.39 ± 0.02	0.36 ± 0.02

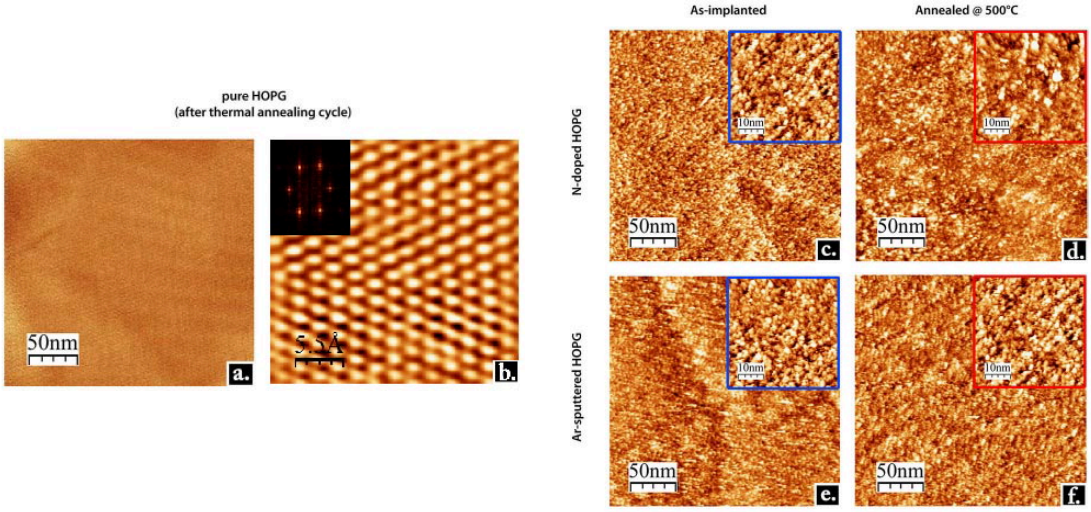

Fig. 4.3 - STM images (250 nm × 250 nm) obtained on: (a) and (b) the pristine HOPG, (c) and (d) N-HOPG and (e) and (f) Ar-HOPG samples. The inset in (b) reports the Fourier spatial transform, while the insets in (c)–(f) show a zoomed image (50 nm × 50 nm).

Thence, any possible difference between the two differently modified HOPG surfaces obtained in our experimental conditions derives from chemical rather than from morphological changes. In order to characterize the chemical modifications induced by the ion implantation, we have carried out a thorough XPS investigation. In the large range measurements (surveys, Fig. 4.4), only two peaks are observed in the case of N-HOPG, i.e. C 1s (284.4 eV) and N 1s (400.0 eV).

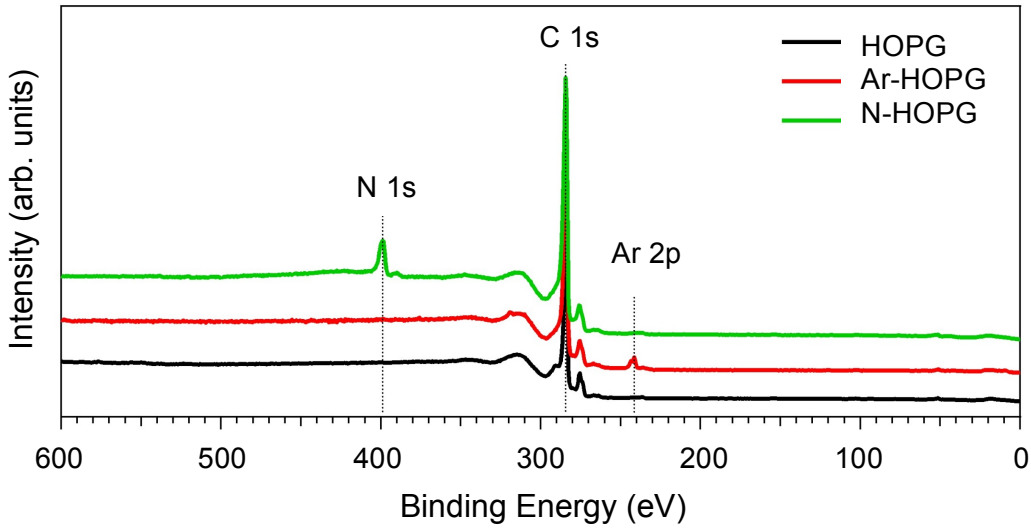

Fig. 4.4 - Wide scan XPS surveys on HOPG, Ar-HOPG and N-HOPG.

On the other hand in Ar-HOPG it is possible to identify the Ar 2p (241.5 eV, corresponding to Ar atoms trapped on HOPG disordered structures [27] or between two graphene layers [27]), and C 1s (284.4 eV). The presence of the low intensity O 1s features is imputable to some C-O groups present at the step edges. In order to get a more precise description about the chemical identity of the defects, the C 1s and N 1s energy regions (Figs. 4.5 and 4.6) have been separately recorded and the corresponding peaks have been fitted to Voigt functions, imposing FWHM in the 1.0 - 1.4 eV range. Fig. 4.5 reports the multi-peak analysis of the C 1s signals for the N- and Ar-HOPG samples. For the latter, two components are visible, one centered at 284.4 eV, which can be attributed to sp^2 hybridized carbon (Csp^2) forming the pure graphitic lattice, and one at 285.5 eV, connected to sp^3 hybridized carbon (Csp^3), constituting tetragonally coordinated carbon clusters [28,29]. On the contrary, the C 1s signal relative to the N-HOPG, shows three resolved components at 284.4, 285.5 and 286.5 eV, which, according to literature, can be assigned to Csp^2 [28], Csp^3 [29], and C-N bonds [28,30], respectively.

From these data, we can deduce that Ar-implantation determines relevant morphological defects consisting in a re-hybridization of carbon atoms from Csp^2 to Csp^3 structures (about 30%, judging from the intensity ratio of the two photoemission signals). On the other hand, N-implantation can induce also chemical defects (the C-N signal accounts for 13% of the total C 1s photoemission line) whose characterization has been carried out by analysing the N 1s XPS signals, as reported in Fig. 4.6. Five different components have been identified, showing FWHM and BE values that are perfectly in agreement with literature data on related systems. The XPS peaks centered at 398.1, 400.2 and 401.2 eV correspond to Csp^2-N defects (see the model in Fig. 4.6), which can be described as pyridinic [28,31,32], pyrrolic [30,31] and graphitic N defects [30–32], respectively. The component centered at 398.9 eV matches with C-N terminal groups [11,32]. Finally, the component centered at 402.7 eV can be attributed to an N^+ ion trapped into a carbon vacancy [11].

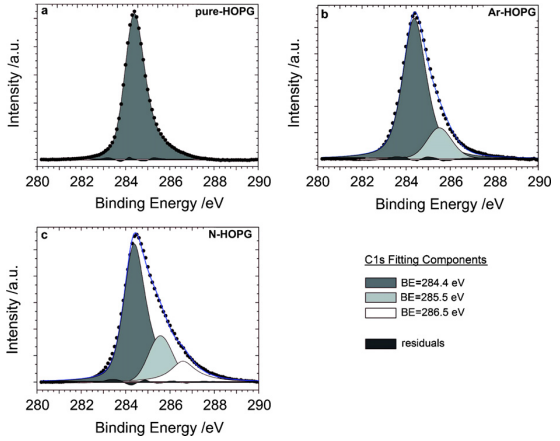

Fig. 4.5 - C 1s XPS regions (take off angle: 30°) of: (a) pure HOPG (after peeling and thermal annealing in UHV); (b) Ar-HOPG; (c) N-HOPG.

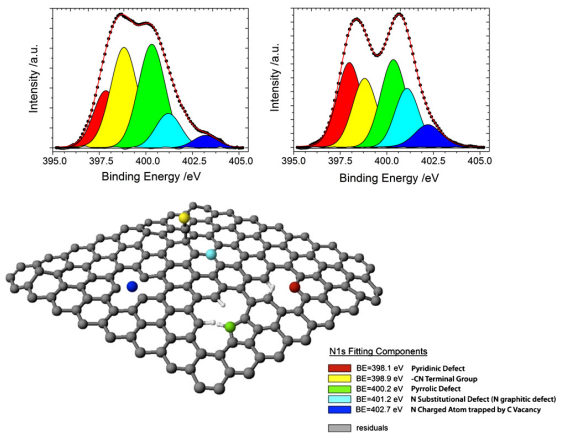

Fig. 4.6 - Multi-peak analysis of the N 1s photoemission line in the N-HOPG sample (left: as-implanted, right: annealed at 500 ◦C) and ball-and-stick model of the corresponding defects.

In order to observe the temperature evolution of these defects, N 1s photoemission measurements at different annealing temperatures have been carried out. Fig. 4.7b reports the percentage of the area for each chemically shifted peak, together with the total dose of implanted nitrogen, which shows a decrease from 10% to 7.5% on passing from r.t. to 500 °C. The most striking feature is the relevant removal of CN groups as the annealing temperature increases (see also the change in the shape of the N 1s signal obtained after annealing at 500 °C, reported in Fig. 4.7a, due to the decrease of the CN related peak). This phenomenology is in agreement with previous works [10,33], which report some thermal programmed desorption measurements indicating the desorption of CN species starting from 140 °C. Another important consequence of the thermal annealing is the increase of the intensity of the graphitic N atoms above 250 °C. This phenomenon has been observed also in the case of the thermal treatment of N-doped graphene layers obtained by chemical vapour deposition [33], and seems to indicate a greater thermodynamic stability of these defects as can be easily inferred considering that in this case the N atoms can exploit the highest coordination with other C atoms.

As a general comment, we wish to point out that, with the exception of the as-implanted samples, at any other temperature, pyridinic and, to a lesser extent, pyrrolic defects are the predominant surface species, demonstrating a quite good thermal stability. This is quite interesting for applications since it has been postulated that these functional groups play an important role in ORR [4,34,35].

Moreover, also in the case of advanced electrocatalysts obtained by the combination of polyaniline with Fe and Co, pyridinic and pyrrolic centers are responsible for the enhanced catalytic activity [36]. All these results consistently delineate a picture where HOPG modified surfaces can be used as a model system for investigating the impact of different C-N functional groups on specific electrochemical processes.

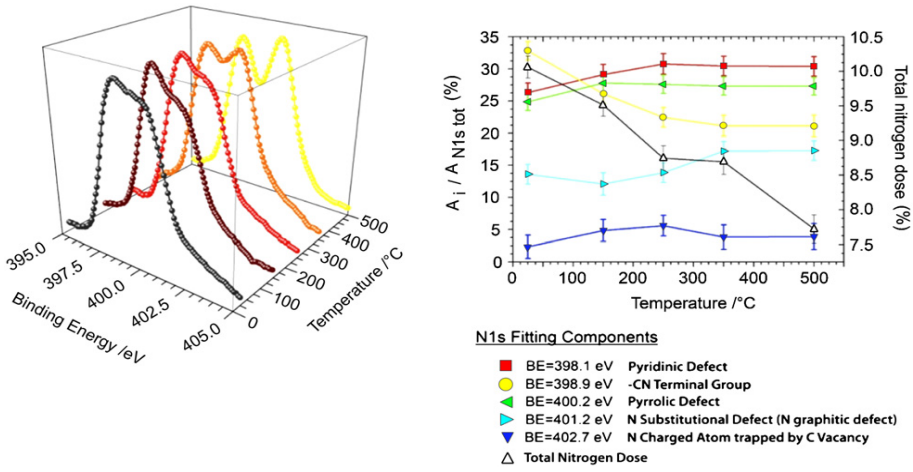

Fig. 4.7 - (a) N 1s XPS peaks for different annealing temperatures. (b) Temperature trend of the single components for N 1s XPS peaks (30◦ take off angle). The error bar has been provided by the fitting procedure of the photoemission peaks.

4.4 Electrochemical characterization

The electrochemical characterization of freshly cleaved HOPG, Ar-HOPG and N-HOPG samples was carried out by CV and EIS in a 0.1 M K_2SO_4 solution. Background CVs show a wide accessible potential window for pristine HOPG (3.0 V),

as well as for both Ar-HOPG (2.9 V) and N-HOPG (3.2 V) (Fig. 4.8), which is a highly desirable feature for electrode supports to be employed in catalysis. Both Ar and N implantation seems to produce a higher overvoltage for hydrogen evolution, while oxygen evolution shows similar characteristics at N-HOPG and pristine HOPG electrodes, but a lower overvoltage at Ar-HOPG.

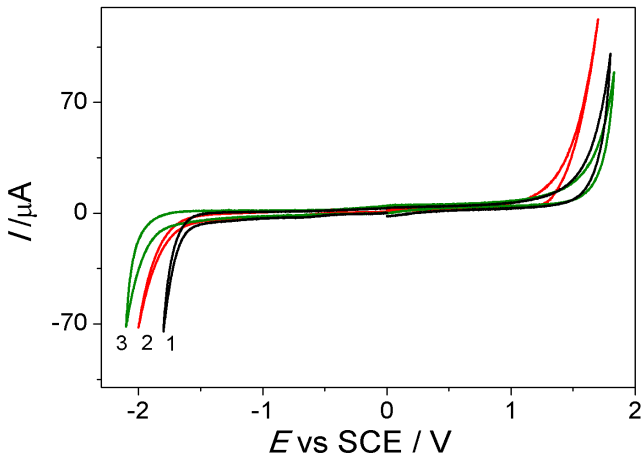

Fig. 4.8 - Background CVs of HOPG (1), Ar-HOPG (2), N-HOPG (3) recorded at 0.2 V s^{-1} in 0.1 M K_2SO_4.

The most accepted explanation for the diverging activity of step edges and basal planes toward ET processes is based on the semiconductor character of HOPG basal plane [37]. In particular, the local electric field may be much higher at "edge planes" (i.e. region of localized step bunching) [38] than on basal planes and this may lead to very different double-layer effects. Other studies correlate the higher electrochemical activity of the edge plane with an increased Density of electronic States (DOS) near the edges and thus, a higher DOS in the electrode increases the probability that an electron with suitable energy is available for electron transfer to a redox system. For this reason, disordered graphite behaves electronically like a metal with a low DOS, while HOPG by itself behaves like a semiconductor. Furthermore, step edges are decorated with several types of functional groups, usually oxygen functional groups, that may interact with the redox probe and therefore may enhance or restrain the electrode kinetics. The first redox probe considered was $Ru(NH_3)_6^{3+/2+}$, which is commonly used to represent an outer-sphere electron transfer reaction without specific chemical interactions with the surface. Voltammetric reduction of $Ru(NH_3)_6^{3+}$ follows a nernstian behaviour at both

pristine and implanted HOPG electrodes, although at the three different electrode surfaces the reduction process involves different peak current densities (Fig. 4.9a). Analysis of the effect of scan rate on current intensity for $Ru(NH_3)_6^{3+}$ reduction, results in a linear I_p vs. $v^{1/2}$ relationship all over the investigated scan rate range (0.02–5 V s^{-1}) for both implanted and pristine HOPG electrodes, indicating that the current is controlled by a semi-infinite linear diffusion. The ΔE_p value, increases with the scan rate pointing to a quasi-reversible ET process, with a standard heterogeneous rate constant k^0, which can be calculated by using the Nicholson method [39]. The k^0 values measured for the three electrode surfaces are listed in Table 4.3; N-HOPG (7.4×10^{-2} cm s^{-1}) and pristine HOPG (5.9×10^{-2} cm s^{-1}) show similar k^0 values, whereas ET at Ar-HOPG is 2-3 times faster. Due to the susceptibility of the Nicholson method to uncompensated ohmic drop, k^0 was also determined by EIS experiments and the extrapolated k^0 values are reported in Table 4.3. These values are slightly different from those calculated by the Nicholson method.

Table 4.3 - Charge transfer process parameters determined from the CV and EIS data.

		CV		EIS [a]	
		ΔE_p (V)	k^0 (cm s^{-1})	R_{ct} (Ω) [b]	k^0 (cm s^{-1})
$Ru(NH_3)_6^{3+/2+}$ [c]	HOPG	0.074	$5.9 \cdot 10^{-2}$	$2.39 \cdot 10^{2}$	$3.54 \cdot 10^{-2}$
	N-HOPG	0.071	$7.4 \cdot 10^{-2}$	$1.73 \cdot 10^{2}$	$4.90 \cdot 10^{-2}$
	Ar-HOPG	0.062	$1.7 \cdot 10^{-1}$	$3.69 \cdot 10^{1}$	$3.18 \cdot 10^{-1}$
$Fe(CN)_6^{3-/4-}$ [c]	HOPG	1.18	--	$5.70 \cdot 10^{5}$	$1.48 \cdot 10^{-5}$
	N-HOPG	0.24	--	$3.82 \cdot 10^{3}$	$2.21 \cdot 10^{-3}$
	Ar-HOPG	0.20	--	$2.76 \cdot 10^{3}$	$3.07 \cdot 10^{-3}$

[a] Recorded at the formal standard potential $Fe(CN)_6^{3-/4-}$ (E^0 = 0.189 ± 0.005 V *vs.* SCE), $Ru(NH_3)_6^{3+/2+}$ (E^0 = –0.236 ± 0.005 V vs. SCE).
[b] Data obtained from non-linear least square fits of the corresponding Nyquist plots.
[c] The overall concentration of the oxidized and reduced specie was 1 mM.

The values of k^0 found on pristine and doped HOPG point out that the $Ru(NH_3)_6^{3+/2+}$ redox process is only weakly affected by the presence of nitrogen and morphological defects on the electrode surface.

The second redox probe considered was $Fe(CN)_6^{3-/4-}$, which, however, represents a somewhat problematic probe for HOPG in virtue of controversial results reported in the literature. Compton et al. have proposed that k^0 for ferrocyanide oxidation at basal plane HOPG is lower than 10^{-9} cm s^{-1}, possibly even zero [40,41]. On the other hand, Williams et al. have demonstrated, by means of a scanning micropipet contact method, that on HOPG basal planes the electroactivity is by far greater than previously reported [42]. McCreery has reported that at ungraded HOPG, which presents the lowest number of defects, the redox couple $Fe(CN)_6^{3-/4-}$ commonly gives a peak-to-peak separation ranging between 0.7 and 1.5 V, mostly depending on the procedure adopted for the surface preparation and the way the sample is handled [43]. Peak-to-peak separations of more than 0.7 V are indicative of a very slow ET kinetics [44–46]. The oxidation of $Fe(CN)_6^{4-}$ at ZYB grade HOPG in 0.1 M K_2SO_4 gives a peak-to-peak separation >0.9 V (Fig. 4.9b). For such a slow electron transfer process, it is not possible to employ the Nicholson method to determine k^0, since ΔE_p is out of the validity range of the method. Therefore, k^0 values at freshly cleaved HOPG, Ar-HOPG and N-HOPG electrodes has been extracted from EIS Nyquist plots (Fig. 4.10a). The standard rate constant calculated for $Fe(CN)_6^{4-}$ oxidation at HOPG was $k^0 = 1.48 \times 10^{-5}$ cm s^{-1}. Since HOPG is expected to present a high number of surface defects, according to the literature, we should observe peak-to-peak separations in the order of 0.15–0.20 V, corresponding to k^0 values in the order of 3–5 $\times$ 10^{-3} cm s^{-1}, depending on the type of HOPG and the procedure adopted for its preparation. The discrepancy between our experimental results and literature data could be ascribed to the different experimental conditions, since we have experimentally verified that there is a deep influence of the type of supporting electrolyte and of its concentration on both ΔE_p and k^0, i.e. higher electrolyte concentration corresponds to lower ΔE_p and faster kinetics. A remarkable increase of the ET kinetics was observed at Ar-HOPG electrodes as evidenced by the shape of voltammogram 2 in Fig. 4.9b and by the decrease in the radius of the hemicycle in the Nyquist plot of Fig. 4.10b. The peak-to-peak separation decreased to 0.2 V and the overall faradic current was even higher than at the pristine HOPG electrodes. This behaviour indicates that k^0 is higher on the Ar-HOPG than on freshly cleaved HOPG surface. From Nyquist plot deconvolution we estimated a k^0 value of 3.07×10^{-3} cm s^{-1}, which is two orders of magnitude higher than on pristine HOPG (Table 4.3). Similar

results have been observed for N-HOPG: in this case, the peak-to-peak separation is 0.22 V at 0.2 V s^{-1} and the Nyquist plot (Fig. 4.10c) gives $k^0 = 2.21 \times 10^{-3}$ cm s^{-1}, which is comparable with the value observed at Ar-HOPG.

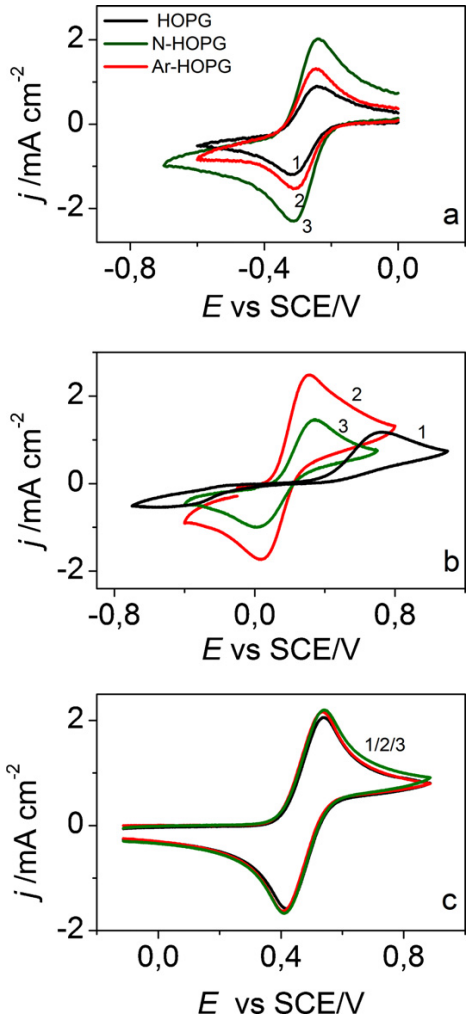

Fig. 4.9 - CVs of HOPG (1), Ar-HOPG (2) and N-HOPG (3) recorded at a scan rate of 0.2 V s^{-1} with (a) 2 mM $Ru(NH3)_6^{3+}$ in a 0.1 M K_2SO_4; (b) 2 mM $[Fe(CN)_6]^{4-}$ in a 0.1 M K_2SO_4; (c) 2 mM ferrocene in a 0.1 M Et_4NBF_4 in CH_3CN.

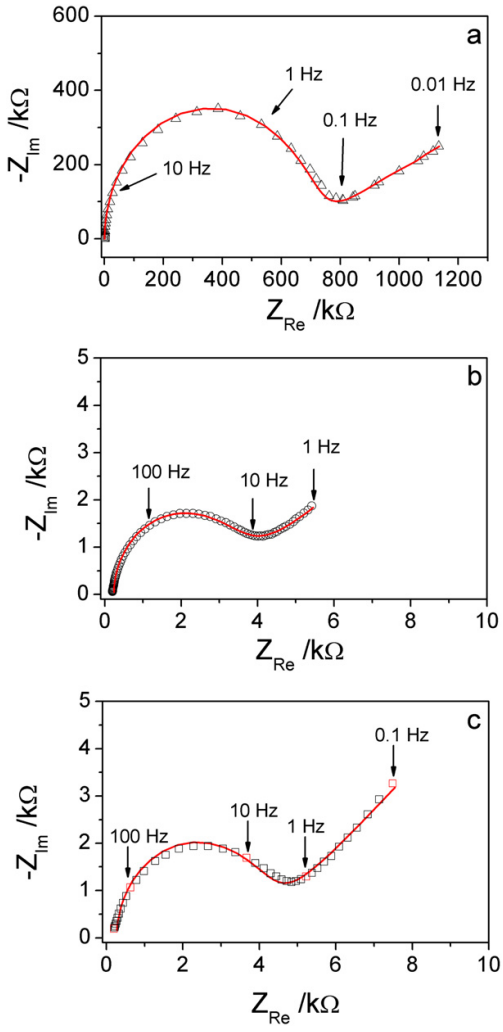

Fig. 4.10 - EIS Nyquist plot of 1 mM $[Fe(CN)_6]^{3-/4-}$ for (a) HOPG, (b) Ar-HOPG and (c) N-HOPG. The EIS spectra were recorded at the standard potential $E^0 = 0.189$ V vs. SCE in a 0.1 M K_2SO_4.

These results clearly indicate activation of the HOPG surface upon Ar- or N-implantation. In particular, it is well established in the literature that k^0 of the $Fe(CN)_6^{3-/4-}$ redox couple is sensitive to the physical, chemical and mechanical pre-

treatment of the electrode surface because of the introduction of novel chemical and morphological defects. In particular, laser ablation [43], electrochemical oxidation [47], and UHV thermal treatment, have shown to increase the ET kinetics.

Raman spectroscopy investigations have pointed out that all these surface activation procedures lead to the formation of a disorder band (D-band) at 1360 cm^{-1}, indicating a decrease of the size of graphite microcrystallites of HOPG, and that the D-band intensity correlates with the density of the graphitic edge planes [47]. Furthermore, it was demonstrated that the intensity of the D-band, and therefore the density of step edges, correlates with the heterogeneous electron transfer rate k^0. In the present case, Raman spectroscopy investigation has shown that both Ar and N sputtering result in the formation of a D-band at 1343 cm^{-1}, indicating an increased density of the graphitic edge planes (Fig. 4.11). It is worth noting that the D-band at 1343 cm^{-1} gets more intense upon increasing of the N or Ar dose up to a limiting implantation dose of 2×10^{15} ions/cm^2 (spectra b-d in Fig. 4.11).

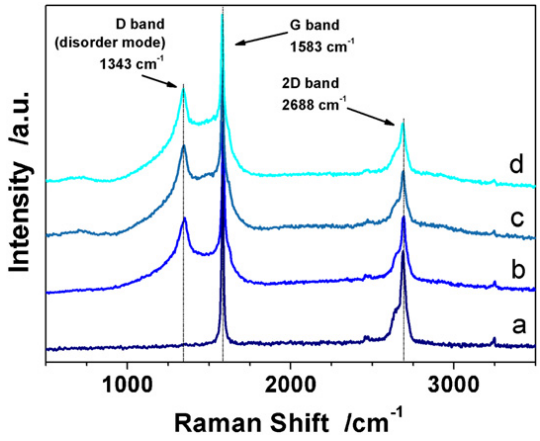

Fig. 4.11 - Raman spectra of HOPG at different doses of nitrogen N-implantation: N dose (ions/cm^2) = (a) 0, (b) 3×10^{14}, (c) 2×10^{15}, d) 5×10^{15}.

The electrochemically investigated samples were prepared with an implantation dose of 5×10^{15} ions/cm^2 (Fig. 4.11 spectra d), which is far beyond the saturation value and therefore the samples had the maximum achievable degree of amorphization. Consequently, the enhanced ET kinetics observed at Ar-HOPG and N-HOPG is to be attributed to the introduction of novel defects and to a higher density of step edges on

the electrode surface. As shown by the STM images reported in Fig. 4.3, Ar-HOPG and N-HOPG have similar surface morphology with an increased number of defects. The presence of defects should also increase the formation of oxygen functional groups, especially when, in the electrochemical cell, the HOPG electrode is exposed to the electrolyte and polarized. There are reports in literature claiming that functional groups on the electrode surface do not affect the ET kinetics for the $Fe(CN)_6^{3-/4-}$ redox couple [1]. In the case of N-HOPG, it is reasonable to assume that also nitrogen groups are placed near the edges of HOPG (see XPS data) and therefore, if a chemical interaction with the redox probe takes place, it should influence the electrode kinetics. However, only a slight difference between N-HOPG and Ar-HOPG has been observed. Therefore, we can deduce that, just like oxygen functional groups, nitrogen functional groups do not sensibly affect k^0 of this redox process. Both redox probes investigated do not discern between Ar-HOPG and N-HOPG, though it must be highlighted that there is a relevant difference in the peak current concerning the two differently implanted HOPG samples in the $Ru(NH3)_6^{3+/2+}$ redox process (Fig. 4.9a). N-HOPG electrodes exhibit a redox peak with a peak current density of about 2.3×10^{-3} A cm^{-2} at $\upsilon = 0.2$ V s^{-1}, in contrast to Ar-HOPG and HOPG, which show peak current densities of 1.5×10^{-3} A cm^{-2} and 1.2×10^{-3} A cm^{-2}, respectively. The increase of the peak current may be associated to an increase of the real surface area as a consequence of increased roughness. However, since STM results show that Ar-HOPG and N-HOPG samples have similar surface roughness, this reasoning seems to hold only for Ar-HOPG, where the increase of the current density is of the order of 25%. Besides increased surface roughness, a reasonable explanation for the increased magnitude of the current density at N-HOPG can be given by considering the presence of a higher density of negative charges on the HOPG surface, resulting from nitrogen implantation as confirmed by literature data [48,49]. The extent of negative charges present on the N-HOPG surface is evident when we performed CV on implanted HOPG using the negatively charged $[Fe(CN)_6]^{4-}$ (Fig. 4.9b). In this case, N-HOPG electrode exhibits a peak current density of 7.2×10^{-4} A cm^{-2} at a scan rate of 0.2 V s^{-1}, whereas Ar-HOPG shows a peak current density of 1.2×10^{-3} A cm^{-2}. The presence of a higher number of negative charges on N-HOPG surface, is likely to cause repulsion of the negatively charged $[Fe(CN)_6]^{4-}$ ions, thereby resulting in a smaller peak current density at N-HOPG as compared to Ar-

HOPG. Furthermore, the electrostatic repulsion may also be responsible for the small difference of k^0 value between the two differently implanted substrates and indirectly also in the shape of the CV peak. This interpretation is confirmed by measurements carried out on the neutral ferrocene species in an organic solvent (CH_3CN/tetrabutylammonium tetrafluoroborate 0.1 M) (Fig. 4.9c). In fact, although different double layer effects may arise in the organic environment with respect to the aqueous one, we have observed that oxidation of the uncharged species results in comparable peak current densities and k^0 values at both implanted surfaces. As a partial conclusion we may assert that morphological defects are the dominant factors ruling the electrode kinetics of $Ru(NH_3)_6^{3+}$ and $[Fe(CN)_6]^{4-}$ and therefore it is not possible at this stage to clearly distinguish eventual chemical effect effects between Ar- and N-implanted HOPG surfaces.

4.5 Deposition of Palladium NPs

Palladium NPs were prepared by deposition under Ultra High Vacuum (UHV) on either clean HOPG or N-HOPG, obtained by ion implantation as described in section 4.3. In this case, however, the time of exposure was reduced from 10 to 2.5 min and the nitrogen dose was evaluated to be about 3% as determined by XPS measurements. The implantation dose was reduced in order to have a minor roughness of the sample and thus have a better STM characterization of Pd NPs.

The deposition of Pd (i.e. 0.7 ML, 1.4 ML and 3.0 ML; ML = Mono Layer) was performed by in situ evaporation from a high-purity metal rod, at r.t., at a deposition rate of 0.25 ML min^{-1}, and calibrating one ML from the XPS measurements.

Fig. 4.12 summarizes the STM results obtained at r.t. for Pd(x ML)/HOPG (x = 1.4 and 3.0 ML), whereas no STM characterization was carried out for Pd(0.7 ML)/HOPG and /N-HOPG because the NPs were too small to be evaluated by this technique. In Fig. 4.12 a and d we report a flat and stepped region (x = 1.4 ML), respectively. In both cases, the lateral size (denoted as d) and the apparent height (denoted as h) of the Pd NPs are characterized by a bimodal distribution (see Fig. 4.12 b, c, e and f). In the flat zones, the Pd NPs ($d_1 = 3.35 \pm 1.30$ nm, $h_1 = 0.25$ nm and $d_2 =$

10.72 ± 2.11 nm, h_2 = 1.84 nm) present two almost equivalently populated maxima in the corresponding histograms (Fig. 4.12 b and c).

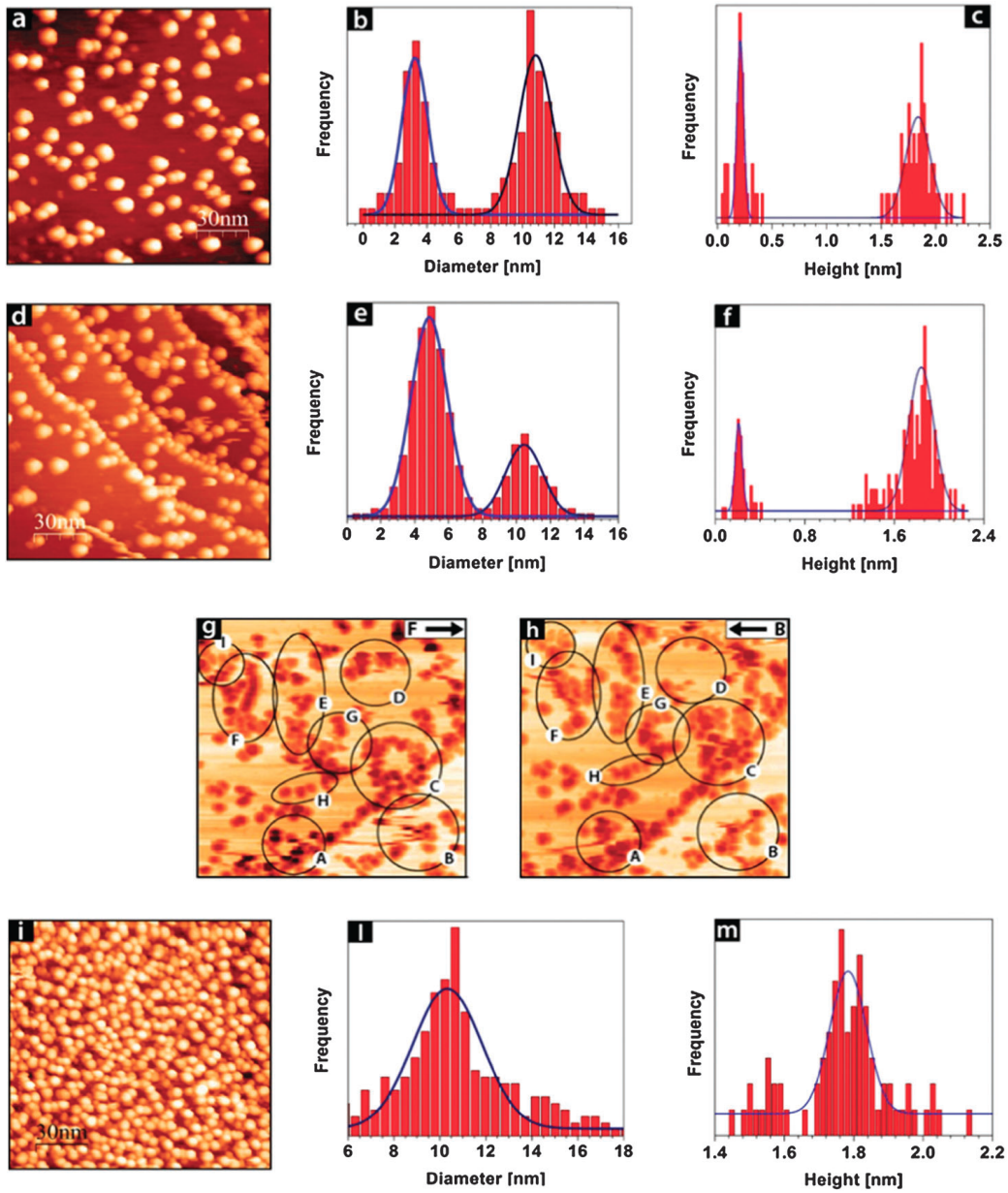

Fig. 4.12 - STM images (150 × 150 nm) (a) and (d) of the Pd(1.4 ML)/HOPG assembly and relative NPs size distributions (b and c) and (e and f), respectively. A forward and backward scan is reported in (g) and (h), respectively. In this case, in order to highlight the motion of the NPs, the *z*-scale is reversed. In (i), (l) and (m) the STM image and the relative size analysis of the Pd(3.0 ML)/HOPG system are reported.

On the other hand, when considering the step edge regions (Fig. 4.12d), the low-coordination sites can bind efficiently the Pd NPs, having an almost equivalent size (d_3 = 4.96 ± 2.08 nm, h_3 = 0.31 nm and d_4 = 10.65 ± 2.08 nm, which is obviously equal, within the error bar, to d2, and h4 = 1.82 nm) but with a higher population with the smallest ones. Moreover, Fig. 4.12g and h show that the NPs deposited onto pure HOPG are characterized by a pronounced mobility on the surface. This is in line with the usual phenomenology of metals nucleation and growth on HOPG at r.t.: typically, very mobile and unevenly distributed 3D islands with a wide size distribution are formed, with a strong tendency to nucleate on step edges, rather than on terraces [50]. Fig. 4.12i shows the STM measurements for Pd(3.0 ML)/HOPG: the Pd NP surface density is strongly increased with respect to the lower coverage, while the sizes are almost unchanged, i.e. d = 10.33 ± 2.97 nm and h = 1.80 nm, with the loss of the bimodal pattern (Fig. 4.12 l and m). The STM results on Pd(x ML)/N-HOPG (x = 1.4 and 3.0) are rather different (see Fig. 4.13): there is an increase in the density of the Pd NPs and, at the same time, a relevant decrease in their average size and apparent height. In particular, the Pd(1.4 ML)/N-HOPG system presents Pd NPs characterized by d = 1.61 ± 0.85 nm and h = 0.11 nm (Fig. 4.13b and c), whereas Pd(3.0ML)/N-HOPG shows d = 1.82 ± 0.96 nm and h = 0.44 nm, respectively (Fig. 4.13e and f). In addition, in the N-HOPG samples, the presence of low coordination sites formed even on the pristine terraces by the implantation process reduces the mobility and determines an extended nucleation; this phenomenology is evident making the comparison between Fig. 4.12 and 4.13.

In order to have a better understanding of the interaction of Pd NPs with HOPG, both *as prepared* and *doped* surfaces, XPS measurements were carried out. Fig. 4.14 reports the Pd 3d photoemission spectra corresponding to Pd(x ML)/HOPG (Fig. 4.14a) and Pd(x ML)/N-HOPG (Fig. 4.14b) assemblies (x = 0.7, 1.4 and 3). In the latter case, both as-implanted and annealed (at 500 °C for 30 min) supports (blue and cyan lines respectively, Fig. 4.14b) were examined.

In contrast to pure HOPG, on implanted substrates the centroid of the XPS Pd 3d peak shifts from higher to lower BE as a function of the metal dose, this phenomenon being particularly relevant when passing from 0.7 to 1.4 ML. This trend of Pd 3d peak BEs and FWHMs can be rationalized by the well-known Small Cluster Size Effect

(SCSE) [51–54]. Actually, it has been reported that Pd NPs of mean diameter >5 nm show a BE close to the bulk metal value (i.e. ΔBE = 0), while a marked decrease is observed for smaller NPs (diameter < 3 nm) and eventually, NPs of 1 nm present a shift as large as 1 eV [51,52]. The values reported above for the Pd/N-HOPG samples nicely fit this scenario considering the NPs sizes determined by STM.

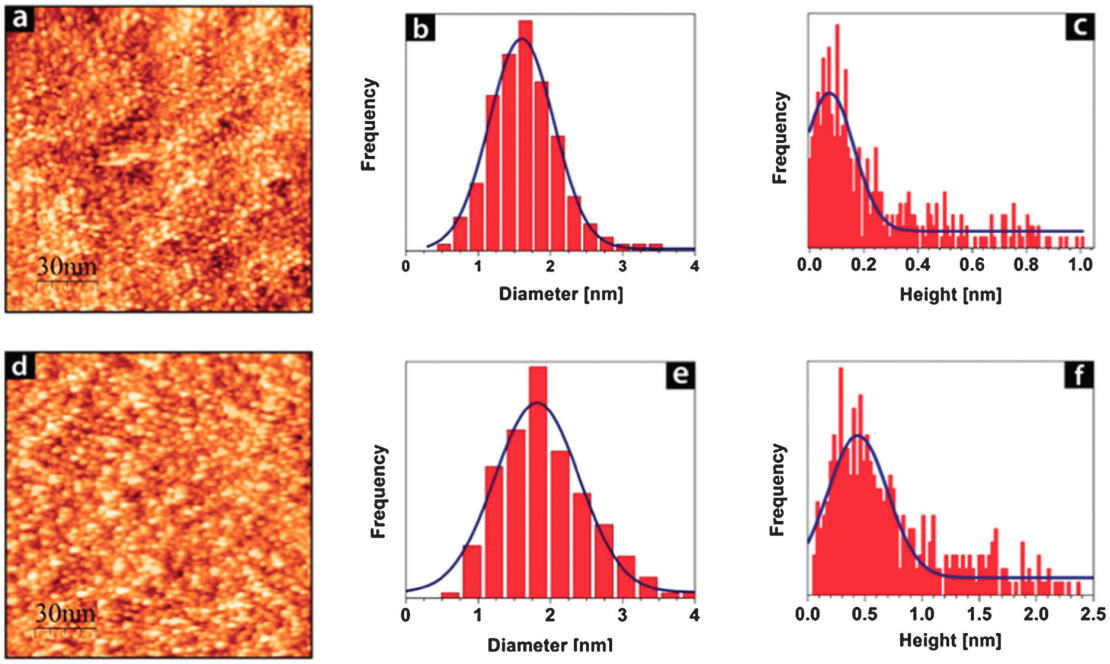

Fig. 4.13 - STM images (150 × 150 nm) (a) and (d) of the Pd(x ML)/N-HOPG assemblies (x = 1.4 and 3.0, respectively) and relative NPs size distributions. a and b: 150 × 150 nm scan area of 1.4 and 3.0 ML of palladium deposited onto N-HOPG, respectively. b, c, e and f show the size analysis for the two different palladium coverages.

The difference in the N 1s photoemission spectrum between the as-implanted and annealed data of N-HOPG was also evaluated (Fig. 4.15b) and was interpreted as deriving from the thermal desorption of cyano groups [55]. The analysis of N 1s spectra (Fig. 4.15b and d) indicates that there is no evident chemical interaction between Pd and N-based defects: the lack of any component in the range of 395.5–396.5 eV suggests that no Pd–N bond is formed [56]. Interestingly, there is no evidence of the formation of carbide species as well.

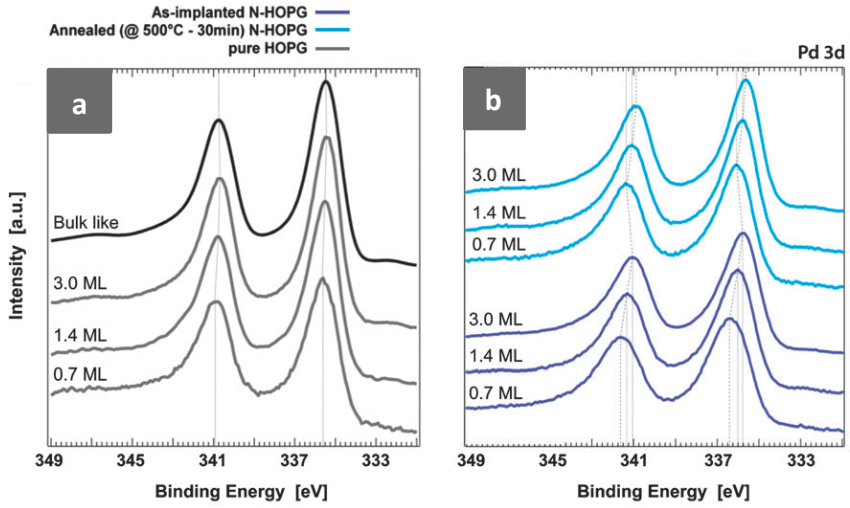

Fig. 4.14 - Pd 3d XPS data of (a) Pd(x ML)/HOPG and (b) Pd(x ML)/N-HOPG (both as-implanted and annealed, see text) systems (x = 0.7, 1.4 and 3.0).

To confirm the absence of interfacial reactions between the metal and our chemically modified substrate, we expanded the analysis to Co NPs, which are well known to interact with nitrogen [57,58]. Even in this case, we cannot observe any low BE component, which demonstrates that no Co–N bond is formed.

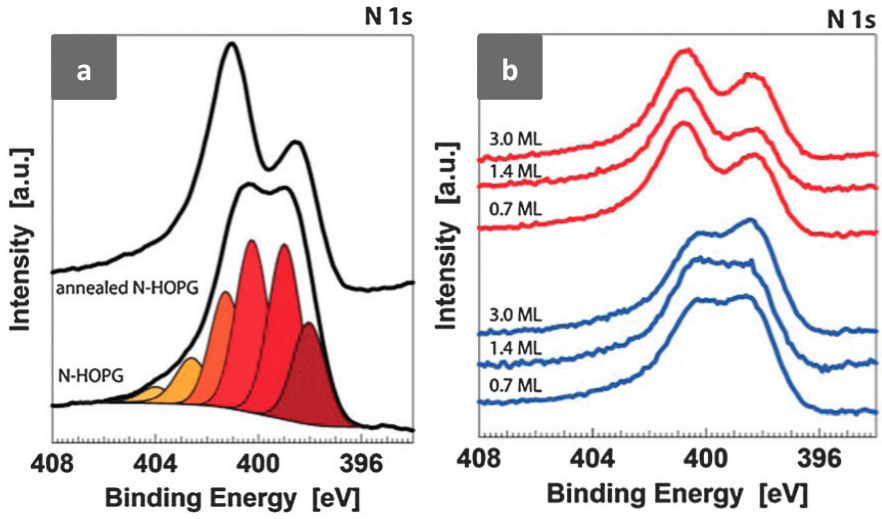

Fig. 4.15 - N 1s XPS data for N-HOPG, annealed N-HOPG and Pd(x ML)/N-HOPG: (a) spectra of the substrates together with the fitted components; (b) spectra of the Pd(x ML)/N-HOPG system of the as-implanted (blue curves) and annealed Pd(x ML)/N-HOPG (red curves) systems (x = 0.7, 1.4 and 3.0).

On the basis of these data, we can safely state that N implantation in HOPG under the adopted experimental conditions generates N-based defects that are mostly localized in a region underneath the surface, i.e. not accessible for bonding with metal NPs. On the other hand, the ion implantation leads also to partial amorphization of the surface, which presents morphological defects that may act as preferential nucleation sites for metal NPs.

4.6 Activity toward Oxygen Reduction Reaction

The last examined redox process, in this chapter, is the reduction of O_2, which is reported to be sensitive to the presence of nitrogen functional groups. It is worth noting, however, that many of these studies used electrodes presenting metal cations such as Fe [7], Co and Ni [59] or metal NPs on the surface in concomitance with nitrogen functional groups. Therefore, these literature reports do not unambiguously establish the role of surface nitrogen on the kinetics of O_2 electroreduction.

N-HOPG and Ar-HOPG were comparatively examined toward ORR in order to clarify whether the presence of nitrogen functional groups is indeed beneficial for the reduction of O_2. In fact, several other papers concerning nitrogen-doped materials such as graphene [4], carbon nanotubes [35] or carbon nanofibers [7] have established an increased catalytic activity toward ORR. However, in the present investigation, we aim to understand the net effect of doping since the catalytic activity can be evaluated without the interference due to different porosity, surface area and degree of crystallinity. Furthermore, any possible effects arising from the electrode supports or from metallic contaminants coming from the doping procedure are avoided. In an effort to compare more directly the influence of nitrogen implantation in ORR we have tested the freshly cleaved HOPG and both Ar-HOPG and N-HOPG electrodes in an O_2 saturated 0.1 M H_2SO_4 solution: the results are shown in Fig. 4.16 and compared with the electrolyte background (indexed numbers).

A remarkable difference can be seen between the implanted and pristine HOPGs. In fact, both Ar-HOPG and N-HOPG show a single cathodic peak for the

irreversible reduction of O_2 and a more positive onset potential for the O_2 reduction reaction of 90 and 280 mV, respectively.

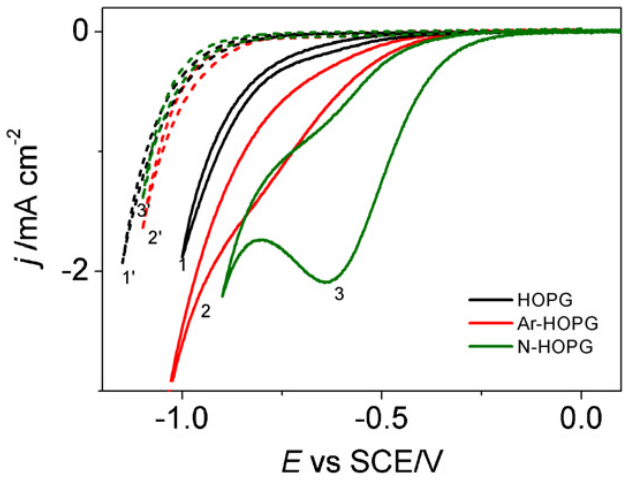

Fig. 4.16 - CV response of HOPG (1), Ar-HOPG (2) and N-HOPG (3) in a O_2-saturated 0.1 M H_2SO_4, recorded at a scan rate 0.03 V s^{-1}. The indexed numbers are the corresponding CV responses in the absence of O_2.

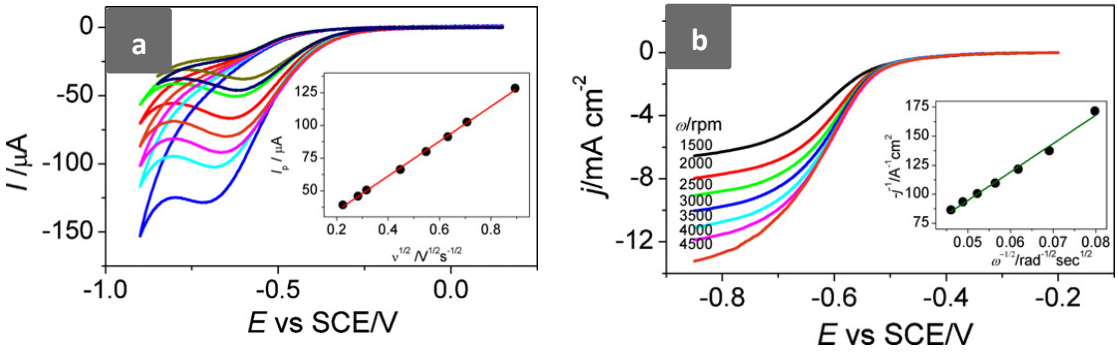

Fig. 4.17 - (a) CV response of N-HOPG electrode in O_2-saturated 0.1 M H_2SO_4 as a function of scan rate. The inset plot shows the cathodic peak current versus the square root of the scan rate. (b) RDE voltammetry curves for the ORR at N-HOPG electrode obtained at different rotation speeds. The inset shows the corresponding Koutecky–Levich plot (scan rate, 5 mV s^{-1}) at E = -0.85 V vs SCE.

The positive potential shift implies that the N-HOPG electrodes show a higher catalytic activity for ORR compared with Ar-HOPG and pristine HOPG. N-HOPG

electrode shows a well-defined diffusion peak at -0.64 V vs. SCE, while Ar-HOPG shows a more stretched and less defined peak that is indicative of a more sluggish kinetics. The observed peak current for O_2 reduction at N-HOPG was found to be proportional to the square root of the scan rate, which is consistent with a diffusion-controlled process (inset Fig. 4.17a).

ORR at N-HOPG was also studied using the RDE method (Fig. 4.17b): the measurements were carried out at different electrode rotation rates and the data were analyzed using the Koutecky–Levich (K–L) equation (Eq. (4.1)) to verify the number of transferred electrons and therefore the predominant pathway for the ORR.

$$\frac{1}{j} = \frac{1}{j_k} + \frac{1}{j_d} = \frac{1}{nFkC_{O_2}} + \frac{1}{0.62nF(D_{O_2})^{2/3}v^{-1/6}C_{O_2}\omega^{1/2}} \qquad [4.1]$$

In the K–L equation, j is the measured current density, j_k and j_d are the kinetic and diffusion-limited current densities, respectively, n is the number of electrons transferred per O_2 molecule, k is the rate constant for O_2 reduction, F is the Faraday constant (96,485 C mol^{-1}), ω is the rotation rate, C_{O_2} is the concentration of oxygen in the bulk (1.1×10^{-6} mol cm^{-3}) [60], D_{O_2} is the diffusion coefficient of oxygen (1.4×10^{-5} cm^2 s^{-1}) [61] and v is the kinematic viscosity of the solution (0.01 cm^2 s^{-1}) [61]. The slope of the straight lines (see inset of the Fig. 4.17b for an exemplary plot), allows us to assess the number of electrons involved in the ORR. At N-HOPG electrode a value of 3.95 ± 0.12 was reproducibly found at E = -0.64 V vs. SCE, indicating that O_2 is reduced to H_2O according to the reaction:

$$O_2 + 4H^+ + 4e^- \rightarrow 2H_2O \qquad [4.2]$$

The results obtained clearly state that the activity of the N-HOPG toward ORR is the result of nitrogen doping since both Ar-HOPG and N-HOPG possess similar surface morphology and surface area, but different chemical surface functionalization. The enhanced catalytic activity at N-HOPG with respect to Ar-HOPG arises from the chemical interaction between O_2 and nitrogen functional groups, possibly through preferential adsorption and reactions at these sites.

Besides HOPG and N-HOPG, the electrocatalytic properties of Pd/HOPG and Pd/N-HOPG were examined and compared to that bulk Pd. The aim of this investigation was to assess the catalytic properties of supported Pd NPs and also to understand if the presence of nitrogen functional groups triggers electronic interactions that can promote the catalytic activity of the metal. Cyclic voltammograms at Pd(bulk), N-HOPG, Pd(1.4 ML)/HOPG and Pd(1.4 ML)/N-HOPG in 0.1 M H_2SO_4 at a scan rate of 200 mV s^{-1} are presented in Fig. 4.18a and b. The clean N-HOPG support exhibits a wide potential window, whereas Pd/HOPG and Pd/N-HOPG show lower overpotential towards hydrogen evolution because of the presence of Pd on the support. However, the typical features of bulk Pd (Fig. 4.18a) or Pd deposited on glassy carbon [62] in an aqueous electrolyte, i.e. the hydrogen adsorption–desorption peaks and the Pd oxide peak, are missing. This indicates a different EC behaviour of Pd NPs with respect to Pd (bulk) and in particular a relative inertness of Pd NPs supported on HOPG towards the formation of an oxide layer. Fig. 4.18c shows the catalytic activity of the above-mentioned electrodes towards ORR. Pd bulk electrode and clean N-HOPG are active towards ORR though to a different extents and show a well-defined diffusion peak at 0.13 and -0.62 V, respectively. The deposition of 1.4 ML of Pd on HOPG and N-HOPG results in electrodes with similar properties; the two electrodes exhibit very similar CV responses. Actually, apart from a minor difference in peak current density, possibly associated with a different active surface area, the two Pd-based electrodes have similar electrocatalytic activities (Fig. 4.18c).

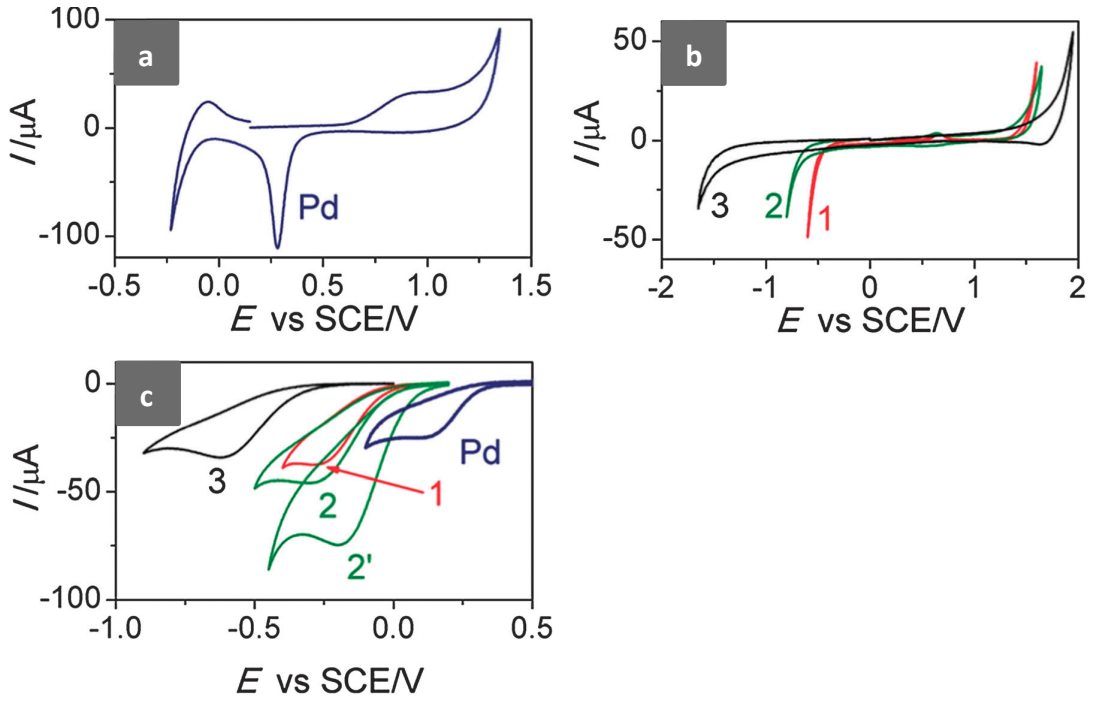

Fig. 4.18 - Cyclic voltammograms of bulk Pd, Pd(1.4 ML)/HOPG (1), Pd(1.4 ML)/ N-HOPG (2), Pd(3.0 ML)/N-HOPG (2') and N-HOPG (3) in 0.1 M H_2SO_4 (a and b) and O_2 saturated 0.1 M H_2SO_4 (c).

Both Pd/HOPG and Pd/N-HOPG show a reduction peak for O_2 at -0.275 V, which is a compromise of the two limiting cases represented by the reduction of O_2 at N-HOPG and Pd electrodes. In this sense, the effect of supporting Pd NPs on HOPG does not improve the catalytic activity with respect to the bulk Pd electrode. However, the aspect of interest is that the doping of the HOPG surface does not affect the catalytic activity of Pd NPs with respect to the undoped HOPG. This is a clear indication that introduction of nitrogen functional groups onto the electrode support does not affect the catalytic activity of the Pd NPs. Therefore if a synergic effect between nitrogen induced defects and Pd NPs is present, it is very modest. On the other hand, the catalytic activity is dependent on the number of monolayers deposited on the N-HOPG surface. Fig. 4.18b clearly shows that in the case of Pd(3.0 ML)/N-HOPG there is a shift of almost 100 mV in the O_2 reduction potential with respect to Pd(1.4 ML)/N-HOPG. In addition, Pd(3.0 ML)/N-HOPG shows higher current density with respect to both bulk Pd and Pd(1.4 ML)/N-HOPG as a result of an increased active surface area.

Bibliography

[1] McCreery, R.L. *Chem. Rev.* **2008**, *108*, 2646.

[2] Welch, C.M.; Compton, R.G. *Anal. Bioanal. Chem.* **2006**, *384*, 601.

[3] Scrosati, B.; Garche, J. *J. Power Sources* **2010**, *195*, 2419.

[4] Qu, L.; Liu, Y.; Baek, J.B.; Dai, L. *ACS Nano* **2010**, *4*, 1321.

[5] Sheng, Z.H.; Shao, L.; Chen, J.J.; Bao, W.J.; Wang, F.B.; Xia, X.H. *ACS Nano* **2011**, *5*, 4350.

[6] Zhou, Y.; Pasquarelli, R.; Holme, T.; Berry, J.; Ginley, D.; O'Hayre, R. *J. Mater. Chem.* **2009**, *19*, 7830.

[7] Maldonado, S.; Stevenson, K.J. *J. Phys. Chem. B* **2005**, *109*, 4707.

[8] Dumitrescu, I.; Unwin, P.R.; MacPherson, J.V. *Chem. Commun.* **2009**, 6886.

[9] Yang, W.; Ratinac, K.R.; Ringer, S.R.; Thordarson, P.; Gooding, J.J.; Braet, F. *Angew. Chem. Int. Ed.* **2010**, *49*, 2114.

[10] Kusunoki, I.; Sakai, M.; Igari, Y.; Ishidzuka, S.; Takami, T.; Takaoka, T.; Nishitani-Gamo, M.; Ando, T. *Surf. Sci.* **2001**, *492*, 315.

[11] Yang, D.Q.; Sacher, E. *Surf. Sci.* **2003**, *531*, 185.

[12] Pylypenko, S.; Queen, A.; Olson, T.S.; Dameron, A.; O'Neill, K.; Neyerlin, K.C.; Pivovar, B.; Dinh, H.N.; Ginley, D.S.; Gennett, T.; O'Hayre, R. *J. Phys. Chem. C,* **2011**, *115*, 13667.

[13] Pylypenko, S.; Queen, A.; Olson, T.S.; Dameron, A.; O'Neill, K.; Neyerlin, K.C.; Pivovar, B.; Dinh, H.N.; Ginley, D.S.; Gennett, T.; O'Hayre, R. *J. Phys. Chem. C,* **2011**, *115*, 13676.

[14] Rice, R.J.; McCreery, R.L. *Anal. Chem.* **1989**, *61*, 1637.

[15] Davies, T.J.; Moore, R.R.; Banks, C.E.; Compton, R.G. *J. Electroanal. Chem.* **2004**, *574*, 123.

[16] McCreery, R.L.; McDermott, M.T. *Anal. Chem.* **2012**, *84*, 2602.

[17] Sarapuu, A.; Helstein, K.; Schiffrin, D.J.; Tammeveski, K. *Electrochem. Solid-State Lett.* **2005**, *8*, E30.

[18] Gara, M.; Compton, R.G. *New J. Chem.* **2011**, *35*, 2647.

[19] Sarapuu, A.; Helstein, K.; Vaik, K.; Schiffrin, D.J.; Tammeveski, K. *Electrochim. Acta* **2010**, *55*, 6376.

[20] Slevin, C.J.; Gray, N.J.; Macpherson, J.V.; Webb, M.A.; Unwin, P.R. *Electrochem. Commun.* **1999**, *1*, 282.

[21] Bertoncello, R.; Glisenti, A.; Granozzi, G.; Battaglin, G.; Caccavale, F.; Cattaruzza, E.; Mazzoldi, P. J. *Non-Cryst. Solids* **1993**, *162*, 205.

[22] Ziegler, J.F.; Ziegler, M.D.; Biersack, J.P. *Nucl. Instrum. Meth. B* **2010**, *268*,1818.

[23] Sternitzke, K.; McDermott, M.T.; McCreery, R.L. *J. Electrochem. Soc.* **1991**, *138*, 2412.

[24] Kinchin, G.H.; Pease, R.S. *Rep. Prog. Phys.* **1955**, *18*, 1.

[25] Marton, D.; Boyd, K.J.; Lytle, T.; Rabelais, J.W. *Phys. Rev. B* **1993**, *48*, 6757.

[26] Niimi, Y.; Kambara, H.; Fukuyama, H. *Phys. Rev. Lett.* **2009**, *102*, 026803.

[27] Smith, R.A.P.; Smith, G.C.; Weightman, P. J. *Electron. Spectrosc. Relat. Phenom.* **2006**, *152*, 152.

[28] Wei, D.; Liu, Y.; Wang, Y.; Zhang, H.; Huang, L.; Yu, G. *Nano Lett.* **2009**, *9*, 1752.

[29] Wang, T.S.; Ding, J.J.; Cheng, R.; Peng, H.B.; Lu, X.; Zhao, Y.T. *Nucl. Instrum. Meth. B* **2012**, *272*,15.

[30] Zhang, C.; Fu, L.; Liu, N.; Liu, M.; Wang, Y.; Liu, Z. *Adv. Mater.* **2011**, *23*, 1020.

[31] Usachov, D.; Vilkov, O.; Grüneis, A.; Haberer, D.; Fedorov, A.; Adamchuk, V.K.; Preobrajenski, A.B.; Dudin, P.; Barinov, A.; Oehzelt, M.; Laubschat, C. *Nano. Lett.* **2011**, *11*, 5401.

[32] Hellgren, N.; Guo, J.; Luo, Y.; Såthe, C.; Agui, A.; Kashtanov, S.; Nordgren, J.; Ågren, H.; Sundgren, J.E. *Thin Solid Films* **2005**, *471*, 19.

[33] Taylor, J.A.; Lancaster, G.M.; Rabalais. J.W. *J. Am. Chem. Soc.* **1978**, *100*, 4441.

[34] Zhang, L.; Zhenhai. X. *J. Phys. Chem. C* **2011**, *115,* 11170.

[35] Gong, K.; Du, F.; Xia, Z.; Dustock, M.; Dai, L. *Science* **2009**, *323*, 760.

[36] Wu, G.; More, K.L.; Johston, C.M.; Zelenay, P. *Science* **2011**, *332*, 443.

[37] Cline, K.K.; McDermott, M.T.; McCreery, R.L. *J. Phys. Chem.* **1994**, *98*, 5314.

[38] Banks, C.E.; Compton, R.G. *Analyst* **2006**, *131*, 15.

[39] Nicholson, R.S. *Anal. Chem.* **1965**, *37*, 1351.

[40] Banks, C.E.; Davies, T.J.; Wildgoose, G.G.; Compton, R.G. *Chem. Commun.* **2005**, *7*, 829.

[41] Davies, T.J.; Hyde, M.E.; Compton, R.G. *Angew. Chem. Int. Ed.* **2005**, *44*, 5121.

[42] Williams, C.G.; Edwards, M.A.; Colley, A.L.; Macpherson, J.V.; Unwin, P.R. *Anal. Chem.* **2009**, *81*, 2486.

[43] McDermott, M.T.; Kneten, K.; McCreery. R.L. *J. Phys. Chem.* **1992**, *96*, 3124.

[44] Gerischer, H. *J. Phys. Chem.* **1991**, *95*, 1356.

[45] Bowling, R.; Packard, R.T.; McCreery, R.L. *Langmuir* **1989**, *5*, 683.

[46] Mahè, E.; Devilliers, D.; Comninellis, C. *Electrochim. Acta* **2005**, *50*, 2263.

[47] Bowling, R.J.; Packard, R.T.; McCreery, R.L. *J. Am. Chem. Soc.* **1989**, *111*, 1217.

[48] Zhou, Y.; Holme, T.; Berry, J.; Ohno, T.R.; Ginley, D.; O'Hayre, R. *J. Phys. Chem. C* **2010**, *114*, 506.

[49] Alwarappan, S.; Erdem, A.; Liu, C.; Li, C.Z. *J. Phys. Chem. C* **2009**, *113*, 8853.

[50] Binns, C.; Baker, S. H.; Demangeat, C.; Parlebas, J. C. *Surf. Sci. Rep.* **1999**, *34*, 105.

[51] Vijayakrishnan, V.; Chainani, A.; Sarma, D.D.; Rao, C.N.R. *J. Phys. Chem.,* **1992**, *96*, 8679.

[52] Aiyer, H.N.; Vijayakrishnan, V.; Subbanna, G.N.; Rao, C.N.R. *Surf. Sci.* **1994**, *313*, 392.

[53] Rao, C.N.R.; Kulkarni, G.U.; Thomas P.J.; Edwards, P.P. *Chem. Eur. J.* **2002**, *8*, 28.

[54] Hüfner, S.; Wertheim, G.K.; Buchanan, D.N.E. *Chem. Phys. Lett.* **1974**, *24*, 527.

[55] Favaro, M.; Perini, L.; Agnoli, S.; Durante, C.; Granozzi, G.; Gennaro, A. *Electrochim. Acta* **2013**, *88*, 477.

[56] Bertóti, I. *Surf. Coat. Technol.* **2002**, *194*, 151.

[57] Lee, K.; Zhang, L.; Liu, H.; Hui, R.; Shi, Z.; Zhang, J. *Electrochim. Acta* **2009**, *54*, 4704.

[58] Shi, Z.; Liu, H.; Lee, K.; Dy, E.; Chlistunoff, J.; Blair, M.; Zelenay, P.; Zhang J.; Liu, Z.S. *J. Phys. Chem. C* **2011**, *115*, 16672.

[59] Chen, Z.; Higgins, D.; Yu, A.; Lei Zhang, L.; Zhang, J. *Energy Environ. Sci.* **2011**, *4*, 3167.

[60] Gottesfeld, S.; Raistrick, I.D.; Srinivasan, S. *J. Electrochem. Soc.* **1987**, *134*, 1455.

[61] Song, C.; Zhang, J. *PEM Fuel cell Electrocatalyst and Catalyst layers, Fundamentals and Applications*, Springer-Verlag, London, (**2008)**.

[62] Tateishi, N.; Yahikozawa, K.; Nishimura, K.; Suzuki, M.; Iwanaga, Y., Watanabe, M.; Enami, E.; Matsuda Y.; Takasu, Y. *Electrochim. Acta* **1991**, *36*, 1235.

GLASSY CARBON

5.1 Chemical and Electrochemical properties

An electrochemically important variant of the graphite structure is glassy carbon (GC), which is made by heat-treating various polymers, like polyacrylonitrile. By heating the polymer under pressure in an inert atmosphere to 1000-3000 °C, the heteroatoms are evaporated until only carbon remains. The C-C bonds in the polymer backbone don't break at these temperatures, so the carbon can form graphitic planes of only limited size, with L_a and L_c in the range of 30-70 Å.

Whereas HOPG is composed of well-ordered sp^2 sheets, as shown in Fig. 5.1 GC has an amorphous structure, though, like HOPG, it is prevalently sp^2 hybridized.

L_a: in-plane microcrystalline size
L_c: inter-planar microcrystalline size

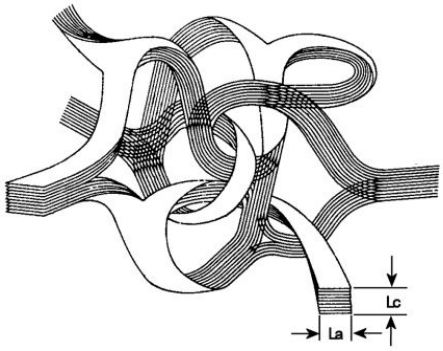

Fig. 5.1 - Structure model of GC.

Among various forms of carbon, GC is the most important for use as an electrode, since it shows very low electrical resistivity, it is non-porous and impermeable to gases, it has high chemical resistance and the widest potential range observed for graphitic carbon electrodes and, last but not least, it can be easily polished and handled [1]. This renders GC an optimal material for a basic investigation on how the chemical modifications of the support can affect the activity of the loaded catalyst. In principle, the catalytic activity can be increased either by a fine dispersion of the NPs or by modulating the electronic properties of the catalyst NPs by interaction with the chemical or morphological defects of the support; as an example, a way to enhance the durability of the catalyst support assembly in the case of oxygen reduction is to

strengthen the interaction between catalyst NPs and support by introducing into the substrate defects that can act as trapping sites for anchoring the NPs [2,3]. In this regard, Minguzzi et al. have recently observed that the electrochemical activation of a carbon surface in acidic media introduces oxygen functional groups, which enhance the stability and the electrocatalytic activity of Ag NPs toward the C-X bond activation [4]. The chemical modification (hereafter referred to as doping) of a GC surface is generally performed by adsorption or by covalent bonding (grafting) of molecular catalysts or electronic mediators. Another option is to synthetize a doped GC by thermolysis of suitable carbon precursors (usually polymers) containing the desired heteroatoms [1,5] or by a mixture of resins and an inorganic source of heteroatoms, such as boric acid, ammonia, etc. [6]. In the present work, following a different approach, nitrogen functional groups have been introduced onto a GC support by N_2^+ and N^+ ion implantation and by carbamic acid electrolysis [7], producing a modified N-GC support.

After that, palladium was employed as metal NPs, because of its excellent hydrogenation ability, which makes it an excellent catalyst in the electrochemical dechlorination of organic chlorides in aqueous media or organic-aqueous mixtures [8-10].

Here it will be shown that the presence of nitrogen functional groups on the carbonaceous support can influence the nucleation and growth of metal NPs and promote their catalytic activity toward activation of the C-X bond.

5.2 Characterization of pristine GC

The electrocatalytic activity of the pure and nanostructured surfaces for benzyl chloride (BnCl) reduction was investigated using cyclic voltammetry (CV) and was carried out in a three-electrode cell system with a GC, either modified or unmodified, or Pd disc as working electrode. The counter electrode and the reference electrode were a Pt wire and Ag|AgI|Bu_4NI (0.1 M) in CH_3CN, respectively. The potentials measured against the Ag|AgI|I^- reference electrode were converted to the SCE scale, to which all potentials in the following are referred, by measuring the standard potential of the ferrocenium/ferrocene couple with respect to our reference and by using $E^\circ_{Fc+/Fc} = 0.391$

V versus SCE in CH_3CN.

The working electrodes were built from a GC plate (Tokai GC-20) and 3-mm diameter Pd wire (Alfa Aesar, 99.999%) and were polished to a mirror finish with silicon carbide papers of decreasing grain size (Struers, grit: 500, 1000, 2400, 4000) followed by diamond paste (3-, 1-, 0.25-μm particle size). At the end, they were cleaned in ethanol in an ultrasonic bath for about 5 min.

First, some experiments were carried out on bare GC in order to reproduce the electrochemical behaviour already reported in the literature [11].

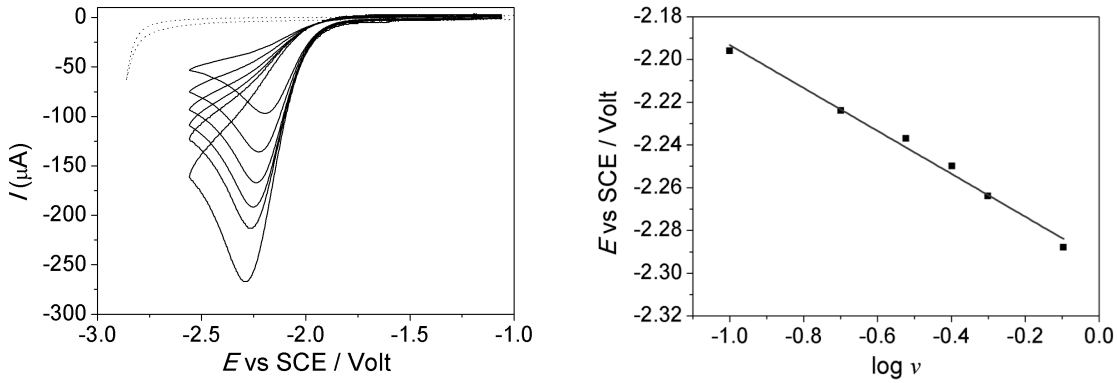

Fig. 5.2 - Cyclic voltammetry of 2 mM benzyl chloride at GC.

Table 5.1 - Voltammetric data for the reduction of BnCl in CH_3CN + 0.1 M $TEABF_4$ at 25°C at GC[a].

	E_p [a] (V *vs*. SCE)	$\partial E_p/\partial \log v$ (mV)	α	DET mechanism
GC [b]	-2.172	-94	0.32	Concerted
GC	-2.210	-100	0.30	Concerted

[a] v = 0.1 V s^{-1}; [b] data from literature [11] carried out in CH_3CN + 0.1 M $TEAClO_4$.

As shown in Table 5.1, in our conditions the peak potential of BnCl reduction is located at -2.210 V *vs.* SCE with an electron transfer coefficient equal to 0.30, characteristic of a concerted mechanism.

Before studying the electrochemical behaviour of palladium nanoparticles on GC, some experiments with the palladium bulk electrode were performed in the same conditions seen above. Sometimes a slight passivation of the Pd electrode, resulting in a poor reproducibility of the data, was observed during the electrocatalytic experiments. When this happened, the electrode was activated by CV cycles in a potential range from -0.5 V down to the cathodic discharge limit.

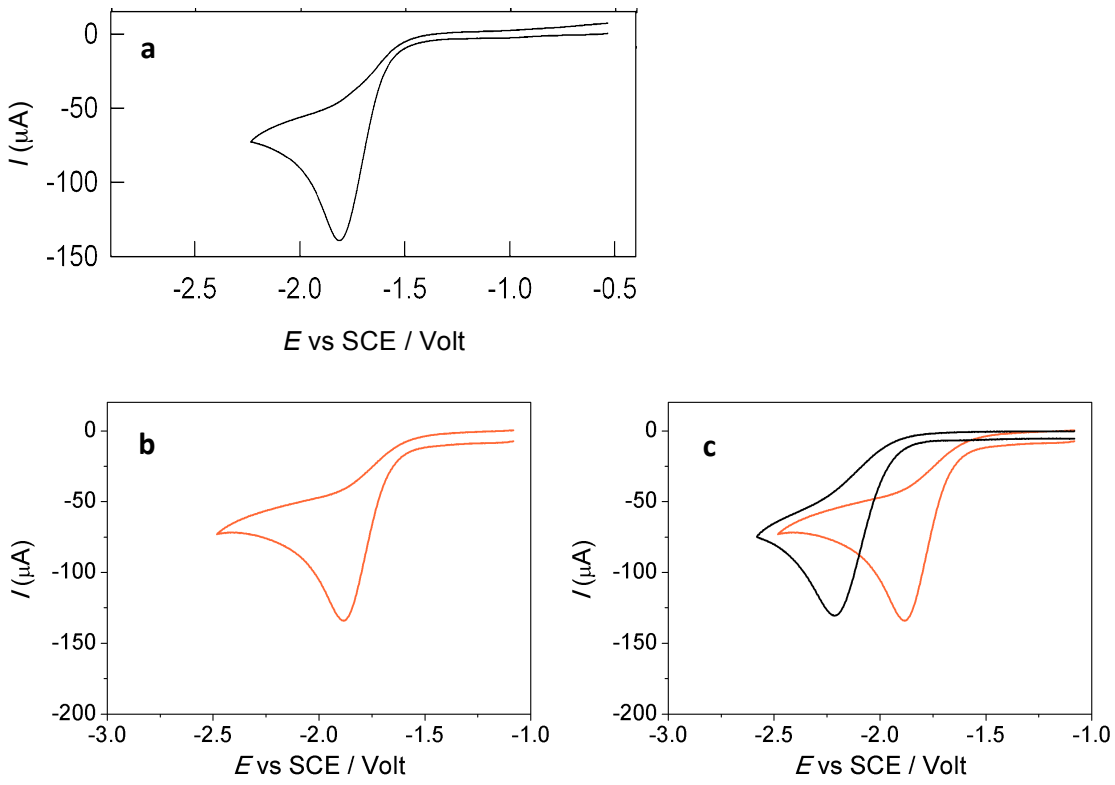

Fig. 5.3 - Cyclic voltammetry of 2 mM benzyl chloride at bulk Pd: (a) from ref. [11], (b) acquired in this work, (c) comparison between GC (black line) and Pd (red line).

Table 5.2 - Voltammetric data for the reduction of BnCl in CH_3CN + 0.1 $TEABF_4$ at 25 °C at Pd[a].

	E_p[a] (V *vs.* SCE)	$\partial E_p/\partial \log v$ (mV)	α	DET mechanism
Pd [b]	-1.720	-101	0.29	Concerted
Pd	-1.882	-114	0.26	Concerted

[a] v = 0.1 V s^{-1}; [b] data from literature [11] carried out in $TEAClO_4$.

After investigating the electrochemical behaviour of benzyl chloride on GC and Pd, we turned to Pd NPs on GC, to test whether the catalytic activity of Pd can be affected by nanostructuring and/or by the nature and morphology of the support for Pd NPs.

5.3 Deposition of Palladium NPs on GC

Pd NPs on GC were freshly prepared before each experiment by electrodeposition of Pd on an exposed area of a 3-mm diameter GC disk. The GC samples (8 mm diameter) were enveloped in a Teflon tape. The electrochemical deposition of Pd NPs was carried out in a three-electrode cell system containing 1 mM $PdSO_4$ solution in 0.1 M H_2SO_4. A GC disk was set as working electrode, while the counter electrode and the reference electrode were a Pt wire and $Hg|Hg_2SO_4|K_2SO_4$(sat), respectively. To avoid any contamination of the working electrode, the reference electrode was in put a separate compartment and connected to the working electrode solution by a salt bridge. The conversion of the potential measured versus $Hg|Hg_2SO_4|SO_4^{2-}$ to the SCE scale is obtained by adding +0.373 V to the measured value.

Pd NPs were deposited on the GC through a double potential step deposition (Fig. 5.4); both the potential of nucleation (E_n) and the potential of growth (E_g) were chosen by recording a cyclic voltammogram before each experiment (Fig. 5.4).

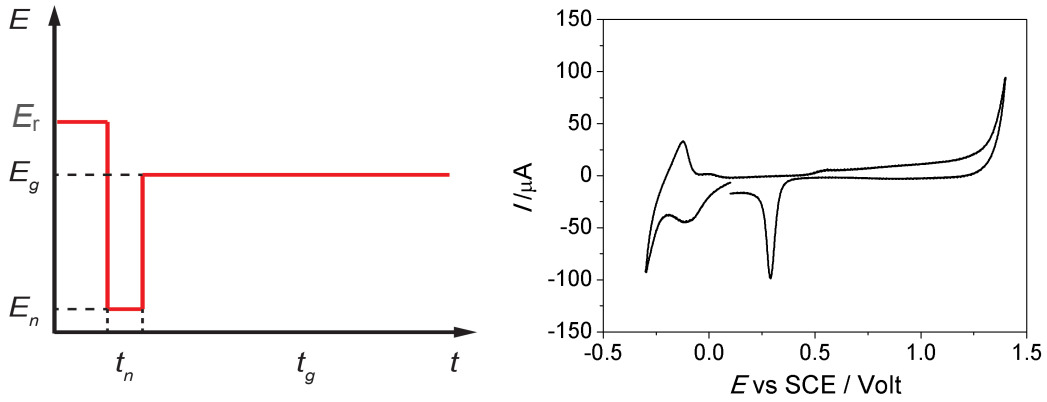

Fig. 5.4 - Double potential step program for Pd deposition (left) and cyclic voltammetry of 1 mM $PdSO_4$ in 1 M $HClO_4$ at GC (right).

We first investigated the redox reactions of palladium on GC by CV in 1 mM $PdSO_4$ + 0.1 M $HClO_4$ solution. The first negative-going scan obtained under these conditions shows no well-defined cathodic peak for the reduction of Pd^{2+} to $Pd^{(0)}$. CVs obtained starting at an initial potential of 0.3 V *vs*. SCE and scanning in the negative direction at variable negative potential limits indicate that Pd deposition starts at a potential more negative than −0.05 V *vs*. SCE. which coincides with the equilibrium potential. This was confirmed by the appearance of a PdO peak on the reverse scan and by XPS measurements revealing the presence of Pd over the GC surface.

The first nucleation step (E_n) was set at a sufficiently negative potential of −0.25 V *vs*. SCE, to allow instantaneous nucleation of Pd and start deposition under a diffusion-controlled rate. In the second growth step (E_g) the potential was set at −0.077 V *vs*. SCE. At this potential the process is under kinetic control and the process proceeds growth of Pd NPs without further nucleation of new sites. The solution was oxygen-free and unstirred during the deposition. The deposition current was recorded and integrated in order to determine the total deposition charge (Table 5.3).

Table 5.3 - Optimized deposition conditions for Pd NPs on GC supports.

	E_r (V)[a,b]	t_r (s)[c]	E_n (V)[b]	t_n (s)	E_g (V)[b]	t_g (s)	Q (C)[d]
GC	0.3	10	-0.25	0.1	-0.077	50	2.74E-4

[a] Rest potential. [b] Potentials are versus SCE. [c] Rest time. [d] Values obtained from the mean of at least 5 different experiments.

The electrochemical deposition of Pd on GC was out at three different growth times, namely, 25, 50 and 150 s, resulting in the formation of NPs of an average size depending on the growth time (t_g). Working with variable growth time also allowed preparation of modified electrodes with different coatings, which were tested to look for any relation between degree of coating and catalytic activity.

NPs deposited for 25 s have a typical Volmer–Weber growth and an average size of 23 nm (Fig. 5.5 a and b). The increase of the growth time from 25 to 50 s increases the Pd amount loaded over the GC support and changes the dimensions of the Pd NPs according to a Gaussian distribution centered at 40 nm (Fig. 5.5 c and d). It is worth

noting that in this case NPs agglomerates of 100-300 nm size are also present as a result of the preferential growth of Pd NPs over the pre-existing metal seeds. At a deposition time of 150 s the distribution of the particle size assumes a maxima at 45 nm. In this case, the growth of NPs agglomerates is even more emphasized (Fig. 5.5 e and f).

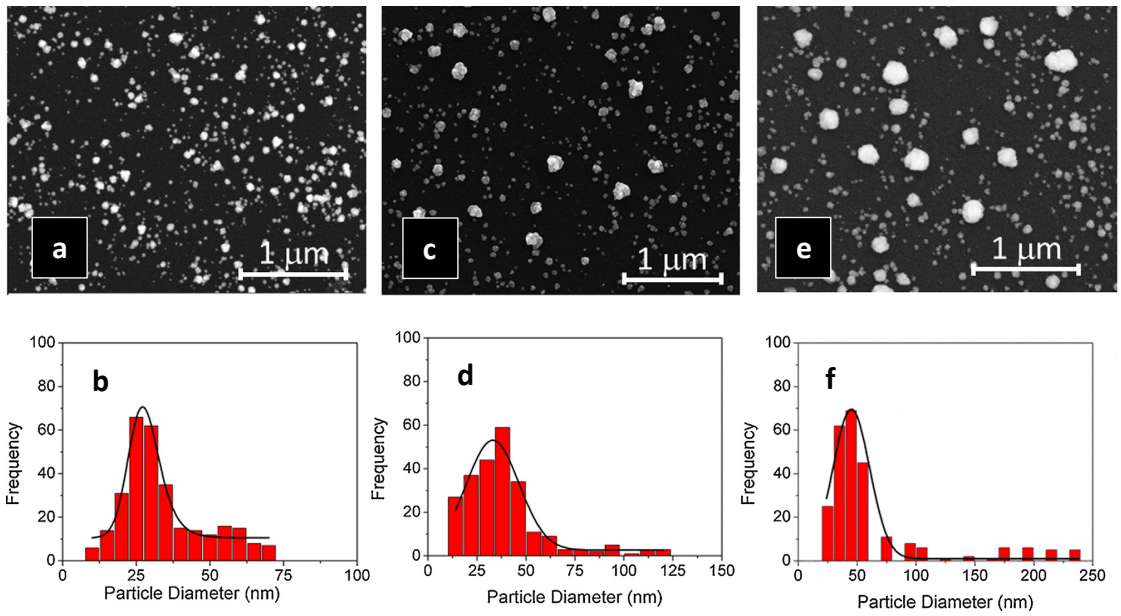

Fig. 5.5 - SEM images and particle size distributions for Pd@GC at different growth times: (a and b) t_g = 25 s; (c and d) t_g = 50 s; (e and f) t_g = 150 s.

5.4 Ion implantation and Electrochemical doping

5.4.1 Doping by N_2 and Ar ion implantation

For the preparation of N- and Ar-GC samples an ion beam produced by an ion gun (Thermo VG Scientific) was used under the conditions: 2.2×10^{-6} mbar background of N_2 or Ar, a beam energy of 500 eV and exposure time of 10 min, with an incidence angle of the ion beam equal to 45° with respect to the sample surface (the ion current measured during this treatment was 2.0 µA and the total dose of implanted atoms was around 5×10^{16} ion cm^{-2}). The nitrogen/argon dose was evaluated to be about 15 at%. XPS characterization of the samples was performed in a UHV chamber (base pressure < 5×10^{-9} mbar), equipped with a double anode X-ray source (Omicron) and a

hemispherical electron analyzer (VG Scienta). All XPS measurements were performed at room temperature, using non-monochromatic Mg-Kα radiation ($h\nu$ = 1253.6 eV) and pass energy of 50 eV and 20 eV for the survey and high-resolution spectra, respectively. The calibration of the binding energy (BE) scale was carried out using Au 4f as reference. The N 1s and C 1s peaks were deconvoluted into individual components (after Shirley background removal) using symmetrical Voigt functions. The χ^2 minimization was ensured by the use of nonlinear least-squares.

The surface chemistry the different GCs was first investigated by means of XPS. In Figure 5.6 the survey spectra of the different samples, recorded before the electrochemical deposition of Pd, are shown.

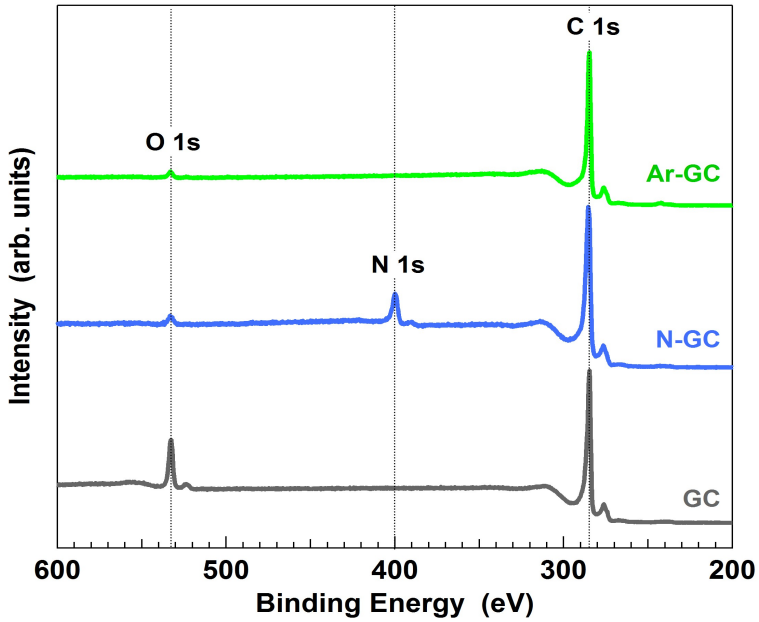

Fig. 5.6 - Wide scan XPS surveys of Ar-GC, N-GC and GC

The surveys of all three samples clearly show similar features that account for the presence of carbon and oxygen, while nitrogen is present only in the case of N-GC. It is important to note how the Ar sputtering and N doping induce a cleaning of the surface from oxygen functional groups. From the analysis of N 1s and C 1s XPS peaks, we can determine an overall surface stoichiometry of $C_{0.85}N_{0.15}$ in N-GC

Furthermore, while in Ar-GC we observe only morphological defects, consisting of a re-hybridization from C_{sp^2} to C_{sp^3}, in N-GC, we can distinguish between different chemical defects. In fact, by deconvoluting the N 1s XPS peak (Fig. 5.7a), we can single out the presence of pyridinic groups (398.0 eV), -C≡N terminal groups (398.9 eV), pyrrolic groups (400.1 eV), N graphitic defects (401.2 eV) and N^+ ion trapped into carbon vacancies (402.6 eV) [12,13]. A further component present at high BE (404 eV) can be assigned to the interaction between nitrogen and oxygen with the formation, of NO_x groups, though in a very limited amount. Although GC has a randomly oriented structure over large dimensions, it contains a graphitic microcrystalline structure; therefore, we may assume that the effect of the ion implantation would increase the number of defects on the graphitic structures, resulting in an increased number of edges. If so, it is reasonable to assume that nitrogen groups are placed near these new edges of the graphitic microstructure. A pictorial view of nitrogen defects is proposed in Fig. 5.7b.

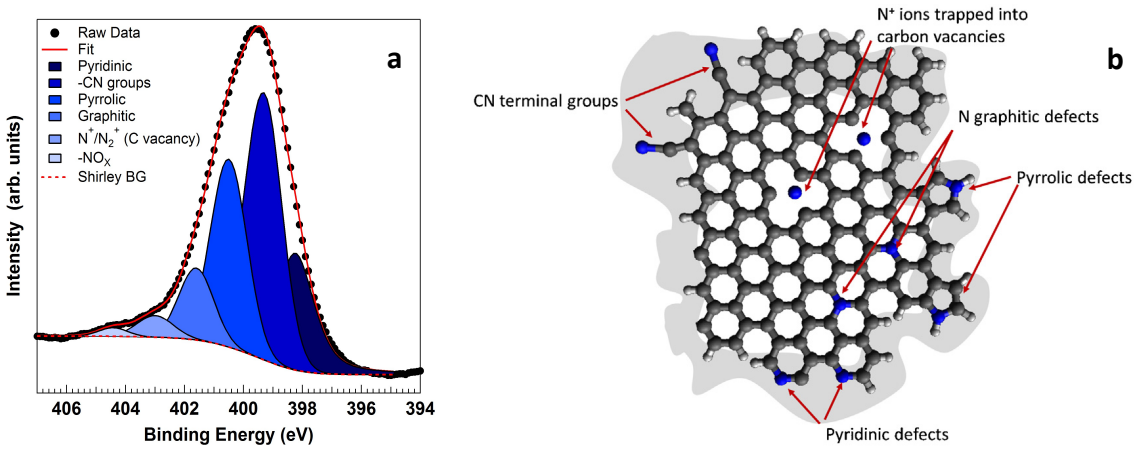

Fig. 5.7 - (a) N 1s XPS peak and relative deconvolution by means of chemically shifted components in N-GC; (b) Ball-and-stick model of the different chemical species obtained after ion implantation in GC according to the XPS N 1s data. The evidenced area corresponds to edge defects.

The electrochemical reduction of BnCl was investigated by CV at the two modified GC electrodes (Ar- and N-GC).

As can be clearly seen in Figure 5.8 and Table 5.4, reductive cleavage of the

carbon-halogen bond in BnCl on the modified electrodes occurs at a more negative potential than on bare GC. This happens because, during the sputtering, the oxygen functional groups on the surface of GC were removed. It is indeed widely known that these groups possess a catalytic activity for this kind of reaction (refer to Chapter 2). Moreover, during the sputtering, the C-C bonds in the GC substrate are subjected to a partial re-hybridization from sp^2 to sp^3, which worsens the conductivity and the tendency of the material for electron transfer.

In conclusion, the modified GC becomes more inert to reduction of the carbon-halogen bond after Ar and N treatment.

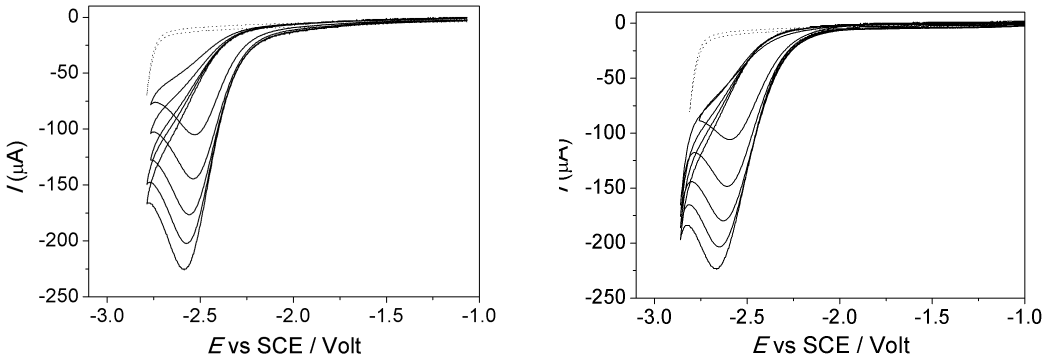

Fig. 5.8 - Cyclic voltammetry of 2 mM benzyl chloride at Ar-GC (left) ad N-GC (right).

Table 5.4 - Voltammetric data for the reduction of BnCl in CH_3CN + 0.1 $TEABF_4$ at 25 °C at Ar- and N-GC.

	E_p [a] (V *vs.* SCE)	$\partial E_p/\partial \log \upsilon$ (mV)	α	DET mechanism
Ar-GC	-2.528	-117	0.25	Concerted
N-GC	-2.590	-112	0.26	Concerted

[a] $\upsilon = 0.1$ V s^{-1}

5.4.2 Doping by carbamate electrolysis

Another way, used in this thesis, to modify a GC electrode with nitrogen functional groups is by electrolysis of carbamic acid. The introduction of the amino

groups on the GC surface is possible by controlling the electrolytic conditions, such as the electrode potential or the electrolytic current. This method was previously reported by Uchiyama et al. [7] and it appears to be a good alternative to, and even more advantageous than, the UHV doping method. So, we selected it as an alternative way of preparing N-modified GC electrodes.

We used the best conditions suggested by the studies of Uchiyama et al. for the preparation of a GC surface with good performance and with the highest content in nitrogen. Therefore, a solution of Ammonium Carbamate (0.1 M, pH 9.0) in PBS (0.1 M) was electrolyzed on GC anode at +1.1 V *vs.* Ag/AgCl/Cl$^-$ for 1 h. The current for electro-oxidation of carbamate was monitored during electrolysis and the recorded cronoamperometric curve is shown in Figure 5.10. The observed increase of the current during electrolysis may be due to an increase of the active surface area of the electrode.

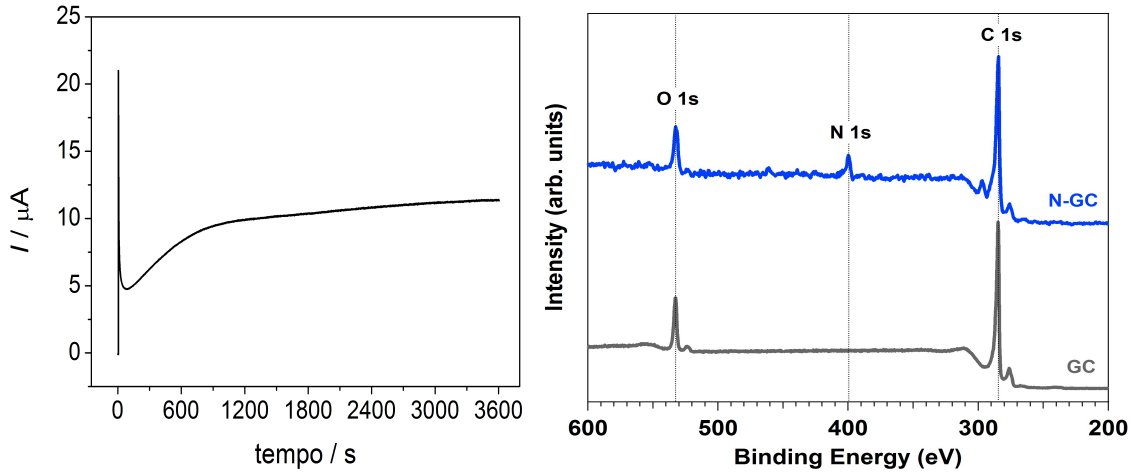

Fig. 5.9 - Variation of the oxidation current of carbamate obtained by constant potential amperometry by using a glassy carbon electrode. Electrode potential: +1.1 V *vs.* Ag/AgCl/Cl$^-$. – wide scan XPS surveys of GC and N-GC.

Even in this case, the surface chemistry of GC and N-GC was investigated by means of XPS; the two samples clearly show similar features that account for the presence of carbon and oxygen, whereas nitrogen (5.2 at%) is present only in the case of N-GC. The N 1s XPS peak (Fig. 5.10a) was deconvoluted to distinguish between the

several functional groups generated during this different synthesis procedure. We can single out the presence of pyridinic (397.8 eV), amminic (399.0 eV), pyrrolic (400.1 eV) and N graphitic (401.2 eV) defects, together with other two components (402,5 and 403,7 eV), which can be assigned to the interaction between nitrogen and oxygen with the formation of C-NO and NO_x groups.

This kind of doping, in comparison with the one obtained by UHV, brings about the formation of a large amount of ammine groups, never found before. The ammine group comes from the electro-oxidation of carbamate, which probably releases radicals such as for example $NH_2^{\cdot}$.

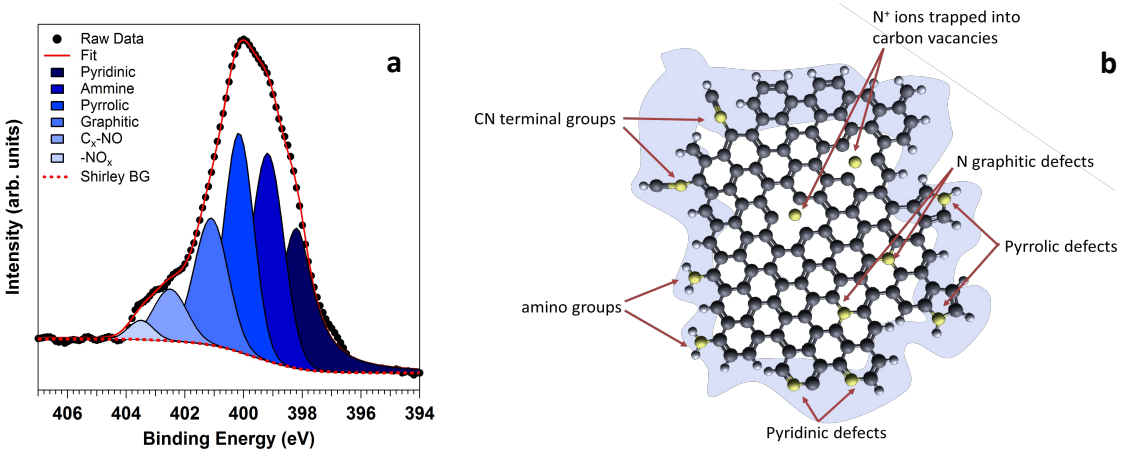

Fig. 5.10 - (a) N 1s XPS peak and relative deconvolution by means of chemically shifted components in N-GC; (b) Ball-and-stick model of the different chemical species obtained after ion implantation in GC according to the XPS N 1s data. The evidenced area corresponds to edge defects.

5.5 Deposition of Palladium NPs on doped GC

After investigating by XPS the surface chemistry of both doped and undoped GCs, we used them as support for palladium electrodeposition. The deposition was carried out in the same way previously described for electrodeposition of Pd on pristine GC; however, in the case of N-GC the E_n and E_g potentials were adjusted taking into account that the reduction of peak potential of Pd^{2+} at this electrode is slightly different from that observed on pristine GC (compare Figures 5.4 and 5.11).

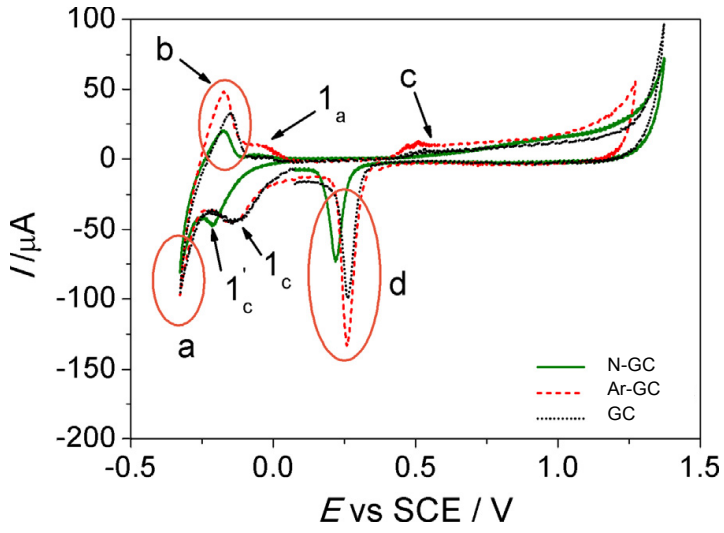

Fig. 5.11 - Cyclic voltammetry of 1 mM Pd^{2+} on pristine and modified GCs in 0.1 M H_2SO_4 solution; scan rate 200 mV s^{-1}.

Pd NPs deposited on GC and modified GCs show the typical electrochemical behaviour of palladium nanostructured electrodes (Fig. 5.11) [14,15], which is characterized by a hydrogen adsorption peak labelled as ***1c*** and a hydrogen desorption peak (***1a***), a zone labelled as ***a*** where hydrogen evolution occurs, a zone labelled as ***b*** due to the oxidation of hydrogen atoms adsorbed onto the $Pd^{(0)}$ NPs during the negative-going scan and a zone labelled as ***c*** due to the formation of PdO, which give rise to an cathodic stripping labelled as ***d***.

Table 5.5 - Optimized deposition conditions for Pd NPs on various GC supports.

	E_r (V)[a,b]	t_r (s)[c]	E_n (V)[b]	t_n (s)	E_g (V)[b]	t_g (s)	Q (C)[d]
GC	0.3	10	-0.25	0.1	-0.077	50	2.74E-4
Ar-GC	0.3	10	-0.25	0.1	-0.077	50	2.75E-4
N-GC	0.3	10	-0.25	0.1	-0.127	50	2.78E-4

[a] Rest potential. [b] Potentials are versus SCE. [c] Rest time. [d] Values obtained from the mean of at least 5 different experiments.

The results in Table 5.5 indicate that a comparable amount of charge is consumed for all three samples and therefore the mass of Pd loaded over the three different GCs is fairly similar. Fig. 5.12b shows the Pd 3d XPS spectra (the photoemission peaks were deconvoluted into chemical-shifted components using Doniach–Sunjich shape functions). As can be seen, the Pd 3d photoemission peak presents a full width at half maximum (FWHM) compatible with the presence of both metal Pd and Pd^{2+} species (BE Pd^{0}= 335.1 eV, BE Pd^{2+}= 336.2 eV), and no significant change is observed in the three cases.

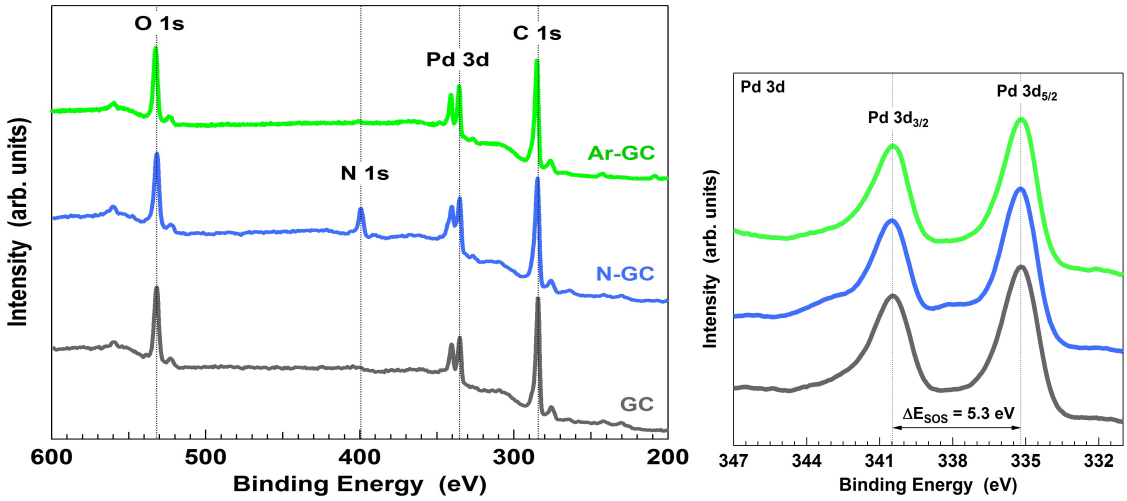

Fig. 5.12 - Wide scan XPS survey of Pd@Ar-GC, Pd@N-GC, Pd@GC (left), and amplification of the Pd 3d XPS peaks with ΔE_{SOS} = 5.3 eV (right).

In Fig. 5.13 a comparative panel for Pd@GC, Pd@Ar-GC and Pd@N-GC deposited at the same growing period of 50 s, at two different magnification scales is reported. SEM images of Pd@Ar-GC show Pd NPs with smaller sizes (centered at 25 nm) and a narrower dispersion (Fig. 5.13d–f) with respect to Pd@GC (Fig. 5.13a–c). Also in the case of Pd@Ar-GC some large size Pd agglomerates are visible, though to a lesser extent than for Pd@GC. In the case of Pd@N-GC, roughly spherical Pd NPs with average sizes of 21 nm are more regularly distributed with respect to both Pd@GC and Pd@Ar-GC (Fig. 5.13g–i).

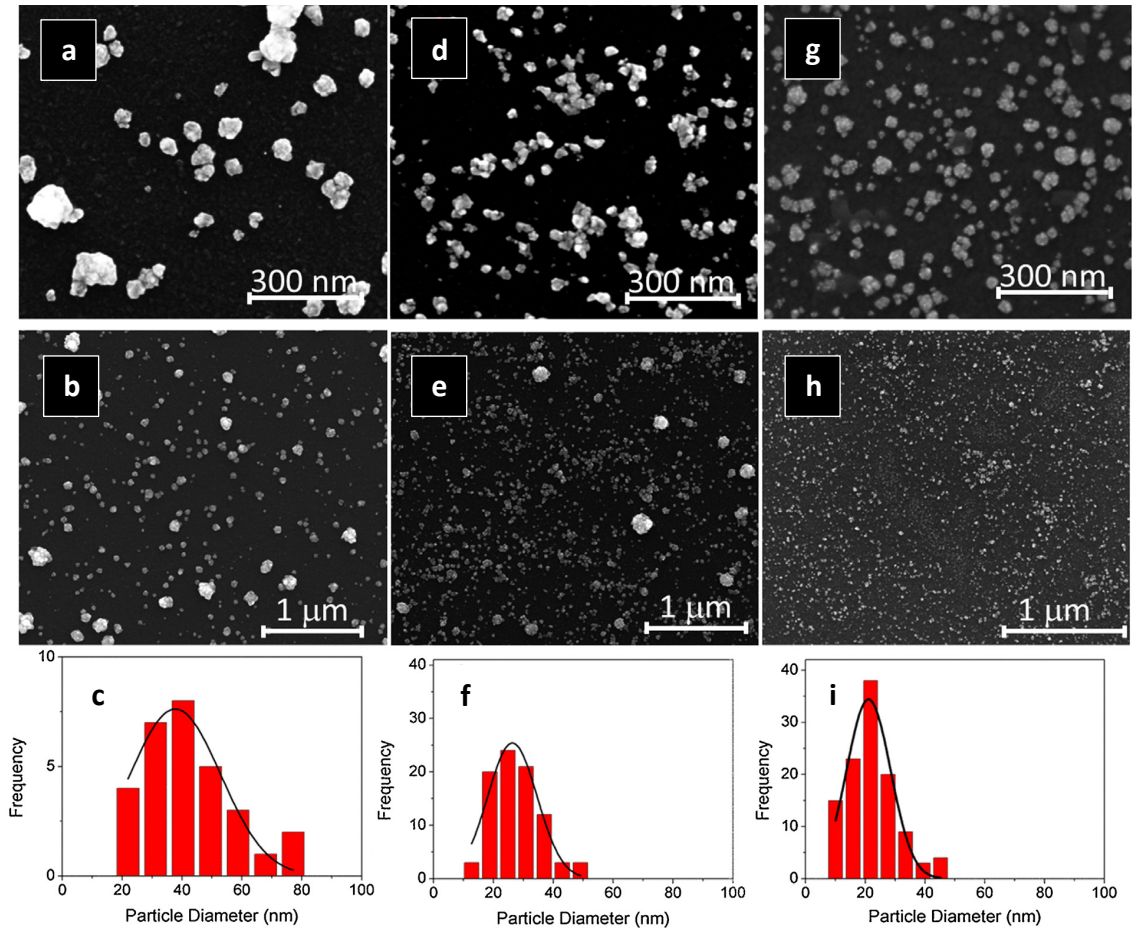

Fig. 5.13 - SEM images at two different magnifications and particle size distributions for: a-c) Pd@GC; d-f) Pd@Ar-GC and g-i) Pd@N-GC, obtained at the same Pd loading (see Table 5.5).

The surface area of the Pd NPs loaded on pristine GC (geometric area 0.076 cm^2) and modified GCs have been estimated from the integrated charge in the electrochemical formation of a full monolayer of PdO [16,17]. This method is based on the identification of the upper potential limit at which oxygen is chemisorbed in a monoatomic layer with a one to one correspondence with the surface Pd atoms. This method has been preferred over the one based on CO stripping, since the N-GC support has shown an anomalous behaviour in the presence of carbon monoxide. CVs at variable positive potential limits have been performed (Fig. 5.14a) and then the integrated charge for the formation of PdO has been plotted vs. the inversion potential (Fig. 5.14b).

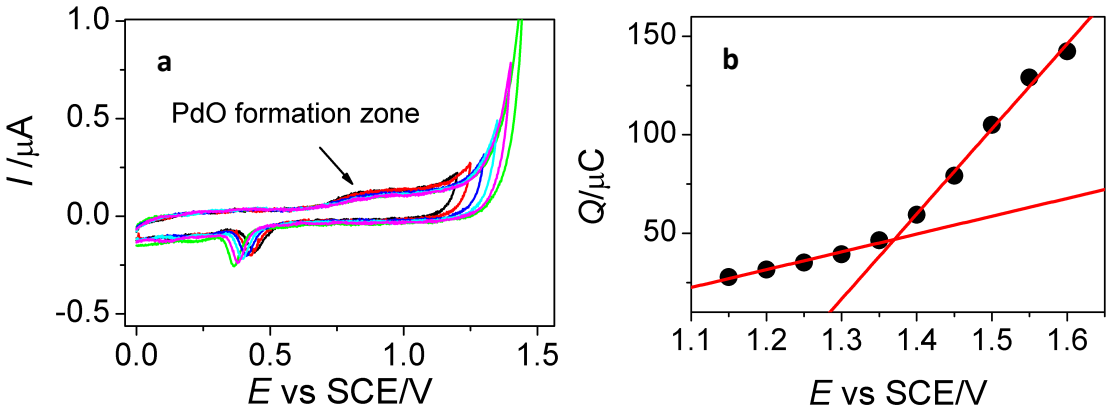

Fig. 5.14 - (a) Cyclic voltammograms at Pd@N-GC electrode in 0.1 M H_2SO_4 with different positive potential limits. (b) Integrated charge for the formation of PdO at Pd@N-GC electrode as a function of the positive potential limit.

The potential for a complete formation of a PdO monolayer corresponds to the point where the straight line changes its slope. The integrated charge at this potential allows determination of the surface area of the Pd NPs to Eq. 5.1:

$$Q_0 = 2eN_A\Gamma_0 A \qquad [5.1]$$

where N_A is the Avogadro constant and Γ_0 is the surface concentration of atomic oxygen, which corresponds to the number of Pd atoms, N_{Pd}, exposed per unit surface area. The real surface area is therefore obtained from the ratio of the integrated charge and the reference charge as indicated in Eq. 5.2:

$$A = \frac{Q_0}{q_0^s} \qquad [5.2]$$

where q_0^s is the reference charge, which is 420 C/cm^2 for Pd.

The estimated area for Pd@N-GC was 0.110 cm^2, which is higher than the area calculated for Pd@GC and Pd@Ar-GC, 0.089 and 0.085 cm^2, respectively.

In conclusion, it is evident that a mere morphological effect of the GC support is not sufficient to justify the observed significant differences in the nanostructured surfaces in terms of both surface area and metal NPs size and dispersion. Instead, these differences must be related to the presence of nitrogen functional groups, which somehow induce a much more stronger interaction between Pd and the chemical defect sites of N-doped GC [18] as compared to Ar-doped or undoped GC. A similar result has been observed for Pt NPs deposited on N-doped HOPG [19,20], where it was claimed that the N-doping is responsible for a decrease in Pt NPs size and an increase in NPs dispersion.

Very similar results were obtained furthermore when GC was doped with nitrogen through carbamic acid electrolysis.

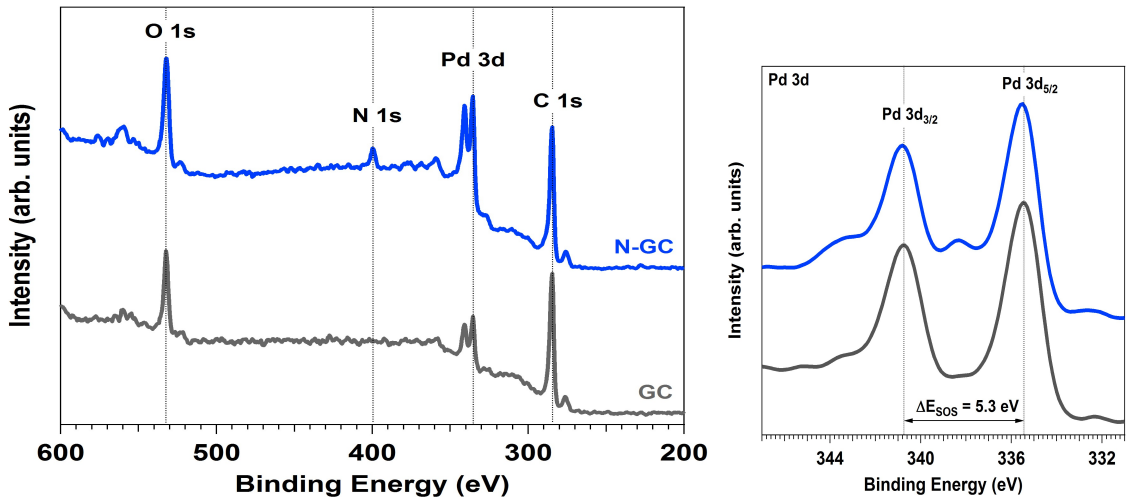

Fig. 5.15 - Wide scan XPS survey of Pd@N-GC and Pd@GC (left) and and amplification of the Pd 3d XPS peaks with ΔE_{SOS} = 5.3 eV (right).

Table 5.6 - Optimized deposition conditions for Pd NPs on GC and N-GC supports.

	E_r (V)[a,b]	t_r (s)[c]	E_n (V)[b]	t_n (s)	E_g (V)[b]	t_g (s)	Q (C)[d]
GC	0.3	10	-0.25	0.1	-0.077	50	4.10E-4
N-GC	0.3	10	-0.25	0.1	-0.127	50	4.35E-4

[a] Rest potential. [b] Potentials are versus SCE. [c] Rest time. [d] Values obtained from the mean of at least 5 different experiments.

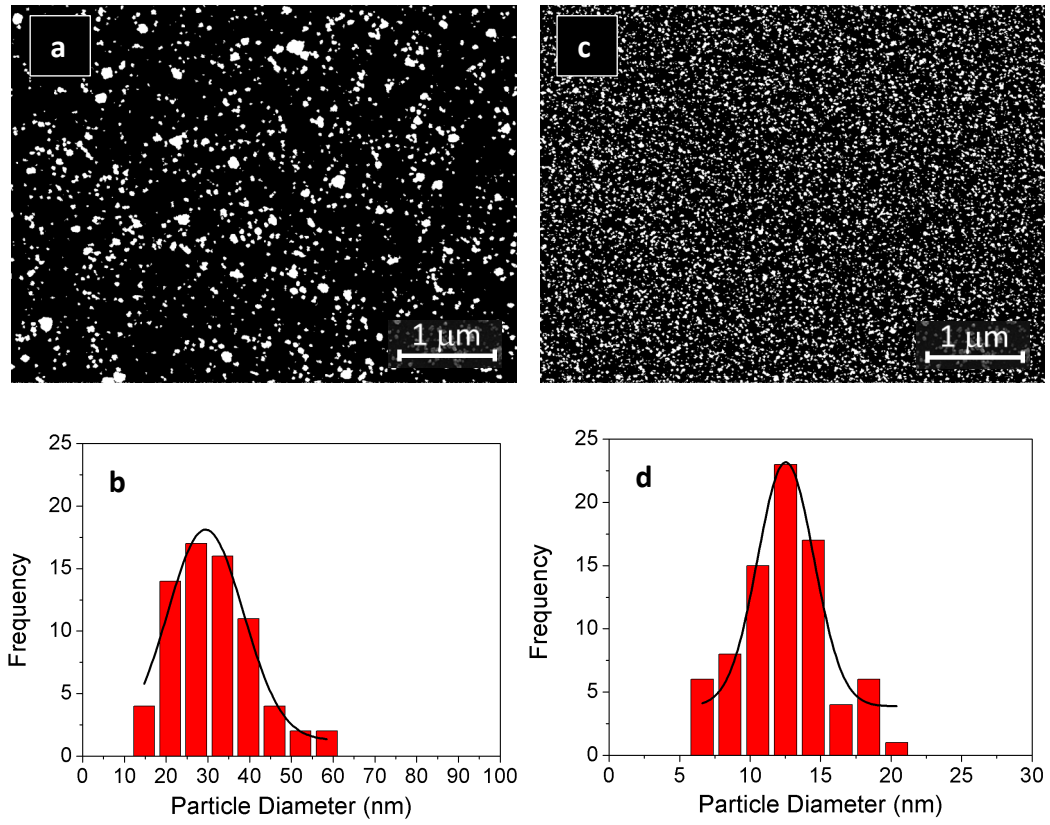

Fig. 5.16 - SEM images and particle size distributions for (a and b) Pd@GC and (c and d) Pd@N-GC, obtained at the same Pd loading (see Table 5.6).

For both samples, also in this case, a comparable amount of charge is consumed and therefore the mass of Pd loaded over the two different GCs is fairly similar.

SEM images of Pd@GC, obtained at the same growing time of 50 s as in the case of Pd@N-GC, show Pd NPs with sizes centered at 30 nm (Fig. 5.16a–b). In the case of Pd@N-GC, roughly spherical Pd NPs with smaller sizes of 12.5 nm and narrower dispersion are more regularly distributed with respect to Pd@GC (Fig. 5.16c–d).

5.6 Electrocatalytic activity

5.6.1 Activity of N-GC obtained by ion implantation

The reduction mechanism of BnCl on bulk Pd and GC has previously been reported [11], showing that, on both electrodes, the reduction of benzyl chloride follows a concerted mechanism that is typically characterized by an ET coefficient $\alpha << 0.5$. Figure 5.17b shows CV of BnCl reduction at Pd@GC electrodes at different Pd deposition times. From Fig. 5.17b it is clear that the overpotential for BnCl reduction depends on the Pd surface coverage since, as the deposition time of Pd increases from 25 to 150 s, the reduction peak shifts to a more positive potential and the peak current increases. The Pd@GC electrode obtained at a deposition time of 150 s (E_p = –1.87 V *vs.* SCE), shows an electrocatalytic activity comparable to that of bulk Pd (E_p = –1.88 V *vs.* SCE). Therefore, it appears that the catalytic activity of Pd deposited on a non-modified GC depends more on the Pd loading and nanoparticles size than on the morphology of the metal catalyst.

The electrochemical behaviour of Pd@Ar-GC (t_g = 50 s) is also reported in Fig. 5.17c. As previously discussed, Pd NPs on Ar-GC are smaller and more uniformly dispersed than on pristine GC; however, besides a little difference of peak current, which may be associated to a different active surface area, Pd@Ar-GC shows similar catalytic activity and reduction mechanism as those of Pd@GC (Table 5.7). These results point out that the catalytic activity is not influenced by the morphology of the samples. In fact, even though Ar-GC has an increased number of defects with respect to pristine GC and the average size of the Pd NPs is sensibly different for the two GCs, the two electrodes show similar behaviour. Furthermore, it must be stressed that in terms of catalytic activity both Pd@GC and Pd@Ar-GC do not show better performance than bulk Pd. However, considering the benefit of employing a small amount of catalyst, there could be a practical advantage in using nanostructured electrodes with respect to bulk metal.

The electrochemical behaviour of BnCl was tested also at Pd@N-GC (t_g = 50 s) (Fig. 5.17c), and, interestingly this time, the nanostructured surface was found to be more active in terms of overpotential, mass catalytic activity (M-CA, peak

current/grams of Pd) and specific catalytic activity (S-CA, peak current/surface area) with respect to not only Pd@GC or Pd@Ar-GC, but also bulk Pd (Table 5.7).

The integrated current for the deposition process indicates that the Pd amount loaded on N-GC is comparable to that on Ar-GC; thus, the improved catalytic activity is not the result of different Pd loading or particle size on the three supports.

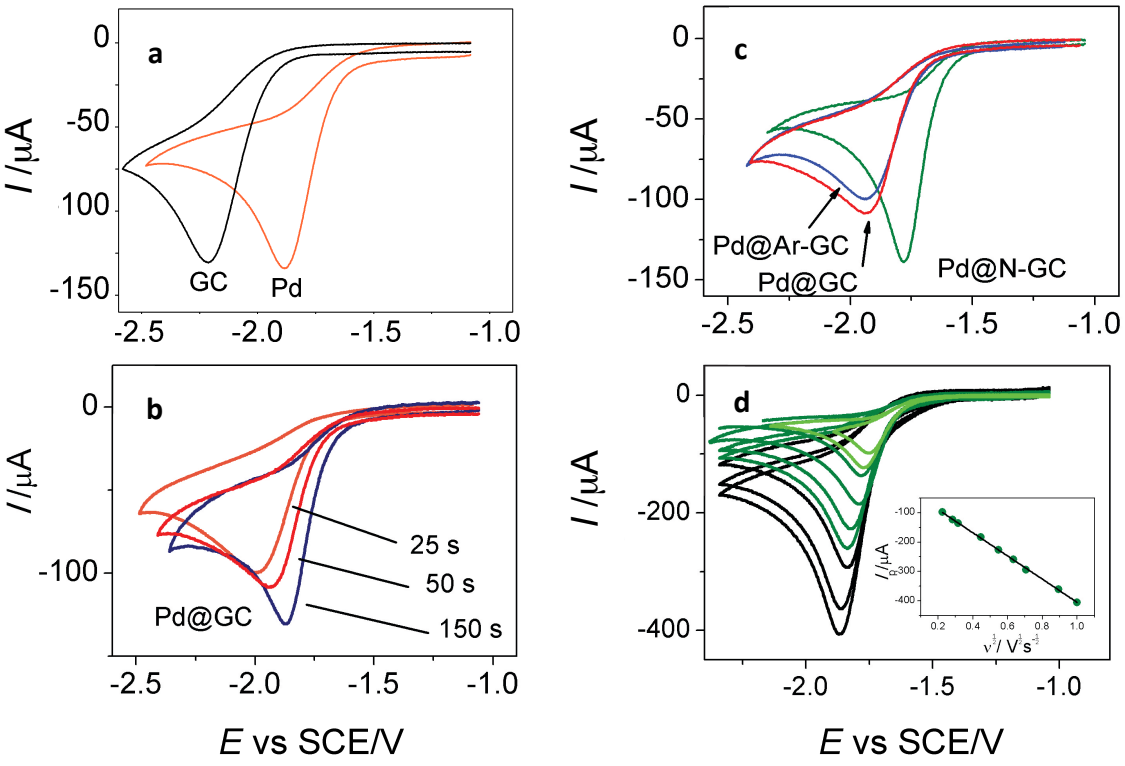

Fig. 5.17 - Cyclic voltammograms of 2 mM BnCl recorded in CH_3CN + 0.1 M $TEABF_4$ at different electrodes: (a) GC and bulk Pd; (b) Pd@GC at different Pd loadings; (c) Pd@N-GC, Pd@Ar-GC and Pd@GC; (d) effect of the scan rate at Pd@N-GC.

This represents a clear example where the electrodic support exerts a synergistic action, promoting the catalytic activity of metal NPs toward a catalytic process. The origin of this increased catalytic activity is to be traced back to the interaction between nitrogen functional groups and Pd NPs during the reduction process, since Pd-free N-GC was found to be inactive by itself. Actually, both N-GC and Ar-GC supports are less active than pristine GC by at least 300 mV. To verify that the increased catalytic activity is not the result of a different reduction mechanism, we have evaluated the dependence

of the voltammetric peak from the scan rate (Fig. 5.17d). The linear dependence of I_p on the square root of the scan rate indicates a diffusion-controlled process, while $\alpha = 0.33$ suggests a concerted reduction mechanism, as already observed at Pd@GC and bulk Pd. Furthermore, Pd@N-GC does not lose its catalytic activity even after exposure to the open laboratory atmosphere for several days, indicating an intrinsic chemical and mechanical stability. This was confirmed also by *post eventum* XPS measurements, showing full preservation of both Pd and N contents.

Table 5.7 - Voltammetric data for BnCl reduction (2 mM) in CH_3CN + 0.1 M $TEABF_4$, measured at 0.1 V s^{-1}.

Electrode	E_p[a] (V)	α	ΔE_p[b] (V)	A (cm^2)	M-CA[c] (mA g^{-1})	S-CA[d] (mA cm^{-2})
GC	-2.21	0.30	--	0.071[e]	--	--
Pd	-1.88	0.26	0.33	0.031[e]	--	1.262
Pd@GC	-1.93	0.19	0.28	0.089[f]	7.2E+05	1.217
Pd@Ar-GC	-1.93	0.23	0.28	0.085[f]	6.6E+05	1.156
Pd@N-GC	-1.78	0.33	0.43	0.110[f]	9.0E+05	1.269

[a] Potentials are referred to SCE, [b] $\Delta E_p = E_p^{Pd} - E_p^{GC}$, [c] Mass catalytic activity with respect to the mass of Pd electrodeposited (Eq. 3.8), [d] Specific catalytic activity (Eq. 3.7), [e] Geometric area, [f] Real surface area.

5.6.2 Activity of N-GC obtained by carbamate electrolysis

Similar considerations, as just seen above, can be made for the N-doped GC obtained by carbamate electrolysis. Cyclic voltammetry of BnCl on this electrode shows that $\alpha << 0.5$, confirming the same concerted dissociative electron transfer mechanism found on all other electrodes.

The integrated current for the deposition process still indicates that the Pd amount loaded on N-GC is comparable to that at GC; however, it is possible to observe that after electrodeposition of Pd NPs, the particle size significantly differs between the two types of N-GC (carbamate electrolysis vs. ion implantation).. In particular, when GC is doped with the electrochemical method, the particle size distribution is centered

at 12.5 nm. This further decrease of the size can be related with the different ratio of functional groups given by these two procedures, or even with the presence of a new one, such as the ammine group.

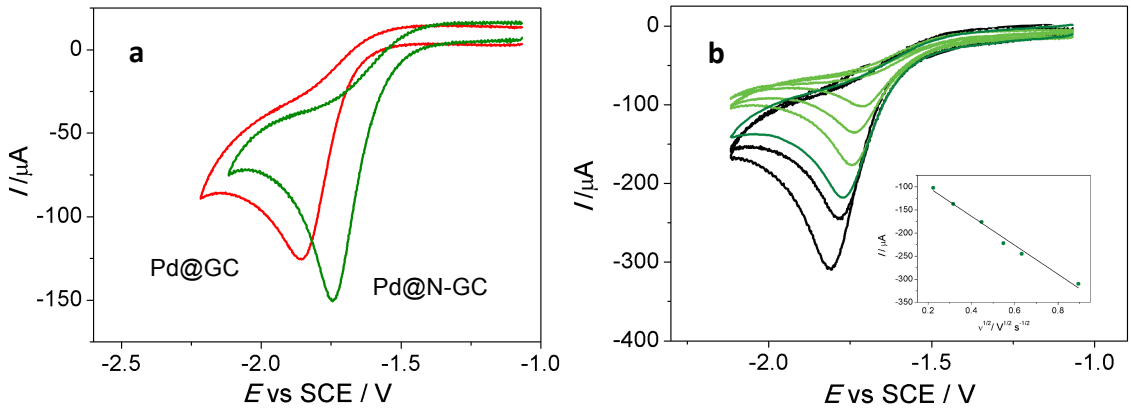

Fig. 5.18 - Cyclic voltammograms of 2 mM BnCl recorded in CH_3CN + 0.1 M $TEABF_4$ at different electrodes: (a) Pd@N-GC and Pd@GC; (b) effect of the scan rate at Pd@N-GC.

Finally, the electrochemical behaviour was tested at Pd@N-GC (t_g = 50 s) (Fig. 5.18a), and, again, Pd@N-GC was found to be more active in terms of overpotential with respect to both Pd@GC and to bulk Pd (Table 5.8).

Table 5.8 - Voltammetric data for BnCl reduction (2 mM) in CH_3CN + 0.1 M $TEABF_4$, measured at 0.1 V s^{-1}.

Electrodes	E_p^a (V)	α	ΔE_p^b (V)
GC	-2.21	0.30	--
Pd	-1.82	0.19	0.39
Pd@GC	-1.86	0.25	0.35
Pd@N-GC	-1.74	0.10	0.50

[a] Potentials are referred to SCE, [b] $\Delta E_p = E_p^{Pd} - E_p^{GC}$.

Further experiments are going on to determinate the real surface area of palladium nanoparticles and to calculate the *M-CA* and *S-CA*.

Compared with other catalysts reported in the literature, that are well-known to possess high catalytic activity, such as Ag, both Pd@N-GC electrodes prepared in this work show comparable catalytic activity with respect to bulk Ag, which so far is considered the best catalyst for R-X activation in non-aqueous solution [11].

Bibliography

[1] Pocard, N.L.; Alsmeyer, D.C.; McCreery, R.L.; Neenan, T.X.; Callstrom, M. R. *J. Mater. Chem.* **1992**, *2*, 771-784.

[2] Pylypenko, S.; Queen, A.; Olson, T.S.; Dameron, A.; O'Neill, K.; Neyerlin, K.C.; Pivovar, B.; Dinh, H.N.; Ginley, D.S.; Gennett, T.; O'Hayre, R. *J. Phys. Chem. C* **2011**, *115*, 13667-13675.

[3] Pylypenko, S.; Queen, A.; Olson, T.S.; Dameron, A.; O'Neill, K.; Neyerlin, K.C.; Pivovar, B.; Dinh, H.N.; Ginley, D.S.; Gennett, T.; O'Hayre, R. *J. Phys. Chem. C* **2011**, *115*, 13676-13684.

[4] Minguzzi, A.; Lugaresi, O.; Aricci, G.; Rondinini, S.; Vertova, A. *Electrochem. Commun.* **2012**, *22*, 25-28.

[5] Neenan, T.X.; Callstrom, M.R.; Bachman, B.J.; McCreery, R.L.; Alsmeyerb, D.C. *Brit. Polym. J.* **1990**, *23*, 171-177.

[6] Perić-Grujić, A.A.; Nešković, O.M.; Veljković, M.V.; Laušević, Z.V.; Laušević, M.D. *Bull. Mater. Sci.* **2007**, *30*, 587-593.

[7] Uchiyama, S.; Watanabe, H.; Kanazawa, A.; Hamana, H.; Okabe, Y. *J. Electrochem. Soc.* **2007**, *154*, 31-35.

[8] Fang, Y.; Al-Abed, S.R. *Appl. Catal. B: Environ.* **2008**, *80*, 327-334.

[9] Sun, Z.; Wei, X.; Hu, X.; Wang, K.; Shen, H.; Colloids Surf., A **2012**, *414*, 314-319.

[10] Chen, S.; Qin, Z.; Quan, X.; Zhang, Y.; Zhao, H. *Chinese Sci. Bull.* **2010**, *55*, 358-364.

[11] Isse, A.A.; Gottardello, S.; Durante, C.; Gennaro, A. *Phys. Chem. Chem. Phys.* **2008**, *10*, 2409-2416.

[12] Favaro, M.; Perini, L.; Agnoli, S.; Durante, C.; Granozzi, G.; Gennaro, A. *Electrochim. Acta* **2013**, *88*, 477-487.

[13] Favaro, M.; Agnoli, S.; Perini, L.; Durante, C.; Gennaro, A.; Granozzi, G. *Phys. Chem. Chem. Phys.* **2013**, *15*, 2923-2931.

[14] Diculescu, V. C.; Chiorcea-Paquim, A.M.; Corduneanu, O.; Oliveira-Brett, A.M. *J. Solid State Electrochem.* **2007**, *11*, 887-898.

[15] Guerin, S.; Attard, G.S. *Electrochem. Commun.* **2001**, *3*, 544-548.

[16] Correia, A.N.; Mascara, L.H.; Machado, S.A.S.; Avaca, L.A. *Electrochim. Acta* **1997**, *42*, 493-495.

[17] Fang, L.L.; Tao, Q.; Li, M.F.; Liao, L.W.; Chen, D.; Chen, Y.X. *Chinese J. Chem. Phys.* **2010**, *23*, 543-548.

[18] Zhou, Y.; Pasquarelli, R.; Holme, T.; Berry, J.; Ginley, D.; O'Hayre, R. *J. Mater. Chem.* **2009**, *19*, 7830-7838.

[19] Zhou, Y.; Holme, T.; Berry, J.; Ohno, T.R.; Ginley, D.; O'Hayre, R.; *J. Phys. Chem. C* **2010**, *114*, 506-515.

[20] Zhou, Y.; Neyerlin, K.; Olson, T.S.; Pylypenko, S.; Bult, J.; Dinh, H.N.; Gennett, T.; Shao, Z.; O'Hayre, R. *Energy Environ. Sci.* **2010**, *3*, 1437-1446.

MESOPOROUS CARBON

In recent years, there has been a growing interest in the synthesis of Mesoporous Carbon (MC) materials with well-controlled and well-defined morphologies and nanostructures [1-5] because of their remarkable properties. Their large surface area (>1000 m^2 g^{-1}), tunable pore structure, uniform and adjustable pore size, chemically inert nature, mechanical stability, good conductivity and electrochemical performances superior to traditional carbon materials are key features for their possible use. The success of these materials relies on the tremendous applications they find as gas sequestering materials (CO, CO_2, NO_2, H_2S, VOCs, etc.), in heterogeneous catalysis (hydrogenation, oxidation, etc), in sensing and, most of all, as catalyst supports in electrocatalysis [6].

The nature of the support has a strong influence on some important properties of the catalyst, such as dispersion of the active phase, inhibition of sintering and loss of the catalyst during operation [7,8], morphology of the metallic crystallites [9] and electrochemically active area [10,11].

Carbon blacks (CBs) are widely used as supports for gas diffusion electrodes in electrochemical devices, since they generally possess a pore structure that allows the filling with electrolyte bringing the catalyst particles close to the reactants, thus maximizing the three-phase interface. There are several types of CBs, like Acetylene Black, Vulcan XC-72R, Ketjen Black, each one showing different physical and chemical properties, such as specific surface area, porosity, electrical conductivity, and surface functionality. Among these properties, specific surface area has a significant effect on the preparation and performance of supported catalysts. Generally, highly dispersed, supported catalysts cannot be prepared from low surface area CBs such as Acetylene Black. Ketjen Black possesses high surface and in principle should be appropriate as a dispersed catalyst support; however, it shows high ohmic resistance and mass transport limitations during fuel cell operation. Vulcan XC-72R, with a surface area of ca. 250 m^2 g^{-1}, has been commonly used as a catalyst support, especially in direct methanol FC anode catalyst preparation. Still, Vulcan has a preponderance of small pores, below 2 nm, that cannot be filled with electrolyte molecules. The result is

that surface area inside the micropores has less or even no electrochemical activity, due to the difficulty in reactant accessibility. Actually, the optimal pore size range is between 2–50 nm (Fig. 6.1).

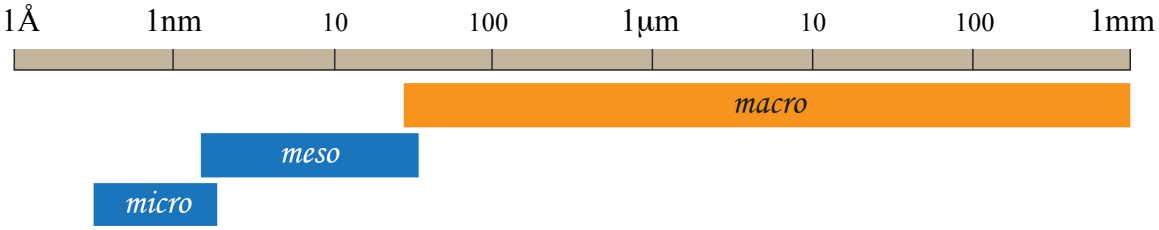

Fig. 6.1 - Pore size ranges of porous materials.

It is therefore convenient to have a classification of pores according to size. Pores with widths less than about 2 nm are termed *micropores*, whereas pores with widths greater than 100 nm are referred to as *macropores.* Pores with intermediate size are called *mesopores.* It has to be noticed that usually, in active carbons, the surface area (between 400 and 1000 m^2 g^{-1}) mainly originates from micropores, while the contribution of macropores in the same specimens is only in the order of few m^2 g^{-1}, although the two types of pores have similar volumes in the range from 0.15 cm^3 to 0.5 cm^3.

6.1 Synthesis of MC

Since zeolites and mesoporous silicas possess ordered and uniform pores, they are used in various fields as catalysts, catalyst supports, and separation media equipped with a molecular sieving function [12]. Their inherent electrical insulative nature, however, does not allow their application to the electrochemical field. To overcome this problem, new ordered porous materials composed of conductive substances, such as metals and/or carbon, have been recently developed [13–21]. Such materials can be classified into two groups. The first group is the materials that are synthesized by using zeolites or mesoporous silicas as hard templates [15–17]. The resulting ordered porous

materials are negative replicas of their parent templates, and therefore, they never have the same structure as the original templates. The second group is the conductive materials that are synthesized by using the soft template method through an organic-organic self-assembly process or block copolymers as templates [13,14,19–22]. With this direct synthetic pathway, it is possible to construct conductive materials with ordered structures, which are similar to those of the mesoporous silicas. Generally, the soft template method is more convenient than the hard template one, although sometimes it is more expensive in terms of reagent usage. Moreover, their structure variety is more or less limited and their structure regularity (pore structure and diameter) is not so high compared with the mesoporous silicas.

The solid template method is mainly employed to synthesize mesoporous carbons because it allows control of the pore structure and morphology of the resulting carbon materials due to the use of mesoporous templates. The synthesis of mesoporous carbons via solid templates is based on the pyrolysis of carbon precursors within the pore channels of mesoporous silica or aluminosilicate templates, followed by the removal of the inorganic templates.

There are two strategies by which carbon precursors may be introduced into the pore channels of mesoporous template: liquid impregnation and chemical vapor deposition (CVD). The liquid impregnation method involves incorporation of a carbon precursor (such as sucrose [23], furfuryl alcohol [24], phenol resin [25], or acetylene [26]) through a solution phase into mesoporous silica hosts, followed by the pyrolysis of the carbon precursor. After the removal of the mesoporous solid template, mesoporous carbon materials with different mesostructural morphologies replicated from various kinds of mesoporous templates can be obtained [27,28]. Another synthetic route widely described is the chemical vapor deposition (CVD). The most important advantage of the CVD method is that various modified carbon materials (e.g., nitrogen doped) can be easily prepared by using an inert gas (N_2 or Ar) as a carrier gas to transport NH_3 or CH_3CN and the carbon precursor [27,29].

Although widely used, chemical vapour deposition and liquid impregnation, as they are, present advantages as well as setbacks. For example, liquid impregnation does not allow a subsequent modification or doping of the carbon material, once it has been prepared. Therefore, for studying a doped carbon material the only standards that can be

used as reference need to be commercial ones. As to the CVD methodology, although it is flexible for the possible combinations of precursor and doping agent as starting materials, it requires both to be in a gas phase, which is fairly more complex than impregnation in terms of equipment and costs.

For these reasons we decided to exploit the benefits of both methodologies. Synthesis of undoped mesoporous carbon was carried out by liquid impregnation, while doping was later performed by an adjusted vapour deposition, fruitfully taking advantage of the simplicity of these two steps and allowing referencing with a real internal standard, represented by the undoped material.

Mesoporous Carbon was prepared by a hard template method using Mesoporous Silica (MS) (Sigma-Aldrich) as scaffold, following the scheme reported in Fig 6.2. Sucrose (1 g) and H_2SO_4 (0.12 g) were mixed with the MS template (1 g) in water (5 mL). The mixture was dried in an oven at 100 °C for 6 h and then the temperature was increased to 160 °C over night. During this pre-treatment step at 100 °C, the carbonization started and the colour of the sample turned from white to brown. Then, the powder was heated in a quartz tube, raising the temperature from 25 to 900 °C and maintaining it at this value for 4 h under Argon flow (200 sccm). At the end, the temperature was cooled down and the silica content was dissolved with a solution (50% v|v) of NaOH (1 M) and EtOH, for 24 h under vigorous stirring. Before being collected, the carbon powder was filtered and washed several times with doubly distilled water.

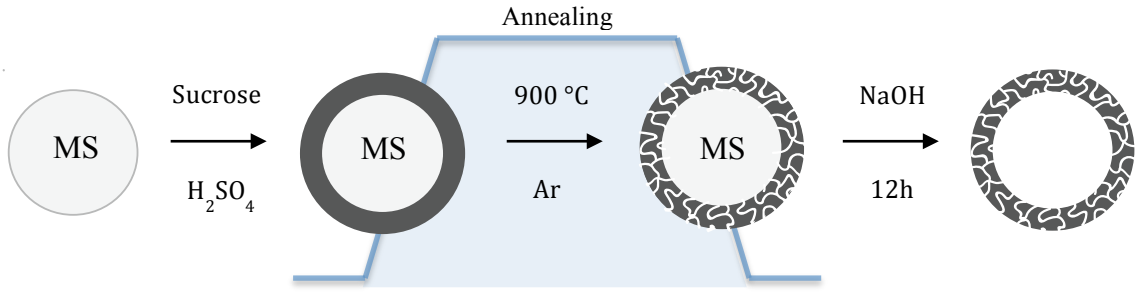

Fig. 6.2 - Scheme of synthesis of Mesoporous Carbon.

Based on what was previously reported in the literature, an optimization of the annealing process was performed by changing the heating rate of the pyrolysis from 2 to 20 °C min^{-1}; in particular, the rates used were: 2, 5, 10, 20 °C min^{-1}.

It is well known that below 800 °C the carbon matrix does not undergo a complete carbonization; the material obtained with this temperature presents a small surface area and thus a poor number of pores. Changing the temperature of annealing from 900 to 1100 °C causes a major re-hybridization of the carbon matrix, from sp^3 to sp^2; overall, the higher the temperature, the higher the sp^2 hybridization degree of the sample obtained.

Several studies have been reported on the effect of the maximum temperature reached during the annealing process and the optimal temperature range has been shown to be between 850 and 950 °C [30]. Thus, since a comprehensive analysis on the subject has never been reported, our attention was focused on studying the effect that a change in the heating rate could have on the final structuring of the material.

BET analysis on the four samples obtained revealed that varying the heating rate from 2 °C min^{-1} to a 20 °C min^{-1} resulted in a 20% loss of surface area, while the dimensions of meso- and micro-pores remained virtually unchanged as shown in Fig. 6.3 and reported in Table 6.1.

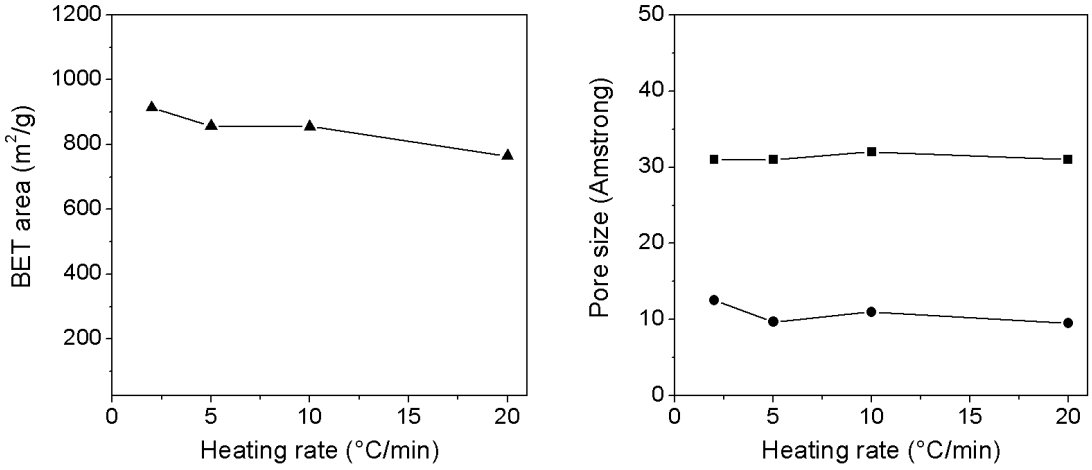

Fig. 6.3 - Correlation between BET surface area (left) or meso- and micro-pore size (right) with the heating rate.

We therefore chose to proceed with the doping step, using samples prepared with the synthetic conditions that could ultimately generate mesoporous carbons with the highest surface area.

6.2 Synthesis of N-MC

In the past few decades, considerable efforts have been devoted in R&D to fuel cell-related areas, though two major challenges remain to be resolved for future practical applications of PEMFCs, namely their costs and durability [31]. It has been recognized that Pt is by far the most active among catalysts for the oxygen reduction reaction (ORR) and the progressive increase in prices of this metal, coupled with the limited reserve of noble metals in general [32], surely is one of the greatest obstacles for commercialization and utilization of PEMFCs. For these reasons, one of the most important lines of the current research on fuel cells aims at further decreasing the amount of Pt in the electrocatalysts, while increasing their specific mass activities. Thus, catalyst support materials with appropriate textural and electrochemical properties, e.g., high surface areas and good electrical conductivities, are highly desirable as they would be helpful for metal NPs dispersion, thus enhancing the kinetics of reactions occurring at both the anode and the cathode [33].

Therefore, taking into account the properties discussed above, nanostructured carbon materials appear to represent ideal supports for metal-based electrocatalysts. Indeed, aside from the most common and commercially available Vulcan XC-72 activated carbons, carbon nanotubes (CNTs), carbon nanofibers (CNFs), and, particularly, mesoporous carbons (MCs) have been suggested to be appropriate supports for electrocatalysts that can be used as both anodes and cathodes in PEMFCs. Nevertheless, due to their chemically inert nature, the majority of nanostructured carbon materials normally lack desirable functional groups at their surfaces, making the supported metal NPs more vulnerable for aggregation and deactivation during electrocatalytic reactions. To circumvent these problems, the incorporation of heteroatoms (e.g., N, B, and S) onto the carbon supports aimed to modify their surface and physicochemical properties is currently under intensive investigation.

Nitrogen-doped mesoporous carbons (N-MC), are a kind of fascinating materials that have recently attracted worldwide attention [34]. They promise access to a wide range of applications and possess great potential for fuel cell catalyst employment, especially regarding the ORR, because the nitrogen atoms in the carbon architecture can enhance chemical, electrical and functional properties [35]. Among different doping agents, N-containing carbons have received considerable attention due to several reasons.

On a general note, the introduction of functional groups into carbon materials provides an increased pseudocapacitance to the material, that is an improved capacitance of the carbon-based electrodes [36] (Fig. 6.4), which is due to an increase of the adsorption capability of the electrolyte ions in the electrical double layer [37]. Specifically for nitrogen doping, its strong electron donor nature promotes reinforcement in π bonding, enhancing wettability of the material at the electrode/electrolyte interface. This process leads to an improved stability, enhanced electron transfer rate and hence an increased durability of the carbon supports during electrocatalysis [38]. On the other hand, the presence of N should also enhance the affinity between metal NPs and the carbon atoms, easing nucleation sites formation and promoting a high NPs dispersion on the surfaces of the supports [39,40].

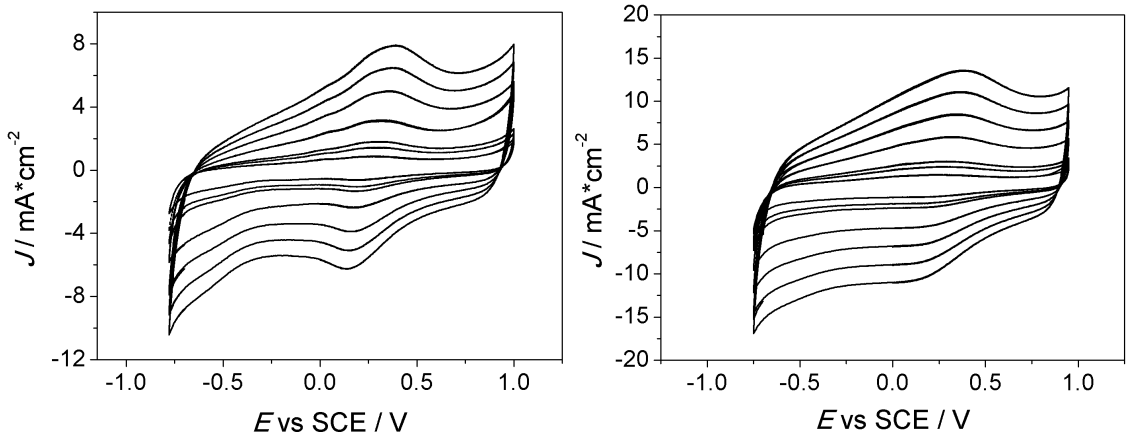

Fig. 6.4 - Cyclic voltammetry of MC (left) and N-MC (right) at different scan rates in H_2SO_4 0.1 M; the current density scales are different.

The procedure used for the synthesis of N-MC, as shown Fig. 6.5, was quite similar to the synthesis described previously for MC. In this case, after the thermal pre-treatment, the temperature was not increased directly to 900 °C, but a new step at 300 °C for 4 h under flow of pure ammonia (NH_3) at 400 sccm was introduced.

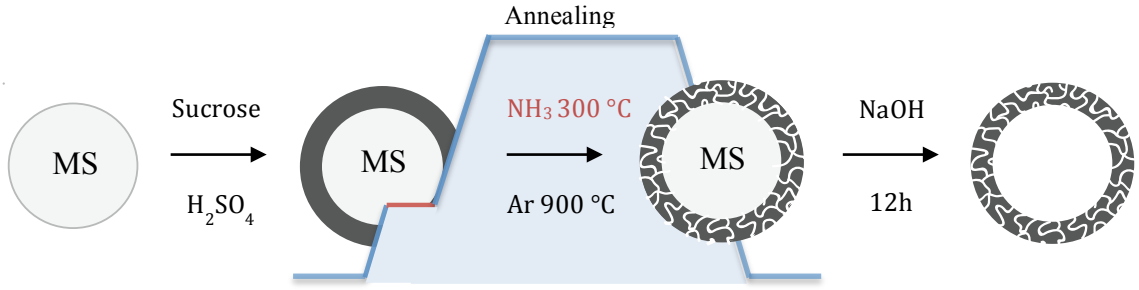

Fig. 6.5 - Scheme of synthesis of N-doped Mesoporous Carbon.

The nitrogen amount was determined by XPS technique, by normalizing the intensity of the N 1s peak for the integrated area of the C 1s photoemission peak (both corrected for the differential cross-section and the mean free path), obtaining a 5.7 at% nitrogen dose. The quantity of nitrogen introduced is in full agreement with the higher range previously reported for nitrogen doping of mesoporous carbon [29,41,42]. Some syntheses were carried out extending the ammonia exposure time from 4 to 8 hours, hoping to increase the nitrogen dose in the sample; however, the results did not show any accountable increase (Fig. 6.6).

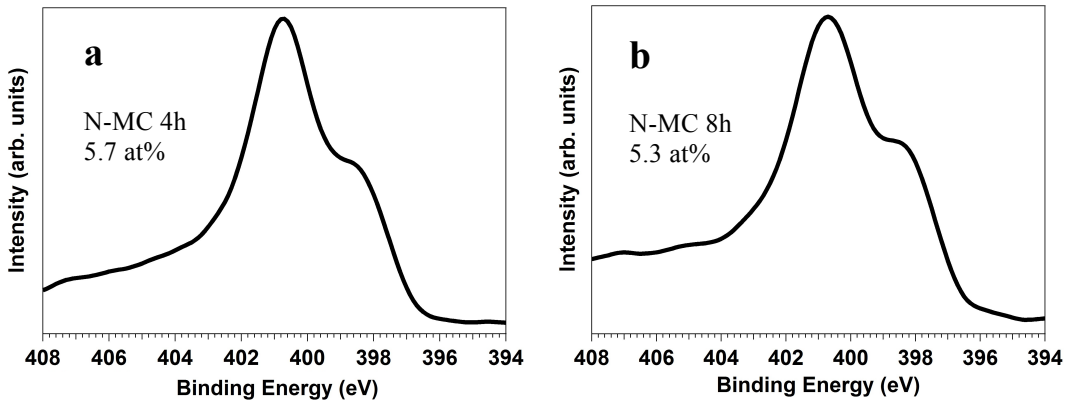

Fig. 6.6 - N1s XPS peak of N-MC at different ammonia exposure time (a) 4h, (b) 8h.

6.3 Physical characterization

The specific surface areas of the samples were calculated by a multipoint Brunauer-Emmett-Teller (BET) analysis of the nitrogen adsorption/desorption isotherms, whereas the pore size distribution curves were derived from the Barrett-Joyner-Halenda method (for mesopores) and Horvath-Kawazoe method (for micropores), by using the adsorption/desorption branches. Figure 6.7 shows for each one of the samples, obtained at different heating rate, the same type-IV (IUPAC) isotherm characteristic of materials with a mesoporous structure.

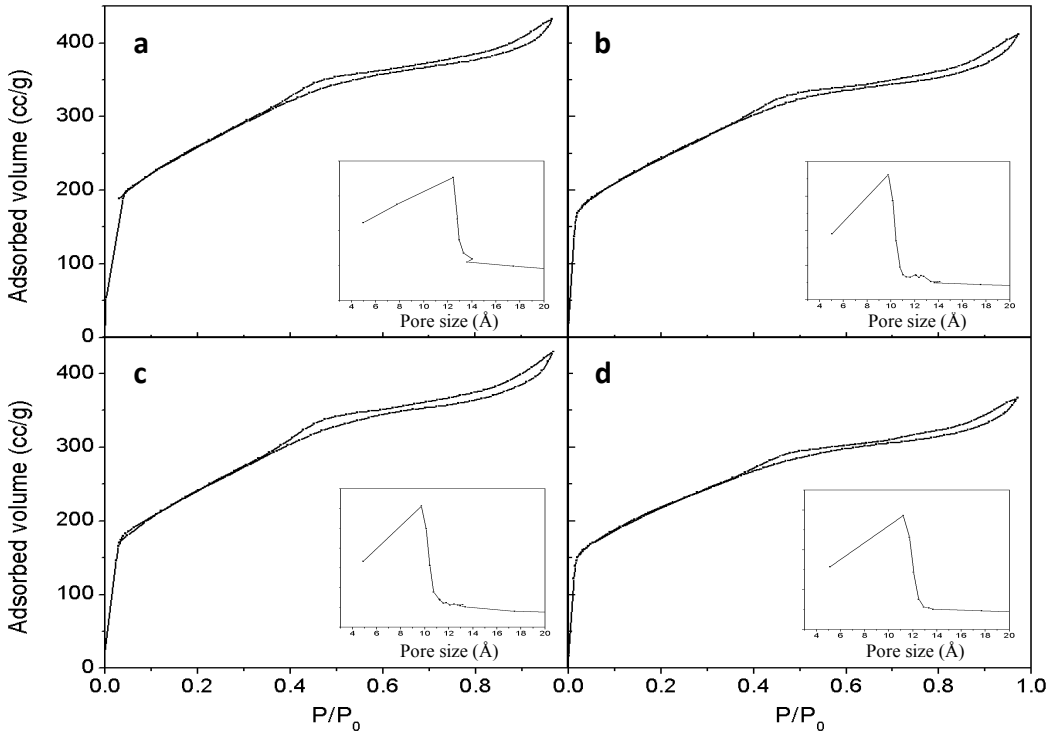

Fig. 6.7 - Nitrogen adsorption isotherms and the H-K pore-size distributions (insets) of (a) MC 2 °C min^{-1}, (b) MC 5 °C min^{-1}, (c) MC 10 °C min^{-1} and (d) MC 20 °C min^{-1}.

While the specific surface area (Table 6.1) decreases from 914 to 765 m^2 g^{-1} with the increase of heating rate from 2 to 20 °C min^{-1}, the average pore diameter of mesopores and micropores is constant with a value around 3 and 1 nm, respectively. This means that the number of pores is the parameter varying with the heating rate variation: at low heating rate the number of pores results to be higher than the one

obtained under higher heating rates. It is therefore wise to synthesis MCs at a low heating rate.

Table 6.1 - BET surface area and pore structure parameters of different MCs and N-MCs.

sample	BET surface area (m^2/g)	Pore volume (cm^3/g)	BJH pore size (nm)	H-K pore size (nm)
MC 2 [a]	914	0.30	3.1	1.2
MC 5 [a]	857	0.31	3.1	0.9
MC 10 [a]	856	0.31	3.2	1.1
MC 20 [a]	765	0.27	3.1	1.0
NMC 2 [a]	608	0.29	3.0	0.9

[a] The numbers 2, 5, 10, 20 indicate the heating rate (°C min^{-1}) used.

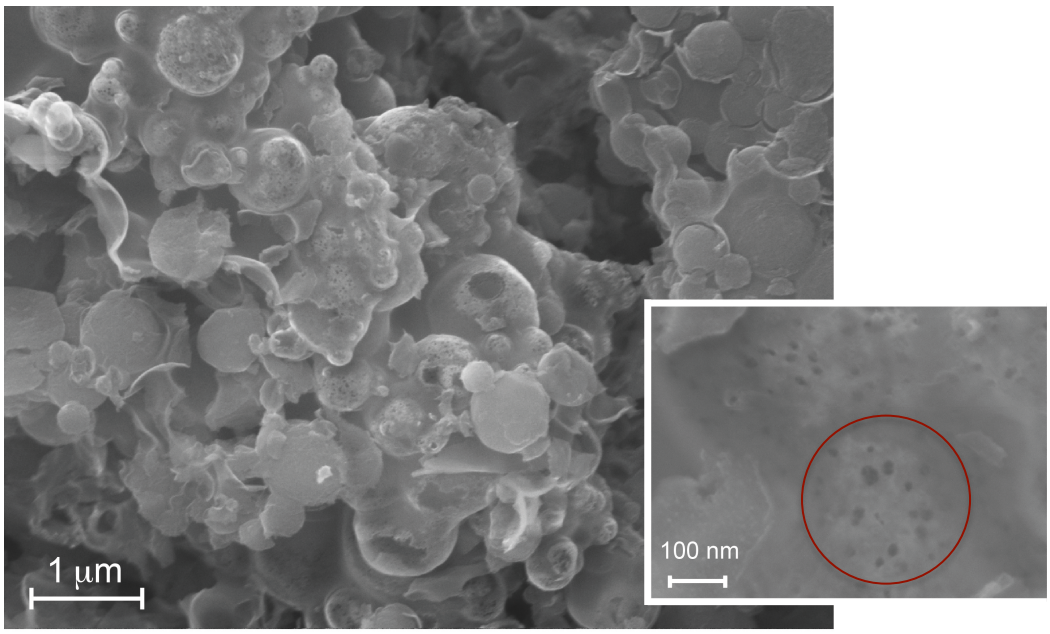

Fig. 6.8 - SEM images of MC 2 with different magnifications, circled in red are the macropores of the structure.

N-MC was then synthesized by using only the lowest heating rate (2 °C min^{-1}); also in this case an isotherm type-IV (IUPAC) and meso- and micropores of similar size as those of MC samples (Fig. 6.9) were obtained. The BET analysis of the doped and

undoped samples, obtained with a 2 °C min^{-1} heating rate, showed that the surface area of the doped material is 2/3 that of the undoped MC. This is caused by the presence of nitrogen on the sample, partially filling the pores and thus covering the surface area of the carbon matrix.

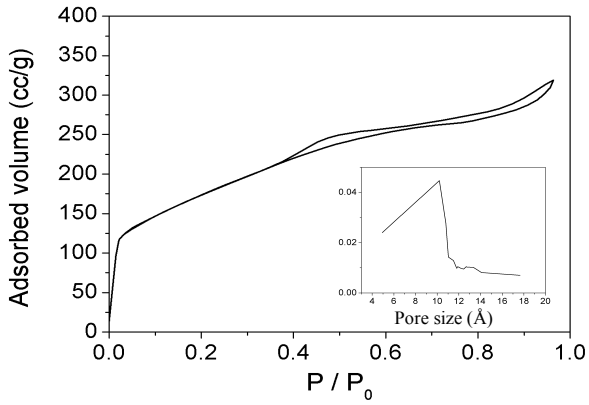

Fig. 6.9 - Nitrogen adsorption isotherm and H-K pore-size distribution (inset) of N-MC.

In order to gain a deep understanding of the chemistry of the studied systems, we carried out an accurate XPS investigation. Figure 6.10 reports the wide range measurements acquired for MC and N-MC samples (Fig. 6.10a and 6.10b, respectively). As can be clearly seen, both spectra exhibit the photoionization peak of C 1s (284.6 eV) as the main feature, thought the presence of an important amount of oxygen is also well evident. Furthermore, XPS reveals traces of contamination from the templating silica and from the solution of concentrated NaOH used to dissolve the templating agent.

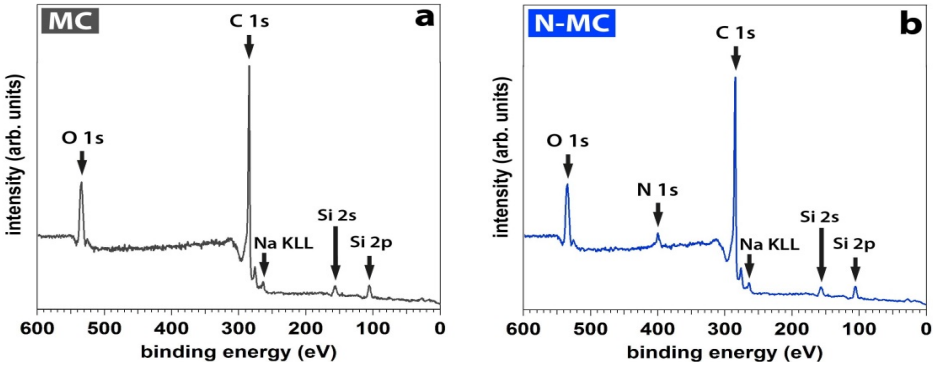

Fig. 6.10 - XPS spectra of MC (a) and N-MC (b) samples.

The results of elemental analysis of MC and N-MC, carried out by accurate XPS quantitative measurements, are reported in Table 6.2.

Table 6.2 - Elemental analysis derived from XPS measurements, for MC and N-MC.

	Si (%$_{at}$)	**Na (%$_{at}$)**	**C (%$_{at}$)**	**N (%$_{at}$)**	**O (%$_{at}$)**
MC	4.1	0.8	80.3	-	14.8
NMC	3.7	0.8	75.8	5.7	14.0

In order to get a more precise description of the chemical identity of the functional groups that are present on MC and on N-MC, the C 1s and N 1s energy regions have been acquired and the corresponding peaks have been fitted with Voigt functions, imposing a Full Width at Half Maximum (FWHM) in the range of 1.0–1.4 eV. Figure 6.11 reports the multi-peak analysis of the C 1s and N 1s signals for MC (a) and N-MC (b), both supported by modelling of the surface of the studied systems.

Concerning MC, we can distinguish five different components in the deconvolution of the C 1s photoemission spectrum: the main component (which constitutes 72% of the signal), centered at 284.5 eV, represents the sp^2-hybridized carbon (Csp^2) forming the graphitic lattice. The component centered at 285.5 eV is due to sp^3 hybridized carbon (Csp^3), which constitutes tetragonally coordinated carbon clusters and C-H bonds [34,35], while the third and fourth components at 286.4 eV and 288.0 eV, respectively, are related to the C-OH bonds and carbonyl (-C=O) groups. For a correct fitting procedure, it is also necessary to introduce a small component in the low-energy tail, which is related to C atoms around vacancy sites (BE = 283.7 eV) [43].

Interestingly, the C 1s spectrum of N-MC (Fig. 6.11b) shows an important increase of the Csp^3 component, which is interpretable with the formation of amorphous carbon. In fact, this side reaction is promoted by the low temperature treatment in ammonia (4 hours, 300 °C), performed on the MC precursor in order to obtain the nitrogen doping. Concerning the component centered at 286.4 eV, it is not possible to distinguish the contribution of the C-OH groups from that of the C-N bonds, which are known to give a characteristic signal centered at 286.6 eV [44]. Moreover, the carbonyl

component at 288.0 eV overlaps that of the -N-C-OH groups [45].

Table 6.3 - Results of the fitting procedure performed on the C 1s spectra related to MC (left) and N-MC (right). The percentages of each single component are normalized to the total integrated area of the C 1s spectrum. Δ is the FWHM of each component.

MC	A_i/A_{tot} (%)	N-MC	A_i/A_{tot} (%)
C vacancy **(BE = 283.7 eV - Δ =1.3 eV)**	6.6	C vacancy **(BE = 283.7 eV - Δ =1.3 eV)**	6.8
Csp^2 **(284.5 eV - Δ =1.3 eV)**	72.3	Csp^2 **(BE = 284.5 eV - Δ =1.3 eV)**	57.3
C-H (Csp^3) **(BE = 285.5 eV - Δ =1.1 eV)**	11.8	C-H (Csp^3) **(BE = 285.5 eV - Δ =1.2 eV)**	16.4
C-OH **(BE = 286.4 eV - Δ =1.3 eV)**	7.1	C-OH / C-N bonds **(BE = 286.5 eV - Δ =1.3 eV)**	14.7
C=O **(BE = 288.0 eV - Δ =1.2 eV)**	2.2	C=O / -N-C-OH **(BE = 288.0 eV - Δ =1.3 eV)**	2.7
		-N-C=O **(BE = 289.0 eV - Δ =1.2 eV)**	2.1

The new component at the high BE tail (BE = 289.0 eV) can be attributed to the presence of strong electron-withdrawing groups, such as formamide-like fragments (-N-C=O) [45]. Table 6.3 summarizes the results and makes a comparison between the fits of the different C 1s spectra.

Characterization of the nitrogen functional groups has been carried out by analysing the N 1s XPS signals, as reported in Fig. 6.11b. Seven different components have been identified [46], with the main peaks centered at 398.1 eV, 399.0 eV, 400.3 eV and 401.2 eV, which can be described as pyridinic groups [45,47] amine groups [43,45], pyrrolic groups [46] and graphitic N [46], respectively. According to the literature, in order to fit a curve consistently with the experimental data, we added three components centered at 402.5 eV, 403.7 eV and 404.8 eV, to the high-energy tail of the N 1s spectrum. These are attributable to quaternary nitrogen groups (402.5 eV), N-C-OH [48] and N-C=OH [48] groups (403.7 eV), and highly oxidized nitrogen groups [48] (404.8

eV), such as NO_x groups, even though in limited amount.

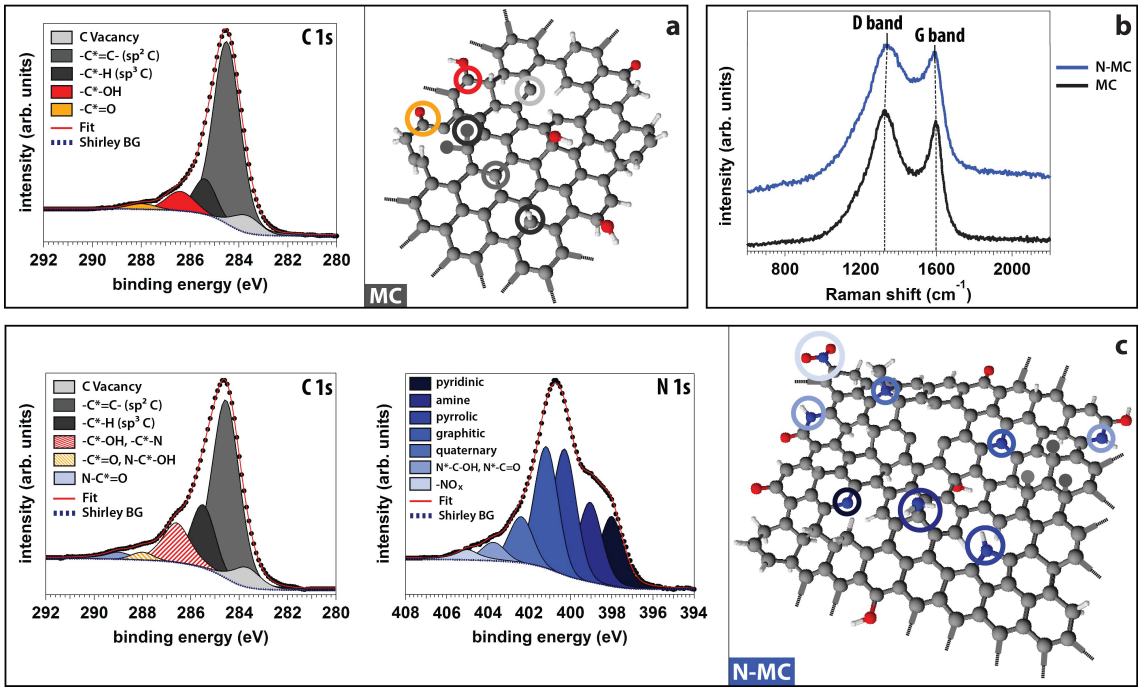

Fig. 6.11 – Detailed XPS spectra of MC (a) and N-MC (b), and Raman spectra of MC and N-MC (c).

Figure 6.11c compares Raman spectra of MC and N-MC. The two intense bands observed at 1600 cm^{-1} and at 1325 cm^{-1} are the G band [49] (tangential vibration mode, E_{2g} symmetry group) and the D band [49], also known as *disorder vibration mode* (belonging to the A_{1g} symmetry group), respectively. The latter is observable only in the presence of defects that lead to a local breakdown of the D_{6h} symmetry of the graphitic honeycomb lattice [49] (such as sp^3 carbon or dopant atoms). Compared to undoped MC, the N-MC sample shows a significant increase in structural disorder, as evidenced by the increase and the broadening of the D band. This is in agreement with the previous XPS observations; in fact, the evolution of the D band with the doping is due to both the increase of the sp^3 C and the doping of the carbon structure.

6.4 Deposition of metal NPs

Nanoparticles from different metal salts ($PdSO_4$, $PtCl_2$, $AuCl_3$) were loaded on undoped (Pd@MC, Pt@MC, Au@MC) and doped (Pd@N-MC, Pt@N-MC, Au@N-MC) MC by a simple chemical reduction method with sodium borohydride ($NaBH_4$) as the reducing agent. Initially, 5 mg of MC were dispersed in 2 mL of distilled water, and then the metal salt was added dropwise to the suspension under stirring. After 2 h at room temperature, 1 mL of $NaBH_4$ was added and the solution was kept under stirring for 12 h to complete the reaction. The mixture was filtered, washed and dried at 80 °C for 4 h. Metal NPs (Pd, Pt, Au) loaded on both MC and N-MC were homogeneously dispersed onto the external and internal surfaces. In figure 6.12, SEM images show metal nanoparticles with a size range below 10 nm.

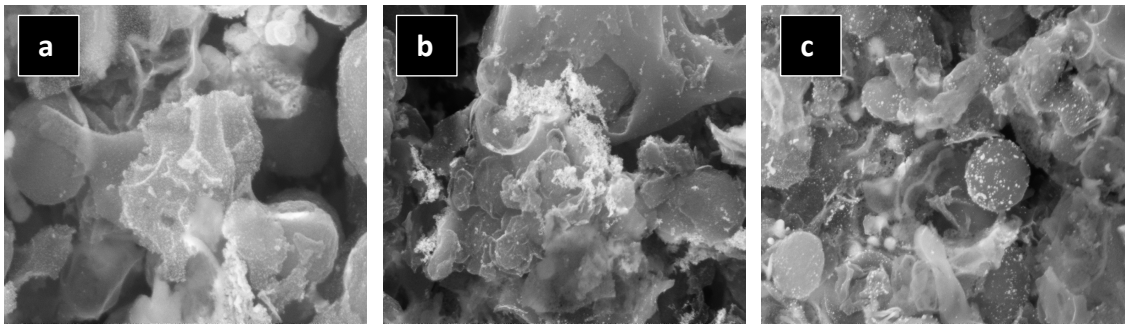

Fig. 6.12 - SEM images of 30% (a) Pd@MC, (b) Pt@MC and (c) Au@MC.

A large number of images with different magnifications, from 10× to 200,000×, were collected to analyse the particle size distribution. However, it was difficult to measure the diameter of each particle even from the images obtained at the highest magnification. Therefore, TEM analysis, which has a higher resolution than SEM, was used for this purpose.

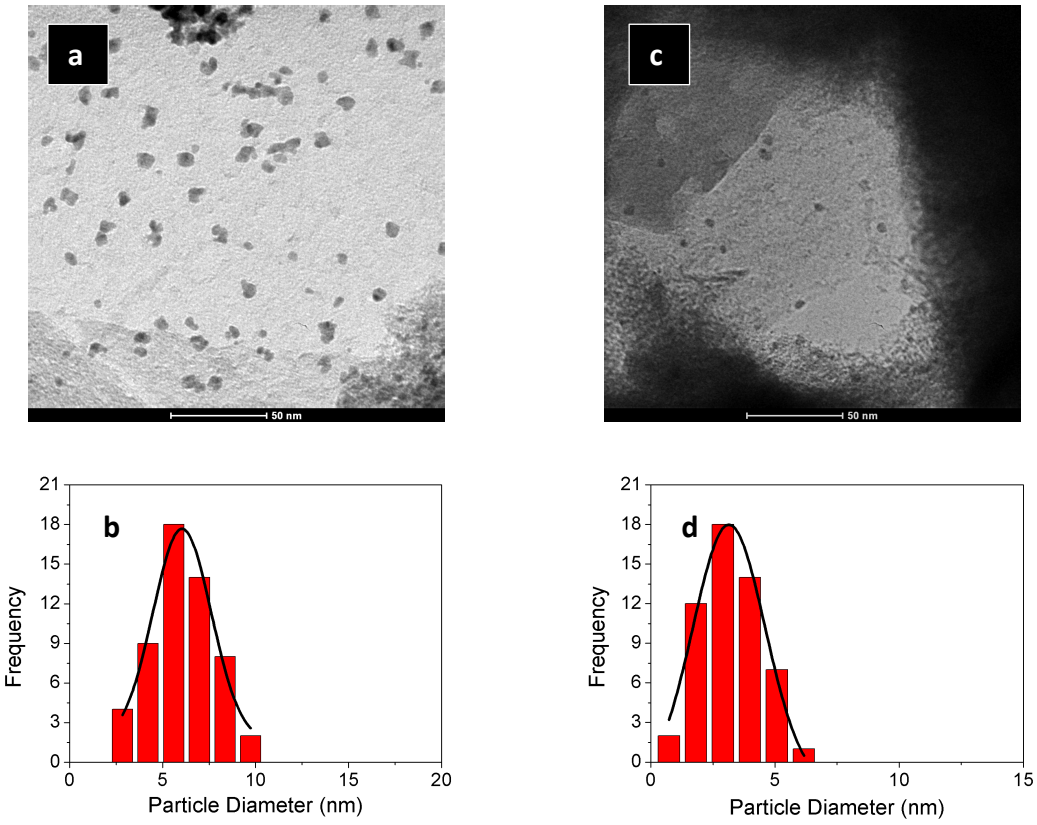

Fig. 6.13 - TEM image and size distribution of Pd@MC (a and b) and Pd@N-MC (c and d).

TEM images of Pd@MC (Fig. 6.13a) and Pd@N-MC (Fig. 6.13c) clearly show that Pd nanoparticles with high loading are uniformly dispersed throughout the samples. These results clearly indicate that the MC matrix is stable after the impregnation, drying, and reduction of the precursor. The size of the Pd nanoparticles was measured using a sample of approximately 100 nanoparticles in the TEM images, and from the size distribution histogram shown in Figure 6.13b, the average diameter of NPs in Pd@MC was calculated to be ca. 5-6 nm. Instead, in Pd@N-MC the presence of nitrogen causes a decrease of the particle size diameter to 2-3 nm. As we will see below, the metal catalyst dispersion is of great significance for the catalytic performance.

Similar results were obtained for Pt on MC and N-MC (Fig. 6.14 a and c), but in this case the particle size distribution is in practice the same for both the samples. (Fig. 6.14b and d).

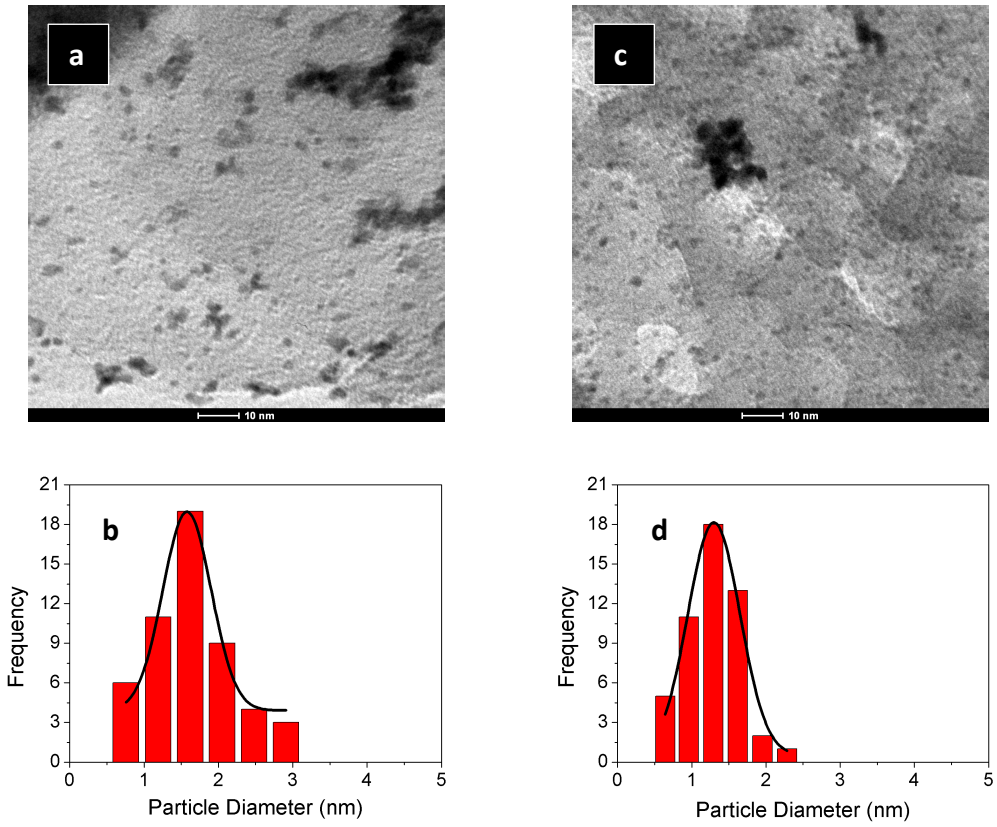

Fig. 6.14 - TEM image and size distribution of Pt@MC (a and b) and Pt@N-MC (c and d).

In order to evaluate the metal loading, Thermo Gravimetric Analysis (TGA) was carried out for each sample. The sample was exposed to air and its mass was recorded while the temperature was raised from r.t. to 1000 °C. After the complete oxidation of the carbon structure to gaseous products, metal and silica residues were left. The mass loading of the metal was close to the expected values of 30%, a result confirmed also by XPS analysis (Fig. 6.15).

To perform X-ray Photoemission Spectroscopy (XPS) measurements, 2.5 mg of the Me@MC or Me@N-MC (were Me = Pd, Pt or Au) powder were dispersed in 50 µL of toluene. After gently sonicating the suspensions for 5 minutes in order to efficiently disperse the powders, the solutions were drop-casted on electropolished polycrystalline copper or GC substrates (with a surface area of 1 cm^2). Thus, the samples were first dried overnight under nitrogen flux (250 sccm) to obtain homogeneous films; then finally, they were vacuum-dried for two hours at about 10^{-6} mbar.

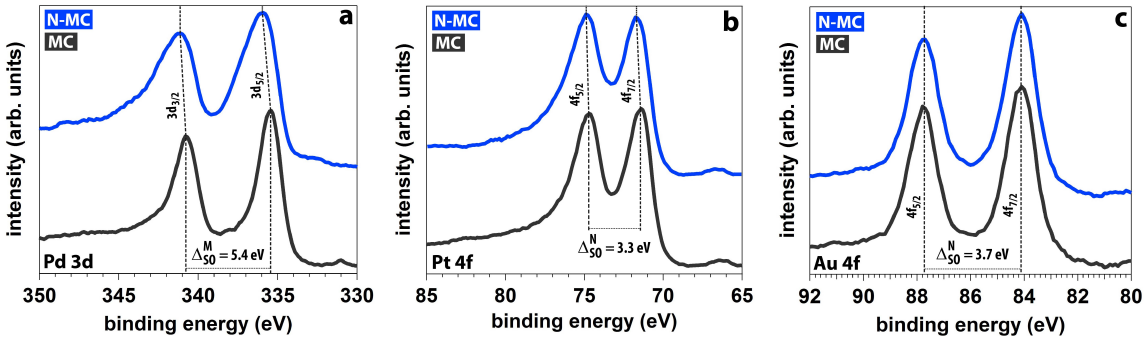

Fig. 6.15 - Spectral regions of the photoemission signals of the metals deposited on MC and N-MC (a) Pd, (b) Pt, and (c) Au.

Figure 6.15 reports the spectral regions of the photoemission signals of Pd, Pt and Au deposited on MC and N-MC. As can be observed, with the only exception of gold, the photoemission spectra of the metals show significant line broadening when they are deposited on N-MC; this can be explained with the formation of oxidized metal species over the nitrogen sites. Moreover, a shift of the signals takes place after the deposition on N-MC. However, the shift appears as a rigid spectral translation as can be observed from the values of the spin-orbit splitting (Δ_{SO}) reported in the Fig. 6.15. Table 6.4 reports the values of BEs and FWHM of the photoemission peaks recorded for Pd, Pt and Au deposited on both MC and N-MC.

Table 6.4 - BE and FWHM of XPS signals of Pd, Pt and Au deposited on MC and N-MC.

	MC		**N-MC**	
	BE (eV)	FWHM (eV)	BE (eV)	FWHM (eV)
Pd $3d_{5/2}$	335.4	1.7	336.0	2.9
Pt $4f_{7/2}$	71.3	1.4	71.6	1.7
Au $4f_{7/2}$	84.1	1.3	84.1	1.3

6.5 Activity toward Oxygen Reduction Reaction

A key element for the commercialization of devices using this reaction is the development of an efficient and cost effective catalyst capable of resolving the problem of the slow reaction rate at the electrode. For example, Pt-carbon materials are among the best catalysts in PEMFCs, but in the last years N-doped carbon materials have attracted a lot of interest as potential catalysts for ORR.

The electrochemical activity toward ORR of the various materials prepared during this work was evaluated by cyclic voltammetry and rotating disk electrode. The electrodes used for these measurements were prepared by drop-casting of catalyst inks on a clean surface (diameter = 3 mm) of glassy carbon.

The catalyst inks were prepared by adding 2.5 mg of Me@MC or Me@N-MC (Me = Pd, Pt, Au) in 2.5 mL Nafion (5%) solution, via ultrasonication for some minutes. Then 10 μL of suspension were carefully pipetted onto the GC. After that, it was dried in air at room temperature for at least 8 h. The LSV and RDE studies of oxygen reduction were recorded in 0.1 M H_2SO_4 and the solutions were purged with Ar before each measurement, whereas ORR measurements were carried out in an O_2 saturated solutions.

The polarization curves on MC and N-MC are depicted in Fig. 6.16a, whereby it is possible to see that the onset potential on N-MC is ca. 250 mV more positive than that on MC, and also the current normalized by the BET area is 1.5 times higher for N-MC than for MC. This improvement is ascribed to carbon atoms influenced by the neighbouring nitrogen dopants, which induces an *activation region* on the carbon surface. This kind of activated region can participate in the ORR reactions directly, or can anchor the metal nanoparticles used in the catalytic reaction, as we will see afterwards.

As shown in Fig. 16c, the onset potential of the ORR wave on the Pt@MC electrode is 0.484 V, which is identical to the onset potential at a commercial Pt@Vulcan XC-72 containing 30% of platinum; the two electrodes show also identical half-wave potentials for O_2 reduction. This shows that the Pt@MC catalyst obtained from our synthesis has the same catalytic activity as the commercial catalyst commonly used as a reference in the literature [50]. The current was normalized by the weight

content of the metal, which was achieved taking into account the concentration of the metal in 10 μL of ink necessary to prepare the catalyst electrode.

As was seen above for the N-MC, the presence of nitrogen defects on MC exalts the catalytic performance of Pt NPs toward ORR. In fact, the onset potential of Pt@N-MC was found to be 40 mV more positive than that of both Pt@MC and Pt@vulcan.

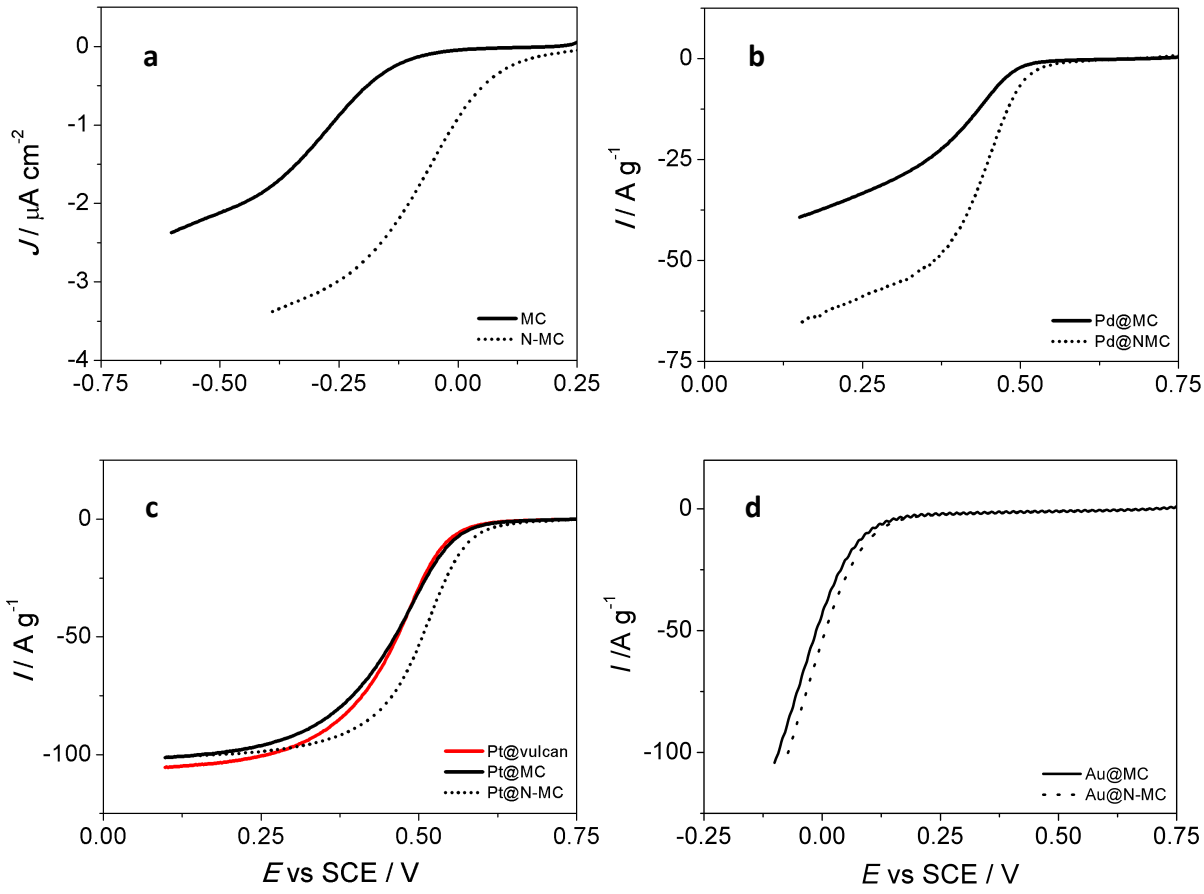

Fig. 6.16 – LSV curves recorded for ORR in 0.1 M H_2SO_4 on rotating disk electrodes at ω = 1600 rpm (scan rate 10 mV s^{-1}), using as electrode material: (a) MC and N-MC, (b) Pd@MC and Pd@N-MC, (c) Pt@MC, Pt@vulcan and Pt@N-MC, (d) Au@MC and Au@N-MC.

The same electrochemical behavior was found for Pd NPs on N-MC (Fig. 6.16b) in which acse, in addition to the gain of the peak potential (42 mV), a large increment of current was observed. The latter is related to the average diameter of the particles, which is about half that of Pd NPs in Pd@N-MC, as shown by TEM size distribution in Fig. 6.13b and d. Therefore, knowing from XPS and TGA analyses, that the undoped

and doped samples have the same content of metal loading, around 30%, we can deduce that the number of particles and consequently the active surface area in Pd@N-MC is higher than those in Pd@MC.

On the other hand, Au NPs on MC and N-MC did not show any reduction peak (Fig. 6.16d), due to the absence of any catalytic activity for the ORR [51].

Table 6.5 - ORR onset potentials in H_2SO_4 0.1 M

Electrode	$E_{1/2}$ **(V vs. SCE)**	***Metal loading (%)***
MC	-0.205	--
N-MC	0.038	--
Pd@MC	0.445	30
Pd@N-MC	0.487	30
Pt@MC	0.484	30
Pt@vulcan	0.482	30
Pt@N-MC	0.521	30

Thanks to the presence of N functional groups, the enhancement of activity obtained for Pt@- and Pd@N-MC is significant for new study and research in this field of electrochemical energy conversion.

Bibliography

[1] Kyotani, T.; Tsai, L.-F.; Tomita, A. *Chem. Mater.* **1996**, *8*, 2109.

[2] Dillon, A. C.; Jones, K. M.; Bekkedahl, T. A.; Kiang, C. H.; Bethune, D. S.; Heben, M.J. *Nature* **1997**, *386*, 377.

[3] Johnson, S. A.; Brigham, E. S.; Ollivier, P. J.; Mallouk, T. E. *Chem. Mater.* **1997**, *9*, 2448.

[4] Ryoo, R.; Joo, S. H.; Jun, S. *J. Phys. Chem. B* **1999**, *103*, 7743.

[5] Ryoo, R.; Joo, S. H.; Kruk, M.; Jaroniec, M. *Adv. Mater.* **2001**, *13*, 677.

[6] Wei, J.; Zhou, D.; Sun, Z.; Deng, Y.; Xia, Y.; Zhao, D. *Adv. Funct. Mater.* **2013**, *23*, 2322.

[7] Liu, C.W.; Wei, Y.C.; Wang, K.W. *J. Phys. Chem. C* **2011**, *115*, 8702.

[8] Favaro, M.; Perini, L.; Agnoli, S.; Durante, C.; Gennaro, A.; Granozzi, G. *Phys. Chem. Chem. Phys.* **2013**, *15*, 2923.

[9] Perini, L.; Durante, C.; Favaro, M.; Agnoli, S.; Granozzi, G.; Gennaro A. *Appl. Catal. B: Environ.* **2014,** *144*, 300.

[10] Leiva, E.; Iwasita, T.; Herrero, E.; Feliu, J.M. *Langmuir* **1997**, *13*, 6287.

[11] Smith, S.P.E.; Abrunã, H.D. *J. Electroanal. Chem.* **1999**, *467*, 43.

[12] Davis, M.E. *Nature* **2002**, *417*, 813.

[13] Attard, G.S.; Bartlett, P.N.; Coleman, N.R.B.; Elliott, J.M.; Owen, J.R.; Wang, J.H. *Science* **1997**, *278*, 838.

[14] Attard, G.S.; Goltner, C.G.; Corker, J.M.; Henke, S.; Templer, R.H. *Angew. Chem. Int. Ed.* **1997**, *36*, 1315.

[15] Lee, J.; Yoon, S.; Hyeon, T.; Oh, S.M.; Kim, K.B. *Chem. Commun.* **1999**, 2177.

[16] Jun, S.; Joo, S.H.; Ryoo, R.; Kruk, M.; Jaroniec, M.; Liu, Z.; Ohsuna, T.; Terasaki, O. *J. Am. Chem. Soc* **2000**, *122*, 10712.

[17] Ma, Z.X.; Kyotani, T.; Tomita, A. *Chem. Commun.* **2000**, 2365.

[18] Shin, H.J.; Ko, C.H.; Ryoo, R. *J. Mater. Chem.* **2001**, *11*, 260.

[19] Liang, C.D.; Hong, K.L.; Guiochon, G.A.; Mays, J.W.; Dai, S. *Angew. Chem. Int. Ed.* **2004**, *43*, 5785.

[20] Tanaka, S.; Nishiyama, N.: Egashira, Y.; Ueyama, K. *Chem. Commun.* **2005**, 2125.

[21] Meng, Y.; Gu, D.; Zhang, F.Q.; Shi, Y.F.; Cheng, L.; Feng, D.; Wu, Z.X.; Chen, Z.X.; Z.X. Wan, Z.X.; Stein, A.; Zhao, D.Y. *Chem. Mater.* **2006**, *18*, 4447.

[22] Zhong, M.; Natesakhawat, S.; Baltrus, J.P.; Luebke, D.; Nulwala, H.; Matyjaszewski, K.;

Kowalewski, T. *Chem. Commun.* **2012**, *48*, 11516.

[23] Joo, S.H.; Jun, S.; Ryoo, R. *Micropor. Mesopor. Mat.* **2001**, *44-45*, 153.

[24] Joo, S.H.; Choi, S. J.; Oh, I.; Kwak, J.; Liu, Z.; Terasaki, O.; Ryoo, R. *Nature* **2001**, *412*, 169.

[25] Meng, Y.; Gu, D.; Zhang, F.; Shi, Y.; Yang, H.; Li, Z.; Yu, C.; Tu, B.; Zhao, D. *Angew. Chem. Int. Ed.* **2005**, *117*, 7215.

[26] Li, L.; Zhu, Z.H.; Lu, G.Q.; Yan, Z.F.; De Marco, R. *Appl. Catal. A: Gen.* **2006**, *309*, 201.

[27] Xia, Y.; Mokaya, R. *Chem. Mater.* **2005**, *17*, 1553.

[28] Fuertes, A.B.; Nevskaia, D. M. *J. Mater. Chem.* **2003**, *13*, 1843.

[29] Wang, X.; Lee, J.S.; Zhu, Q.; Liu, J.; Wang, Y.; Dai, S. *Chem. Mater.* **2010**, *22*, 2178.

[30] Darmstadta, H.; Roya, C.; Kaliaguinea, S.; Choib, S.J.; Ryoo R. *Carbon* **2002**, *40*, 2673.

[31] Borup, R.; Meyers, J.; Pivovar, B.; Kim, Y. S.; Mukundan, R.; Garland, N.; Myers, D.; Wilson, M.; Garzon, F.; Wood, D.; Zelenay, P.; More, K.; Stroh, K.; Zawodzinski, T.; Boncella, J.; McGrath, J.E.; Inaba, M.; Miyatake, K.; Hori, M.; Ota, K.; Ogumi, Z.; Miyata, S.; Nishikata, A.; Siroma, Z.; Uchimoto, Y.; Yasuda, K.; Kimijima, K.I.; Iwashita, N. *Chem. Rev.* **2007**, *107*, 3904.

[32] Wang, J.X.; Inada, H.; Wu, L.; Zhu, Y.; Choi, Y.M.; Liu, P.; Zhouand, W.P.; Adzic, R.R. *J. Am. Chem. Soc.* **2009**, *131*, 17298.

[33] Wang, W.M.; Huang, Q.H.; Liu, J.Y.; Zou, Z.Q.; Li, Z.L.; Yang, H. *Electrochem. Commun.* **2008**, *10*, 1396.

[34] Wei, D.; Liu, Y.; Wang, Y.; Zhang, H.; Huang, L.; Yu, G. *Nano Lett.* **2009**, 9, 1752.

[35] Wang, T.S.; Ding, J.J.; Cheng, R.; Peng, H.B.; Lu, X.; Zhao, Y.T. *Nucl Instrum Meth B* **2012**, *272*, 15.

[36] Ania, C.O.; Khomenko, V.; Raymundo-Piñero, E.; Parra, J.B.; Béguin, F. *Adv. Funct. Mater.* **2007**, *17*, 1828.

[37] Lota, G.; Lota, K.; Frackowiak, E. *Electrochem. Commun.* **2007**, *9*, 1828.

[38] Maldonado, S.; Stevenson, K.J. *J. Phys. Chem. B* **2005**, *109*, 4707.

[39] Lei, Z.B.; Zhao, V.; Dang, L.; An, L.; Lu, M.; Lo, A.Y.; Yu N.Y.; Liu, S.B. *J. Mater. Chem.* **2009**, *19*, 5985.

[40] Oh, J.G.; Lee, C.H.; Kim, H. *Electrochem. Commun.* **2007**, *9*, 2629.

[41] Liu, R.; Wu, D.; Feng, X.; Müllen, K. *Angew. Chem. Int. Ed.* **2010**, *49*, 2565.

[42] Shin, Y.; Fryxell, G.E.; Engelhard, M.H.; Exarhos, G.J. *Inorg. Chem. Commun.* **2007**, *10*, 1541.

[43] Barinov, A.; Malcioglu, O.B.; Fabris, S.; Sun, T.; Gregoratti, L.; Dalmiglio, M.; Kiskinova, M.J. *Phys. Chem. C* **2009**, *113*, 9009.

[44] Zhang C, Fu L, Liu N, Liu M, Wang Y, Liu Z, *Adv. Mater.* **2011**, *23*, 1020.

[45] Usachov, D.; Vilkov, O.; Grüneis, A.; Haberer, D.; Fedorov, A.; Adamchuk, V.K.; Preobrajenski, A.B.; Dudin, P.; Barinov, A.; Oehzelt, M.; Laubschat, C.; Vyalikh, D.V. *Nano Lett.* **2011**, *11*, 5401.

[46] Favaro, M.; Perini, L.; Agnoli, S.; Durante, C.; Granozzi, G.; Gennaro, A. *Electrochim. Acta* **2013**, *88*, 477.

[47] Hellgren, N.; Guo, J.; Luo, Y.; Såthe, C.; Agui, A.; Kashtanov, S.; Nordgren, J.; Ågren, H.; Sundgren, J.E. *Thin Solid Films* **2005**, *471*, 19.

[48] Pylypenko, S.; Queen, A.; Olson, T.S.; Dameron, A.; O-Neill, K.; Neyerlin, K.C.; Pivovar, B.; Dinh, H.N.; Ginley, D.S.; Gennet, T.; O-Hayre, R. *J. Phys. Chem. C* **2011**, *115*, 13667.

[49] Dresselhaus, M.S.; Jorio, A.; Saito, R. *Annu. Rev. Condens. Matter Phys.* **2010**, *1*, 89.

[50] Liu, S.H.; Wu, M.T.; Lai, Y.H.; Chiang, C.C.; Yu, N.; Liu, S.B. *J. Mater. Chem* **2011**, *21*, 12489.

[51] M. Shao, Electrocatalyst in Fuel Cells, Lecture Notes in Energy 9, Springer **2013**.

CONCLUSIONS

In the present thesis, a structural study of the morphological and chemical modifications induced on N-HOPG, N-GC and N-MC samples by different doping-ways have been discussed. In particular, the attention was focused on the electrochemical characterization of Oxygen Reduction Reaction (ORR) and the reductive cleavage of Carbon-Halogen bond. The most relevant results obtained for each electrode material will be briefly described in the following paragraphs.

- Highly Oriented Pyrolytic Graphite

The strong amorphization, induced by ion-implantation on both Ar-HOPG and N-HOPG surfaces, has resulted to be the most critical factor determining the electrochemical properties of these materials, as demonstrated by the faster kinetics of ET determined for the probes $Ru(NH_3)_6^{3+}$ and $[Fe(CN)_6]^{4-}$. Interestingly, the N-implantation is accompanied not only by morphological changes but also by chemical defects that have been identified quite precisely by XPS. It was also shown that it is possible to maximize the concentration of a selected type of defects, for example passing from a surface exposing mostly C-N terminal groups to a surface where the predominant defects are of pyridinic and pyrrolic type, simply by annealing the HOPG sample at a proper temperature. This ability to control the surface functionality of one of the archetypal carbon supports, i.e. graphite, and to study in great detail its atomic structure and electrochemical activity, represents an important methodological achievement. It was verified that the introduction of nitrogen functional groups enhances the catalytic activity of HOPG toward ORR and that the reduction process follows a four-electron pathway leading directly to H_2O without side reactions to H_2O_2. The results obtained at the N-HOPG electrode represent a benchmark for explaining the similar reactivities found for N-doped graphene and electrodes made from carbon nanotubes. We have shown that nitrogen groups on N-HOPG induce the presence of an

excess negative surface charge, which may exert a beneficial influence on the electrodeposition of metal particles on the N-HOPG surface.

In this sense, using a rigorous surface science approach, we have checked the role played by N defects on the nucleation and stabilisation of Palladium NPs. Our data suggest that the N implantation process carried out at few hundreds of eV generates N-defects that are not suitable to chemically interact with the catalyst NPs because they are mostly localised under the exposed surface.

In contrast, when considering the NP size and their stability toward heating, large differences are observed when comparing Pd/HOPG and Pd/N-HOPG samples. We have observed a drastic reduction in the size distribution when Pd deposition is performed on N-HOPG. Furthermore, we have demonstrated that the thermal stability of Pd NPs can increase simply by introducing chemical and morphological defects in the carbon support. Concerning the electrochemical activity versus ORR, it has been shown that the catalytic activity depends more on the Pd loading than on the type of the support since slight differences between Pd/N-HOPG and Pd/HOPG have been observed.

- Glassy Carbon

Morphologically and chemically stable Pd NPs deposited on N-GC, doped by ion implantation or by electrochemical methods, are spherical in shape and uniformly distributed with average size of 20 and 12.5 nm over the N-GC surface. The presence of nitrogen functional groups introduced into the GC support seems to influence the nucleation and growth kinetics during Pd NPs deposition, which results in smaller catalyst particle sizes and higher particle dispersion. The most striking result is that the presence of nitrogen functionalities promotes the catalytic performance of Pd NPs toward activation of the C-Cl bond, so extensively that Pd@N-GC is more active not only than Pd NPs loaded on undoped GC, but even than bulk Pd in both cases.

- Mesoporous Carbon

A simple but elegant way to synthesize MC and N-MC was developed and the products were carefully characterized, both before and after metal NPs (Pd, Pt, Au) deposition, by means of physical and electrochemical methods. BET data revealed that changing the heating rate of synthesis causes a great loss of the surface area (up to 20 %). The synthetic conditions were therefore optimized and the best conditions that generate the sample with the highest surface area were chosen to prepare N-MC. On the doped support, metal nanoparticles were deposited by a chemical reduction method with a metal loading of 30 %. In particular, Pd NPs on N-MC are smaller in size and higher in dispersion if compared with those obtained on MC.

While Au NPs showed no electrochemical activity for ORR, both Pd@N-MC and Pt@N-MC demonstrated beneficial effects due to the introduction of the nitrogen functional groups. Moreover, Pd@N-MC showed not only a beneficial effect in terms of the onset potential of ORR but also in terms of current density due to the smaller size of the NPs and a corresponding greater surface area.

PUBLICATIONS

- **Perini, L.**; Durante, C.; Favaro, M.; Agnoli, S.; Granozzi, G.; Gennaro, A. Electrocatalysis at palladium nanoparticles: Effect of the support nitrogen doping on the catalytic activation of carbon-halogen bond. *Applied Catalysis B: Environmental*, **2014**, *144*, 300–307.

- Favaro, M.; **Perini, L.**; Agnoli, S.; Durante, C.; Granozzi, G.; Gennaro, A. Electrochemical behaviour of N and Ar implanted highly oriented pyrolytic graphite substrates and activity toward oxygen reduction reaction. *Electrochimica Acta*, **2013**, *88*, 477–487.

- Favaro, M.; Agnoli, S.; **Perini, L.**; Durante, C.; Gennaro, A.; Granozzi, G. Palladium nanoparticles supported on nitrogen-doped HOPG: a surface science and electrochemical study. *Physical Chemistry Chemical Physics*, **2013**, *15*, 2923–31.

CONFERENCES

*GEI 2013 Giornate dell'Elettrochimica Italiana, 22-27 September **2013**, Pavia, Italy.*

- Oral presentation: **Perini, L.**; Durante, C.; Leonardi, S.; Schneider, O.; Kunze, J.; Favaro, M.; Granozzi, G.; Gennaro, A. *Platinum And Palladium Nanoparticle Catalysts Supported On Activated Mesoporous Carbon For The Oxygen Reduction Reaction.*
- Oral presentation: Durante, C.; Perazzolo, V.; **Perini, L.**; Gennaro A. *Carbon-Halogen Bond Activation at Nanostructured Copper and Palladium Electrodes.*
- Poster: Durante, C.; **Perini, L.**; Favaro, M.; Agnoli, S.; Granozzi, G.; Gennaro, A; *Electrocatalysis at Palladium Nanoparticles: Effect of the Nitrogen Doped Glassy Carbon on the Catalytic Activation of Carbon-Halogen Bond.*

*64th Annual Meeting of the International Society of Electrochemistry ISE, 8-13 September **2013**, Santiago de Queretaro, Mexico.*

- Oral presentation: **Perini, L.**; Durante, C.; Leonardi, S.; Schneider, O.; Kunze, J.; Favaro, M.; Granozzi, G.; Gennaro, A. *Synthesis of Nitrogen Doped Mesoporous Carbon Supported Catalyst with Metal Nanoparticles for the Oxygen Reduction Reaction.*
- Oral presentation: **Perini, L.**; Durante, C.; Favaro, M.; Agnoli, S.; Granozzi, G.; Gennaro, A. *Electrocatalysis at Pd Nanoparticles: Effect of the Support Nitrogen Doping on the Catalytic Activation of Carbon-Halogen Bond.*

*GEI 2012 Giornate dell'Elettrochimica Italiana, 17-22 June **2012**, Santa Marina Salina, Messina, Italy.*

- Poster: **Perini, L.**; Durante, C.; Favaro, M.; Agnoli, S.; Granozzi, G.; Gennaro, A. Palladium Nanoparticles on N-doped HOPG for Oxygen Reduction Reaction.

*XXIV National Meeting Italian Chemistry Society, 11-16 September **2011**, Lecce, Italy.*

- Oral presentation: **Perini, L.**; Durante, C.; Pilot, R.; Giallongo, G.; Granozzi, G.; Bozio, R.; Gennaro, A.; Electrodeposition of metal nanoparticles on commercially available Digital Versatile Disk (DVD) for sensing and catalysis.